UNIVERSITÄT BONN
Physikalisches Institut

X-ray absorption spectroscopy investigation of structurally modified lithium niobate crystals

von
Tonya Vitova

The type and concentration of impurity centers in different valence states are crucial for tuning the photorefractive properties of doped Lithium Niobate (LN) crystals. X-ray Absorption Spectroscopy (XAS) is an appropriate tool for studying the local structure of impurity centers. XAS combined with absorption in UV/VIS/IR and High Resolution X-ray Emission Spectroscopy (HRXES) provide information about the valence state of the dopant ions in as-grown, reduced or oxidized doped LN crystals. Cu (Cu^{1+} and Cu^{2+}) and Fe (Fe^{2+} and Fe^{3+}) atoms are found in two different valence states, whereas there are indications for a third Mn valency, in addition to Mn^{2+} and Mn^{3+} in manganese-doped LN crystals. One of the charge compensation mechanisms during reduction of copper-doped LN crystals is outgassing of oxygen atoms. Cu ions in the reduced crystals have at least two different site symmetries: twofold (Cu^{1+}) and sixfold (Cu^{2+}) coordinated by O atoms. Fe and Mn atoms are coordinated by six O atoms. Cu and Fe ions are found to occupy only Li sites, whereas Mn ions are also incorporated into Li and Nb sites. The refractive index change in LN crystals irradiated with $^3He^{2+}$ ions is caused by structurally disordered centers, where Nb atoms are displaced from normal crystallographic sites and Li or/and O vacancies are present.

Post address:
Nussallee 12
53115 Bonn
Germany

BONN-IR-2008-03
Bonn University
February 2008
ISSN-0172-8741

UNIVERSITÄT BONN
Physikalisches Institut

X-ray absorption spectroscopy investigation of structurally modified lithium niobate crystals

von
Tonya Vitova

Dieser Forschungsbericht wurde als Dissertation von der Mathematisch - Naturwissenschaftlichen Fakultät der Universität Bonn angenommen.

Tag der Promotion:	8.02.2008
Referent:	Prof. Dr. J. Hormes
Korreferent:	Prof. Dr. K. Maier

Diese Dissertation ist auf dem Hochschulschriftenserver der ULB Bonn unter http://hss.ulb.uni-bonn.de/diss_online elektronisch publiziert.

Erscheinungsjahr: 2009

To my parents and my Vlady

Contents

Chapter 1

Motivation

The increased requirements for larger memory capacities have boosted the development of new data storage technologies. However, even nowadays, most data storage is based on surface recording technologies, e.g., compact discs, which restricts the usable memory of a storage with a fixed size. For example, the capacity of a compact disc is about 1 gigabyte, while a disc produced by InPhase, a holographic technology company, can store up to 200 gigabytes [73]. Another drawback is the recording speed, which is determined by the bit by bit saving of information. The idea for implementing the wide use of holografic data storage originates from 1963, when Pieter van Heerden, who was working on holographic technologies at Polaroid's labs in Cambridge Massachusetts, proposed a storage method based on a light-induced refractive index pattern [186]. The information is stored in the volume of a storage material allowing terabytes memory capacity on half the size of a floppy disc. The recording speed is increased by orders of magnitude since the bits are replaced by pages. For data recording a wave called data (data wave), obtained by illuminating from behind a data page, and a reference wave interfere. When this interfering pattern illuminates a light sensitive material, organic or inorganic [122], its microstructure changes in the light regions. The data wave is reconstructed by illuminating the storage with the reference wave. Volume recording of pages with information is achieved by slight changes of the incident angle of the reference wave. This method permits to search for an exact data page by comparing the intensity of the reference waves after illumination with a data wave. Because of the different incident angles, the true reference wave will have the highest intensity [73].

Lithium Niobate (LN), on which this thesis concentrates, is one of the most promising photorefractive crystals for holografic data storages [12, 37]. Its performance depends strongly on the type and concentration of extrinsic impurity centers. The best results are achieved by doping LN crystals with 3d transition metals Cu, Mn or Fe [31, 32, 139–141, 169, 170, 208]. These impurity centers are usually found in two oxidation states, e.g., Fe^{2+} and Fe^{3+}. Upon illumination with an interference pattern, the electrons from the Fe^{2+} centers in the light regions are excited and after reaching the conduction band, they move towards the dark regions by drift, diffusion and bulk photovoltaic effect [63] until they are finally trapped by the Fe^{3+} impurity centers [see Fig. 6.1 a)]. The redistributed charge builds up space-charge fields, which modulate the refractive index via the electro-optic effect and thus forms a diffraction grating. Illumination with non-interfering light leads to diffraction, which reconstructs the saved pattern.

Tremendous work has been done in improving the quality of potential holograhic storage materials, by increasing the stability, power and wide availability of the needed laser devices and by under-

standing of the involved physical processes. Despite of all these efforts, today, about 50 years later, this great idea for data storage is still not widely used. One of the problems is the long-term storage of the recorded holograms. A recorded hologram, e.g., in a LN crystal, decays about ten minutes after illumination with a reading beam. Without illumination at room temperature the lifetime of a hologram is a few hours [31]. Obviously, this is a real problem for long-term storage, which has been overcome by several ingenious ideas [8, 100, 125, 192]. One of these ideas is to heat up the crystal before or during recording, which makes the intrinsic impurity protons H^+ mobile [32]. They diffuse in the crystal and compensate the redistributed charge. Such a thermally fixed hologram can be saved for thousands of years. Another fixing method is recording with high-intensity ultra violet light and reading with low intensity light (manganese-doped LN crystals) [192]. It is also possible to realize non-volatile storage by doping LN crystals with Mn and Fe, whose energy levels differ in the conduction band, i.e., the Mn center is deeper [31].

Iron doped LN crystals are the best-studied, but Cu and Mn doped LN crystals tend to have some advantages. For example, because of the huge diffusion constant of Cu (exceeding 500 times the one of Fe [86, 98]), it is possible to indiffuse copper into a LN crystal under laboratory conditions [86, 140]. This allows a better control of the doping level and reduces production costs. The conventional doping consists of adding metal oxides in a congruent melt and pulling the crystal by the Czochralski method. By increasing the doping level of the impurity centers, an increased refractive index change, which means increased storage capacity, is achieved. However, this is valid only until a certain concentration is reached. Other important parameters of holographic storage are sensitivity, dynamic range and dark decay times, which determine the speed, signal-to-noise-ratio and volatility of a hologram, respectively. The highest particle doping level in manganese-doped LN crystals is 0.5 wt% [208]; it is ~ 0.1 wt% for iron [139].

The quality performance of holographic data storage, i.e., its characteristics as a storage capacity, sensitivity, dynamic range and dark decay time, exclusively depend on the microscopic structural properties of the impurity centers and their concentration. In order to tune the ratio of the different valencies of the doped atoms, reduction or oxidation treatments are performed. This ratio has direct influence on the refractive index change and the dark decay time of a doped LN crystal [139–141, 208]. A great amount of research has been carried on in order to determine the formal oxidation state of the doped atoms and their site of occupation. Another research aim has been to understand the reduction and oxidation mechanisms leading to lower and higher oxidation states of the doped metal atoms and the favorable charge compensation mechanisms. Spectroscopic methods such as absorption spectroscopy in UV/VIS/IR [106], Electron Paramagnetic Resonance (EPR) [119], Electron Nuclear Double Resonance (ENDOR) [39], Optically Detected Magnetic Resonance (ODMR) [137] and Mösbauer spectroscopy [106] are usually sensitive to only one of the formal oxidation states of the impurity centers or to only one element. For example, Mösbauer spectroscopy detects Fe^{2+} and Fe^{3+} but none of the other transition metals. Wöhlecke et al. give an overview of the advantages and limitations of optical methods used to characterize the composition and homogeneity of LN crystals [198]. Despite all published structural studies many questions remain unanswered.

One of the strengths of the X-ray Absorption Spectroscopy (XAS) is its ability, in most cases, to detect the average formal oxidation state of an element by comparing the energy position of the absorption edge with these of reference compounds. By combining XAS with absorption spectroscopy in UV/VIS/IR, a reliable picture of the average formal oxidation state and the contributing valencies of the probed element is obtained. The X-Ray Absorption Near Edge Structure (XANES) regime of a XAS spectrum is also a direct measure of the local symmetry of the probed element.

The site of occupation of the doped atoms can be characterized by EPR only in some cases. XAS probes the local structure around the absorbing atoms up to distances of about 6 Å, which is sufficient to identify the incorporation site of the impurity center. Moreover, deviations from the exact Li or Nb sites in the lattice are easily detected by Extended X-ray Absorption Fine Structure (EXAFS) analysis, which has precision in distance determinations to ± 0.02 Å. Classical structure determination methods such as X-Ray Diffraction (XRD) are not sensitive to low doping levels (0.3-4 wt%) of metal atoms.

If the light-induced refractive index changes are favorable for some applications, they are undesirable for others and in these cases are called "optical damage". Some ppm of iron always exist in the grown LN crystals. Upon illumination, a refractive pattern develops, which disturbs the phase matching conditions and the beam profile in nonlinear-optical applications. This problem can be solved by strong oxidation of the LN crystal with thermo-electric oxidization method [52] [see Fig. 6.1 b)].

LN crystals are also successfully employed for the development of a novel type of waveguide [143]. This waveguide is based on differences in the refractive index between the guiding channel formed from non-irradiated LN crystal and the medium around the channel of LN crystal irradiated with $^3He^{2+}$. It is assumed that structural damage caused by the high energy $^3He^{2+}$ ions is the reason for the reduced refractive index of the irradiated material. It is a challenging task for the XAS technique to elucidate these structural changes, because it is only possible to probe the electronic and local geometric structure of the heaviest atom in the compound, i.e., Nb.

The aim of this thesis is to study the electronic and geometric structure of the Cu, Mn and Fe impurity centers in the doped LN crystals and the structural damage of the irradiated LN crystals using XAS, High Resolution X-ray Emission Spectroscopy (HRXES) and absorption spectroscopy in UV/VIS/IR. Only few XAS studies has been performed on copper, iron and manganese doped LN crystals. These studies are incomplete and do not fully employ the structural characterization resources of the technique [34, 120, 134, 212]. In this work the average formal oxidation states of Cu, Mn and Fe in doped as well as treated (reduced or oxidized) crystals are determined and the contributing formal oxidation states of the elements are identified. The mechanisms involved in the reduction treatment of copper-doped LN crystals leading to lower formal oxidation state of the doped Cu atoms and the possible charge compensation mechanisms are elucidated for the first time. The site of incorporation of the Cu, Fe and Mn atoms are determined through EXAFS analyses and simulation and calculation of XANES spectra with the FEFF8.2 code [10]. The goal goes beyond an average determination of the geometrical structure of the impurity centers. In Chapter 6.3, an in situ XAS study and HRXES study on iron doped LN crystals is presented, which yields valence selective geometric structural information. In Chapter 7, the possible structural defects in $^3He^{2+}$ irradiated LN crystals are explored by both simulation and theoretical calculations of Nb K-edge XANES spectra with the FEFF8.2 code and EXAFS analysis.

In the framework of this thesis HRXE studies have been performed for the first time in the Synchrotron Radiation Group in PI-Bonn. An overview of this new technique, its advantages and a comparison to conventionally measured XANES spectra of iron and manganese oxides is given in Chapter 3.

Chapter 2

Fundamentals of XAS

The discovery of X-rays by Röntgen in 1895, followed by the first observation of an absorption edge by de Broil in 1913 provided the basis for the development of the X-ray Absorption Spectroscopy (XAS) technique [later called also X-ray Absorption Fine Structure (XAFS) spectroscopy]. In the last 30 years the appearance of second and third generation synchrotron radiation facilities, providing X-rays with orders of magnitude higher brilliance than a X-ray tube, and the improved theoretical understanding of the experimental spectra, led to numerous applications of the XAS technique.

Why is XAS powerful as a structural characterization tool? Its advantages include the fact that it can be applied not only to solid samples but with the same success to liquid and gas samples (see, e.g., [214]) as a non-destructive technique and can be a bulk or a surface sensitive technique. It is perfectly applicable not only to crystalline, as for example X-Ray Diffraction (XRD), but also to amorphous materials. At the same time, it can probe the structure of biological, archaeological and even highly radioactive materials [44]. The XAS technique is element specific, i.e., a XAFS spectrum reflects the local electronic and geometric environment of a chosen element in a complex system: therefore, it is suitable for studying dopant atoms at concentrations down to a few ppm of the element in question.

What can be learned from a XAFS spectrum?: 1) the formal oxidation state of the probed element; 2) its local symmetry; 3) a short range geometrical structure until ~6 Å , i.e., number of near neighboring atoms and their distance from the absorber; 4) by applying fingerprint analysis, it is possible to confirm or reject a crystallographic phase of question; 5) fast/slow changes in structure can be recorded in-situ; 6) often structural disorder can be tracked.

The advantages of the XAS technique make it a favorable tool for solving many structural problems. In this thesis XAS will be applied for answering a series of questions concerning the electronic and geometric structure of the doped transition metal atoms in LN crystals.

2.1 The X-ray absorption process

The attenuation of the intensity of X-rays interacting with matter is due to scattering and absorption processes. Relevant for XAS is the photo-electric effect. When the energy of a photon ($E = h\nu$) is transferred to a bound core electron in an atom, the electron is excited to an unoccupied state (see Fig. 2.1 left). The process can take place only if the photon possesses energy higher than the

energy of the bound atomic state of interest. The excited atom relaxes by filling the created core hole with an electron from an upper shell followed by emission of a photon (see Fig. 2.1 middle) or an Auger electron (see Fig. 2.1 right). The intensity of the X-ray beam transmitted through a material is given by the Beer's law

$$I(E) = I_0 e^{-\mu(E)t}, \tag{2.1}$$

where I_0 is the intensity of the primary beam, I is the intensity of the transmitted beam, t is the thickness of the sample and μ is the absorption coefficient (see, e.g., [6] and [183]).

The absorption coefficient μ depends on the density of the sample ρ, the atomic number Z and atomic mass A of the probed atom and the X-ray energy E as

$$\mu \approx \frac{\rho Z^4}{AE^3}. \tag{2.2}$$

μ measures the probability for a transition of an electron from an initial state $\langle i|$ (i = initial) of an absorbing atom to an unoccupied state $\langle f|$ (f = final). A quantum-mechanical description of the absorption process is provided by the Fermi's Golden rule, which for a single electron and dipole approximations is (see, e.g, [10] and [150])

$$\mu(E) \propto \sum_{f}^{E_f - E_F} |\langle f|\hat{\epsilon} \cdot \mathbf{r}|i\rangle|^2 \delta(E - E_f), \tag{2.3}$$

where i and f are the wavefunctions for the initial and final eigenstates of the effective one-electron Hamiltonian H for the initial state and H′ for the final state, with energies E and E_f respectively. $\hat{\epsilon} \cdot \mathbf{r}$ is the dipole operator for the incident electromagnetic wave interacting with the material.The sum is over all energies above the Fermi level (E_F).

The $\mu(E)$ rises abruptly, when the energy of the incident X-rays equals the binding energy of a core electron. This absorption "jump" is called an absorption edge [6]. As there are significant differences in core electron binding energies for different elements (cf Moseley's law), the measured absorption edge is element specific. A XAFS spectrum of LN measured at the K absorption edge of Nb (18.986 keV) is displayed in Figure 2.2. The XAFS spectrum is traditionally divided into the X-ray Absorption Near Edge Structure (XANES) and Extended X-ray Absorption Fine Structure (EXAFS) parts, where the separation between the two regions may vary and usually overlap (see Fig. 2.2).

2.2 The XANES spectrum

The absorption spectrum of a free atom resembles a decaying step function (weak oscillations are possible, see, e.g., [214]), where the most intense resonance, called the White Line (WL), represents the transition of a 1s electron (in the case of probing a K absorption edge) to an unoccupied dipole allowed np state. The spectrum is broadened by the life times of the core-hole and the excited photoelecton, as well as by the energy resolution of the experiment. However, the spectrum of an atom surrounded by other atoms in the solid, liquid or gas phase reveals fine structure at the absorption edge (pre-edge region) and smooth oscillations (shape resonance region) after the WL.

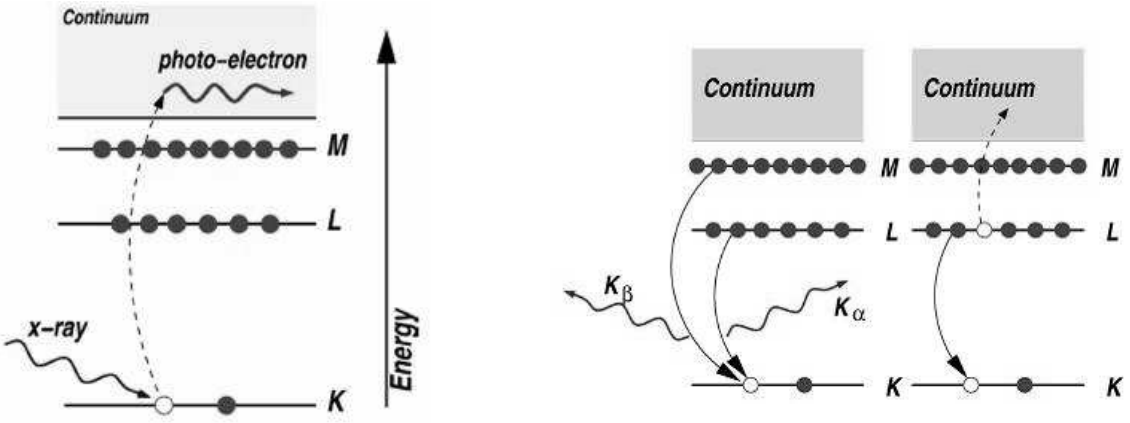

Figure 2.1: The photo-electric effect, in which an X-ray is absorbed and a core-level electron is promoted out of the atom (left). Decay of the excited state: X-ray fluorescence (middle) and the Auger effect (right). (from [133])

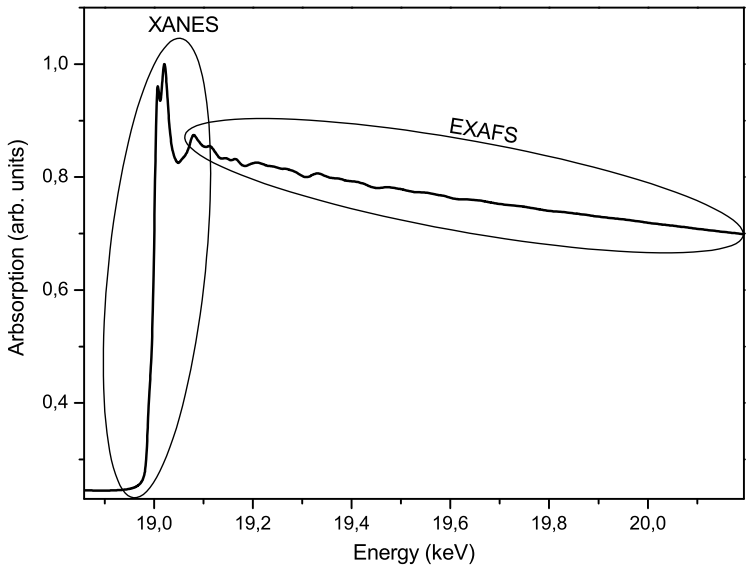

Figure 2.2: XAFS spectrum of $LiNbO_3$ measured at the Nb K-edge.

The resonances on the absorption edge represent mainly transitions to the lowest unoccupied states governed by the dipole selection rule ($\Delta l = \pm 1$, $\Delta J = 0, \pm 1$) (in some specific cases these resonances are due to quadrupole transitions). Multiple scattering of the photoelectron from the surrounding atoms mostly affect the shape resonance region of a XANES spectrum [150].

A XANES spectrum reflects the electronic structure and thus the atomic environment of the probed atom, therefore its interpretation is often complicated and based mainly on qualitative and empirical methods. In the last decade several theoretical codes became capable of calculating XANES spectra *ab initio*, but only in some cases with satisfactory agreement with the experimental spectra (see, e.g., [10, 23, 83, 126, 150]).

2.2.1 Qualitative interpretation of a XANES spectrum

The data reduction of a raw XANES spectrum includes background subtraction, i.e., regression and subtraction of a linear function from the pre-edge region. The energetically lower absorption edges (e.g., L, M... in the case of measurements at the K absorption edge of an element) and absorption from other elements in the studied material contribute to the background absorption. The pre-edge subtracted spectrum is divided by $\Delta\mu_0$ (see Sec. 2.3 for details on determination of $\Delta\mu_0$). The data reduction procedure is necessary for eliminating the influence of experimental effects and secondary absorption processes on the XANES spectrum, which is useful in the comparison of various XANES spectra and to make the signal concentration independent.

XANES fingerprinting refers to the comparison of the spectrum of interest with suitable reference spectra. The choice and availability of the "suitable reference spectra" often determines the success of this type of analysis. The energy positions of the absorption edge of the studied spectrum and the reference spectra are compared, as they depend on the formal oxidation state of the probed element in a compound. The XANES spectra of Cu, Cu_2O, CuO and $CuNb_2O_6$ with 0, +1 and +2 Cu formal oxidation state, respectively, measured at the Cu K-edge (8979 eV) are displayed in Figure 2.3. The higher the formal valence of the Cu atom the more the absorption edge is shifted towards higher energies. The size of the energy shift (~1 eV per valence number in this case of copper oxides) differs not only for the different elements, but also for the type of bonding partner and site symmetry of the atom. An illustrative example of this effect are the spectra of CuO (fourfold coordinated with oxygen atoms) and $CuNb_2O_6$ (sixfold coordinated with oxygen atoms). Cu has a formal oxidation state 2+ in both compounds but the absorption edge of $CuNb_2O_6$ is shifted towards higher energies.

There are several empirical methods for defining the energy position of the absorption edge of an element in a compound (see, e.g., [30, 136, 156, 201]). For example, the absorption edge is defined as the energy position of the first inflection point of a spectrum, which is determined by the maximum of the first intense peak from the first derivative of a spectrum or the zero of the second derivative. However, existence of various resonances on the absorption edge may hinder the successful determination of the energy shifts of absorption edges being compared by this method (see Fig. 6.2). In this case other features can be used. In order to define the formal oxidation state of an element in a studied compound, the dependence of the formal oxidation states from the energy positions of the absorption edges of the same element in different reference compounds is plotted. A linear regression is used as a calibration function (see Fig. 6.15). However, the formal oxidation state is not always a simple linear function of absorption edge in eV, which may lead to inaccurate results [30].

The resonances on the absorption edge can also serve for recognition of a formal oxidation state and symmetry of an element in a compound (see, e.g., [92, 159, 167]). The pre-edge peaks and WLs denoted with A in Fig. 2.3 in the spectra of Cu_2O, CuO and $CuNb_2O_6$ represent transitions of the 1s electron to 4p unoccupied states. In the spectrum of $CuNb_2O_6$ a weak resonance at around 8976 eV, marked with b, is present due to the transition of the 1s electron to the hybridized Cu3d-O2p molecular orbital (see Fig. 2.3, inset). This "mixing" of different types of atomic orbitals is possible only in compounds without inversion symmetry. This condition is satisfied by $CuNb_2O_6$ (distorted octahedral symmetry). It has been shown by Bocharov et al. [21] that in case of CuO this resonance is due to a quadrupole transition. Quadrupole transitions are forbidden by the dipole selection rule; they are present, though very weak, in the spectra of some transition metal oxides. This feature is not visible in the spectrum of Cu_2O and generally in Cu 1+ compounds, because of the completely

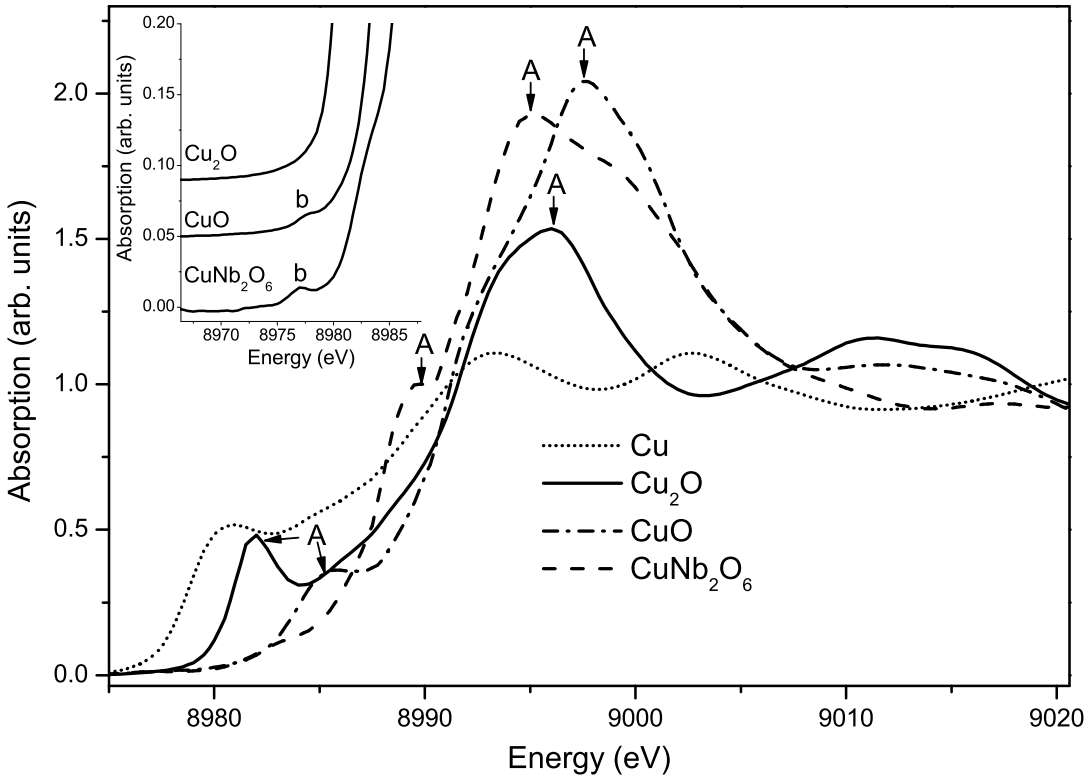

Figure 2.3: Cu K-edge XANES spectra of Cu, Cu_2O, CuO and $CuNb_2O_6$. Part of the pre-edge region is magnified in the inset.

filled 3d state [92].

2.2.2 Quantitative interpretation of a XANES spectrum

The FEFF8.2 (see [10, 55, 153]) code is one of the most successful *ab initio* theoretical codes developed in the last decades, capable of calculating XANES and EXAFS spectra, with calculations of XANES spectra being the more challenging of the two. A brief outline of the basic principles of the theory implemented in the FEFF8.2 code will be given in the following. The other popular codes like StoBe, based on Density Functional Theory (DFT) [83], SPRKKR [172], based on band structure theory, were not used in the present work; therefore they are not discussed.

In order to calculate XAFS spectra, Fermi's golden rule (2.3), which gives the probability for a transition, in the one electron [153] and dipole approximation [183] should be solved. In the frame of the Multiple Scattering Theory (MST) applied in the FEFF8.2 code, Fermi's golden rule is rewritten using the Green's function. The Hamiltonian of the system is $H = Ho + V_{int} + \delta V$, where the atoms are represented as ions and electrons. The ions are scattering sites with spherical symmetric potential δV and V_{int} is the flat interstitial potential [150]. The atoms are positioned according to the input Cartesian coordinates, forming a potential called a muffin tin potential. The one particle Green's function is written as

$$G(E) = 1/(E + H + i\zeta). \tag{2.4}$$

Fermi's golden rule (2.3) can be written using the Green's function $\sum_f |f\rangle G(E)\langle i|$

$$\mu(E) \propto -\frac{1}{\pi}\mathrm{Im}\langle i|\hat{\epsilon}^* \cdot \mathbf{r}G(E)\hat{\epsilon} \cdot \mathbf{r}|i\rangle\Theta(E - E_F). \tag{2.5}$$

Θ is the Heaviside step function, which guarantees that the cross section is different from zero only above the Fermi energy, E_F. G is the full one electron propagator in the presence of a scattering potential, which can be presented as a Taylor expansion.

$$G = G^0 + G^0tG^0 + G^0tG^0tG^0 \tag{2.6}$$

$$G = (1 - G^0t)^{-1}G^0 \tag{2.7}$$

G describes all possible ways the photoelectron can scatter from the surrounding atoms before the core-hole is refilled. G^0 shows how the photoelectron propagates between two scattering sites and t describes how the photoelectron scatters from an atom. The solution of equation 2.6 leads to the EXAFS spectrum, where for the XANES spectrum the trace of the matrix G corresponding to the absorbing atom and the photoelectron final state are used to compute the multiple scattering fine structure function $\chi(E)$. The absorption cross section is

$$\mu(\varepsilon) = \mu_0(\varepsilon)[1 + \chi_l(\varepsilon)], \varepsilon = E - E_0 \tag{2.8}$$

μ_0 is the smoothly varying embedded atomic background and l is the final state angular momentum. The two most important approximations applied in calculations of XANES spectra are the Full Multiple Scattering (FMS) and Self Consistent Field (SCF) approximations (see, e.g, [150] and [153]). In the FMS approximation all possible scattering ways (called single and multiple scattering paths) of the photoelectron from the atoms in a cluster are taken into account. FMS is computationally "expensive" and it is usually done on a small cluster of about 30 atoms around the absorbing atom.

The FEFF8.2 code computes XANES and EXAFS spectra, l projected Density of States (l-DOS) and charge distributions. Detailed description of the computational steps applied in the code are given in [153]. The FEFF8.2 code has proven to reproduce semi-qualitatively, e.g., the spectral features of the XANES spectra of transition metal oxides (see, e.g., [127]). The agreement is usually good enough to study the influence of size effects, structural distortions, vacancies or dopants on the spectral features (see, e.g., [134, 150, 155, 197]). These systematic studies are achieved by modifying the atomic coordinates of the cluster of atoms employed in the calculation. Around 100 atoms are usually sufficient to calculate a XANES spectrum of a bulk material. The calculated Cu K-edge XANES spectra based on Cu incorporated into Li or Nb sites models, shown in Figure 2.4, illustrate the potential of this type of analysis. These simulations are performed by simple substitution of the absorbing Li or Nb atoms by a Cu atom in the input file. The difference in the two spectra is remarkable and it can be used for recognition of the Cu incorporation site by direct comparison with an experimental spectrum [134]. This type of analysis naturally complements the EXAFS analysis, which is sensitive to the short range atomic environment of the absorbing atom.

Another strength of the FEFF8.2 code is the ability to calculate l-DOS (see, e.g., [126, 136]. One example is shown in Figure 2.5. The s, p and d DOS of Cu and s and p DOS of O are plotted along with the simulated copper-doped LN K-edge XANES spectrum. As it is expected from the dipole

selection rule, the Cu p-projected DOS above the Fermi energy (E_F) fully describes the overall shape of the XANES spectrum. This is a good demonstration of how the XANES spectrum reflects the density of unoccupied states. For example, the calculations reveal that XANES resonance A (see Fig. 2.5) is due to transitions to a molecular orbital, which is formed mainly by 5s orbitals of the Cu atom, but a small admixture of O p orbitals is also present. In the same manner, the resonance B is assigned to transitions to the hybridized s and p atomic orbitals of copper, where C is due to transition of the 1s electron to a Molecular Orbital (MO), which contains mainly p type Atomic Orbitals (AOs) of Cu, but also a small amount of O p type AOs. Clearly, l-DOS enables assigning the various XANES resonances to transition of the 1s electron to a particular type of MO.

In order to describe the next widely applied fingerprinting approach for quantitative evaluation of a XANES spectrum, attention should be drawn again to Figure 2.3. Cu_2O, CuO and $CuNb_2O_6$ have different crystal structures, i.e., cubic, monoclinic and orthorhombic, which are reflected in the different overall shapes of their XANES spectra. The ability of the XANES spectrum to fingerprint the structure of a material is used to identify the compounds and their quantities in a heterogeneous sample through linear combination least-square fitting analysis (see, e.g., [134] and [15]) or Principle Component Analysis (see, e.g, [15]). The former is applied in Section 6.1.4 and consists of the comparison of an experimental spectrum with a weighted addition of reference XANES spectra, representing species, which are expected to be a part of the "unknown" material.

2.3 The EXAFS spectrum

The EXAFS spectrum is intuitively understood by considering the wave-particle duality of the photoelectron ($\lambda = \hbar/p$). When a photoelectron, which can be represented as a spherical wave, leaves the atom, it scatters on the surrounding atoms and at position close to the origin (the bound core electron) the incoming and outgoing photoelectron waves interfere constructively or destructively modulating the absorption coefficient (see 2.6). Only elastically scattered photoelectron-waves contribute to the EXAFS oscillations and moreover, only if the photoelectron wave reaches the absorbing atom before the core-hole is refilled. The measured interference pattern, i.e., the EXAFS spectrum, can be described as a sum of sinusoidal waves where the amplitude and frequency of the sinusoidal modulations depend on the number and type j of neighboring atoms and their distance from the absorbing atom i (r_j):

$$\chi(k) = \sum_j A_j(k) \sin(2kr_j + \phi_{ij}(k)), \tag{2.9}$$

k is the wave number of the photoelectron:

$$k = \sqrt{\frac{2m}{\hbar^2}(E - E_0)}, \tag{2.10}$$

where m is the mass of the electron, E is the incident photon energy and E_0 is the threshold energy of the absorption edge. In k space each wave is characterized by an $\phi_{ij}(k)$ function, which is the total photoelectron phase shift including the twice the phase shift by the absorbing atom (Columbic type of interaction) and one phase shift caused by the scattering process, and an amplitude:

$$A_j(k) = N_j S_0^2(k) F_j(k) e^{-2\sigma_j^2 k^2} e^{-2r_j/\lambda_j(k)} / (kr_j^2). \tag{2.11}$$

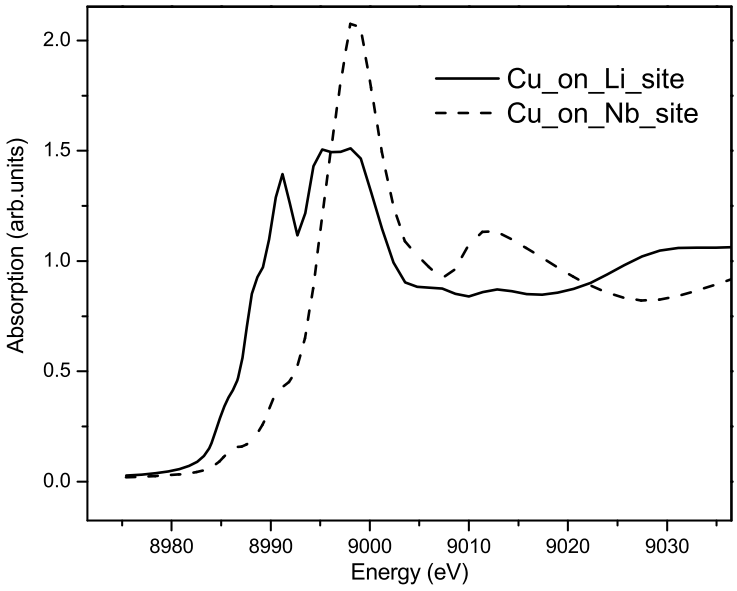

Figure 2.4: Cu K-edge XANES spectra of copper-doped $LiNbO_3$ calculated with the FEFF8.2 code employing the Cu incorporated into the Li or Nb site models.

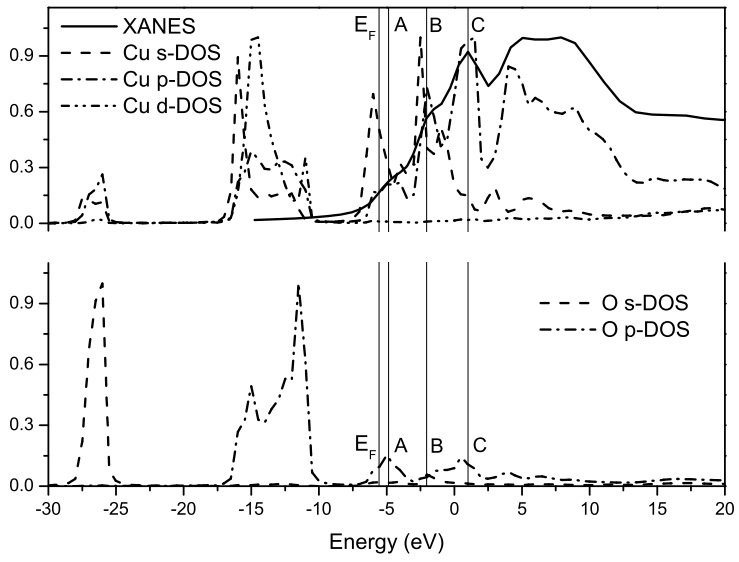

Figure 2.5: Cu K-edge XANES and l-projected Density of States (l-DOS) of copper-doped $LiNbO_3$ calculated employing the Cu incorporated into the Li site model.

$F_j(k)$ is the backscattering amplitude, which depends on the type j of the scattering atoms. N_j is the number of scatterers from type j, it is also called coordination number; r is the distance absorber-

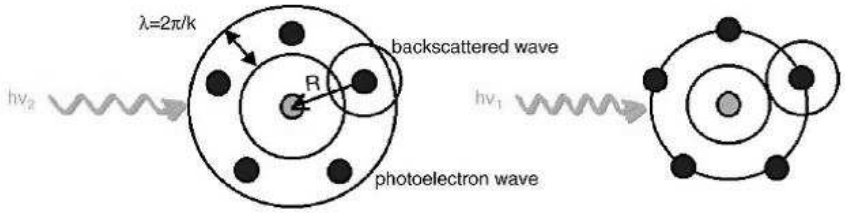

Figure 2.6: Illustration of destructive (left) and constructive (right) interference of outgoing photoelectron wave and backscattered wave, which lead to minima and maxima of the oscillations in μ observed in the EXAFS regime. (from [44])

neighboring atom; $e^{-2\sigma_j^2 k^2}$ accounts for the disorder in the lattice, i.e., σ_j^2 is the similar Debye-Waller factor, which includes the static disorder and thermal vibrations of the atoms; $e^{-2r_j/\lambda_j(k)}$ is due to inelastic losses during the scattering process, where λ is the mean free path of the photoelectron. $S_0^2(k)$ is the amplitude reduction factor, which is due to many-body effects, i.e., other transitions in the atom, e.g., shake-off effects, etc. A detailed information on the multiple scattering theory, explaining the EXAFS oscillations in detail can be found in [153, 162, 174, 175, 180, 183].

2.3.1 Quantitative interpretation of an EXAFS spectrum

The EXAFS equation (2.9), using theoretically calculated scattering phases ($\phi_{ij}(k)$) and amplitudes ($F_j(k)$), is successfully employed in this and hundreds of other studies for determining distance, type and number of near neighboring atoms, as well as the structural disorder in an unknown material. Depending on the quality of the experimental data, reliable structural values can be achieved up to 6 Å away from the absorbing atom. The errors for the obtained coordination numbers could be up to 30%, where the obtained values for the distances are more accurate, often with error bars of about ± 0.01 Å. This value includes the statistical error. The spatial resolution in EXAFS is inversely proportional to the measured spectral range $\Delta R \sim 1/\Delta k$ [183]. Distances (the same type of neighboring atom) with difference (ΔR) up to ≈ 0.07 Å can be resolved ($\Delta k = 15$ Å) (see, e.g., [152]).

The first step in the EXAFS analysis is to isolate the scattering function $\chi(E)$ from the measured XAFS spectrum:

$$\chi(E) = \frac{\mu(E) - \mu_0(E)}{\Delta\mu_0(E_0)}. \tag{2.12}$$

μ_0 is the absorption of a single embedded atom, which is removed by removing a smooth post-edge background function (see Fig. 2.7 a)). The background function can be determined for example by using theoretical standards; a method suggested by Shelly Kelly (for details see [93]). $\Delta\mu_0$ is the difference in absorption between the post-edge and pre-edge regions, which are regressed with lines and extrapolated at the threshold E_0. These two steps are executed by the program AUTOBK [14].

In the next step the $\chi(E)$ function is converted from E to k units, using relation 2.10 (see Fig.2.7 b)). In order to Fourier Transform (FT) the $\chi(k)$ spectrum to R space, the appropriate k range, the type of window and window sills are chosen. The upper limit of the k range is at the point where noise

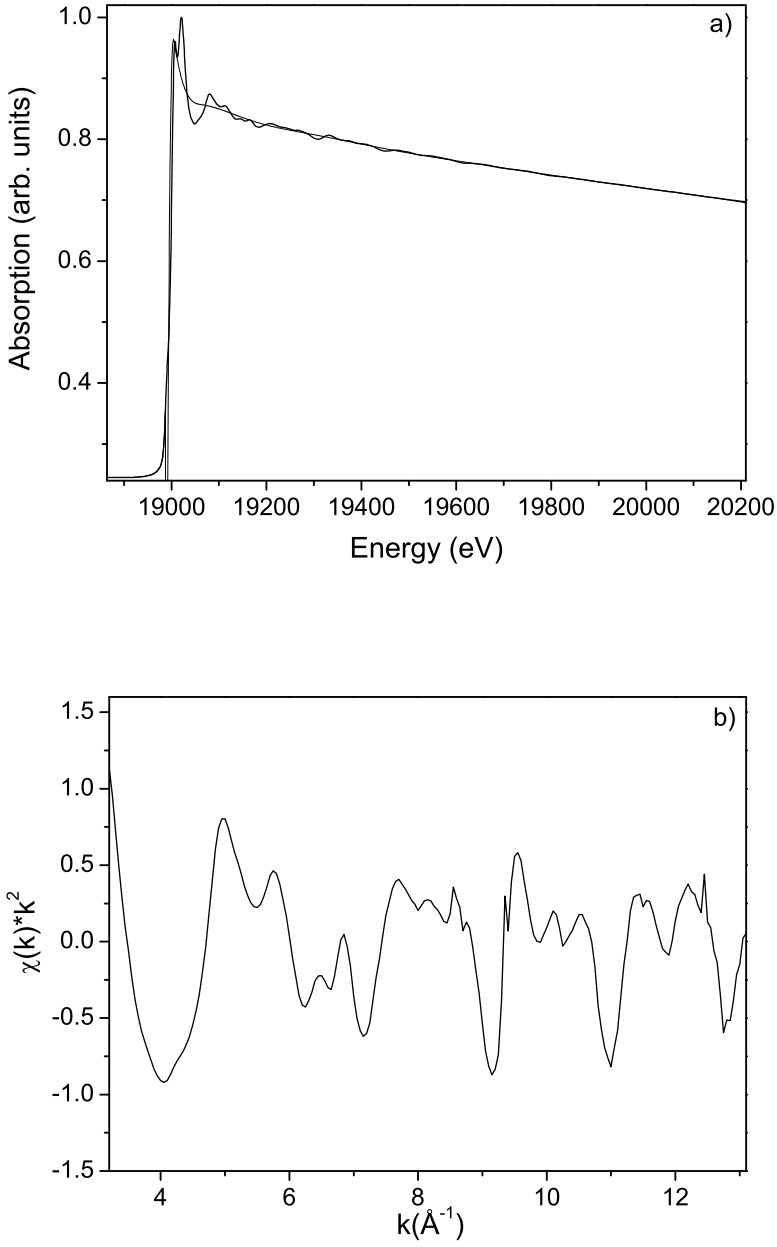

Figure 2.7: Nb K-edge EXAFS spectrum of $LiNbO_3$ in E a) and k spaces b)

begins to dominate the signal. In order to compensate for the fact that $\chi(k)$ is a finite function, $\chi(k)$ is multiplied by a window. Practice has shown that Kaiser-Bessel or Hanning windows are suited for most experimental cases. The amplitude of $\chi(k)$ decays with k, which damps the signal especially for light scattering atoms. One solution to this problem is to weight $\chi(k)$ by k, k^2 or k^3. However, the quality of subsequent fits should not depend on the weighting. One approach

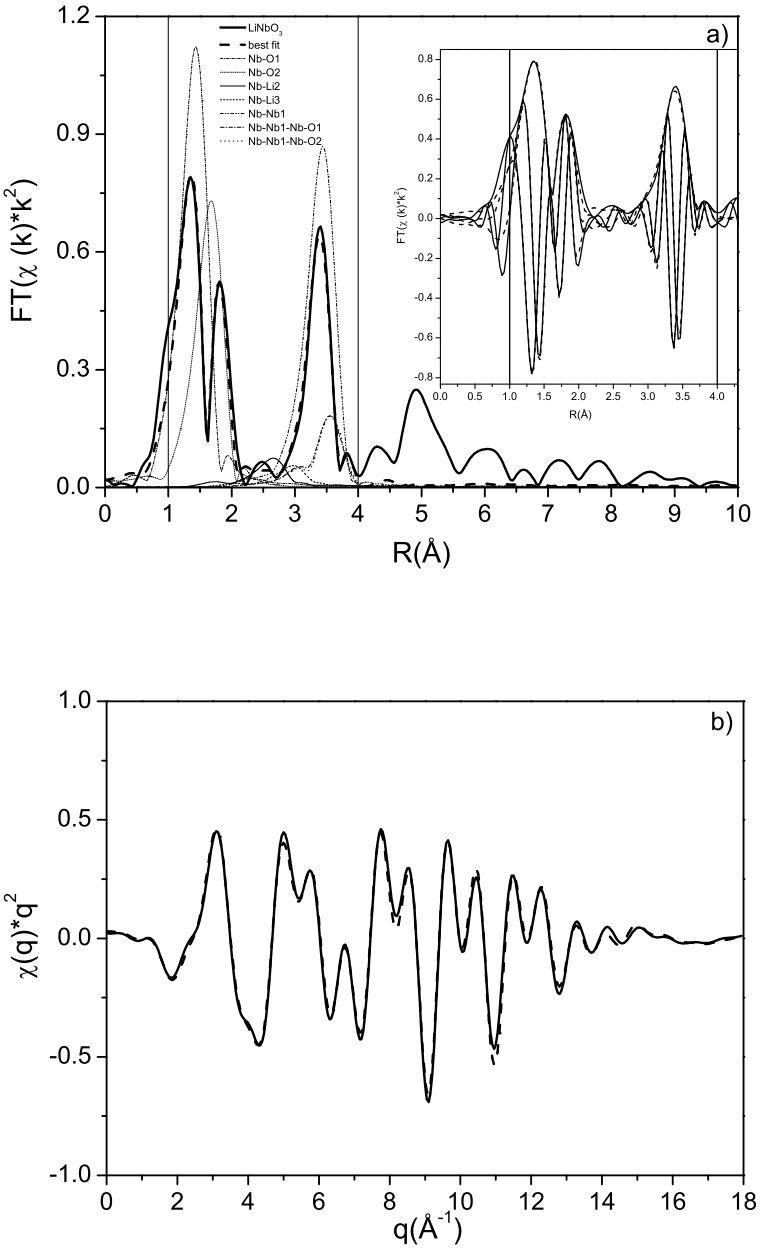

Figure 2.8: Nb K-edge EXAFS spectrum of $LiNbO_3$ (solid) and its best fit (dash) in R space (together with the individual scattering paths used in the fit) a) and q space b). The imaginary and real parts of the FT EXAFS spectrum in R space are plotted in the inset of a).

for testing the reliability of obtained structural parameters is to perform the fit with the three k weightings simultaneously. This has been done in all EXAFS analyses in this thesis.

The $\chi(R)$ spectrum is similar to a Radial Distribution Function (RDF), where the intense peaks, called also coordination shells, are at distances corresponding to the distance of the absorber-

neighboring atoms (see Fig. 2.8 a)). The amplitudes of the peaks depend on the number of atoms at the respective distances. Usually, the spectrum is shown "not-phase corrected", which means that these characteristic peaks appear at lower distances than the actual interatomic distances. Practice has shown that the most suitable way for extracting the structural information from the experimental FT EXAFS spectrum is to follow a shell-by-shell fit approach. First, a structure as close as possible to the "unknown" is chosen, using structure databases, e.g., Inorganic Crystal Structure Database (ICSD) [87]. The information about the basis and the point group symmetry of the chosen material is used as an input file in a program called ATOMS [13], which creates a list of atomic coordinates used as an input file to FEFF [55]. The FEFF program calculates the backscattering amplitudes ($F_j(k)$) and phase shifts ($\phi_{ij}(k)$) and provides single and multiple scattering paths, which are used in modeling the FT EXAFS experimental spectrum. One single scattering path is created for the same type of atoms at the same distance. The fit is done with the program FEFFIT [56], which takes as input the $\chi(k)$ spectrum and the theoretical single and multiple scattering paths needed for the chosen fit region. There are five parameters from the EXAFS equation for each scattering path, which are either unknown and varied or known and fixed during the fit. In the case of known structure, N and r will be hold constant at set values, whereas S_0^2, ΔE_0 and σ^2 will be varied. After the best parameters of the included paths are found by using numerical methods, they are summed and this theoretical spectrum is compared with experiment. There are several measures of the quality of the fit. To find the best fit during the fitting procedure

$$\chi^2 = \sum_{i=1}^{N_{ind}} \left(\frac{-f_i}{\epsilon_i} \right)^2 \tag{2.13}$$

is minimized. χ^2 depends on the square of the difference between data and fit f_i at each point in R or q space and uncertainty ϵ_i. Here N_{ind} is the number of independent data points

$$N_{ind} = \frac{2 * (kmax - kmin) * (Rmax - Rmin)}{\pi} + 2. \tag{2.14}$$

The problem of this statistical measure is that for a good fit it should be approximately equal to 1 but the practice shows that for concentrated samples it is between 10 and 100. ϵ_i accounts for this discrepancy, which generally includes random and systematic errors, but only the former are considered during the fit. $\frac{\chi^2}{\nu}$ is used for comparison of two fits which have the same $\Re$ factor of fit. ν is the degree of freedom in the fit, defined as $N_{ind} - N_{varys}$, where N_{varys} is the number of variables in the fit. The $\Re$ factor of the fit is defined as:

$$\Re = \frac{\sum_{i=1}^{N} \left\{ [\Re(f_i)]^2 + [Im(f_i)]^2 \right\}}{\sum_{i=1}^{N} \{ [Re(\chi data_i)]^2 + [Im(\chi data_i)]^2 \}}. \tag{2.15}$$

$\Re \leq 0.02$ is considered a good fit. During the fit procedure, the physical meaning of the parameters, the size of their error bars and their correlations should be considered.

The structural parameters (up to 4 Å) from the fit of a Nb K-edge FT EXAFS spectrum of a congruently-melting LN crystal are given in Table 2.1. The amplitude reduction factor S_0^2 was set to 1 during the fit. The $\Re$ factor of fit was 0.01. There are 6 O atoms at two different distances in the first coordination shell. The well separated two peaks, at around 1.5 Å, were fit with two

atom type	N	R (Å)	σ^2 (Å^2)	ΔE_0 (eV)	Nm	Rm (Å)
O1	3.2 ± 0.3	1.88 ± 0.01	0.004 ± 0.0040	9.1 ± 0.3	3	1.89
O2	2.8 ± 0.3	2.13 ± 0.01	0.004 ± 0.0040	9.1 ± 0.3	3	2.11
Nb1	6.5 ± 0.7	3.75 ± 0.01	0.005 ± 0.0003	6.2 ± 0.8	6	3.76
Li1					1	3.01
Li2	3.0 ± 0.8	3.12 ± 0.03	0.005 ± 0.0003	9.1 ± 0.3	3	3.05
Li3	3.0 ± 1.5	3.44 ± 0.03	0.005 ± 0.0003	9.1 ± 0.3	3	3.38
Nb-Nb1-O1-Nb	6.0	3.87 ± 0.01	0.005 ± 0.0010	7.6 ± 0.5	6	3.88
Nb-Nb1-O2-Nb	6.0	3.88 ± 0.01	0.004 ± 0.0010	7.6 ± 0.5	6	3.88

Table 2.1: Results from the EXAFS analysis of a Nb K-edge EXAFS spectrum of LN. The type of atom neighboring the absorbing Nb atom is given in the first column. The structural parameters from the fit are in the remaining columns: N: coordination numbers, R (Å) distances, Debye-Waller factors: σ^2 (Å^2), ΔE_0 energy shift of the ionization potential (eV), Nm and Rm coordination numbers and distance, respectively, for the initial used model (ICSD 28294).

Nb-O single scattering paths. Best agreement between data and model was achieved by fitting the second coordination shell with two Nb-Li single scattering paths. The low scattering amplitude of Li is not expected to contribute significantly in the EXAFS signal. However, this is the most significant contribution at this distance.The reduced $\mathfrak{R}$ factor of fit and $\frac{\chi^2}{\nu}$ justify the use of these single scattering paths. The pronounced peak at about 3.5 Å was fit with a Nb-Nb single scattering path and two double scattering paths.

Chapter 3

Fundamentals of High Resolution X-ray Emission Spectroscopy (HRXES)

If XAS probes density of unoccupied states of an atom, X-ray Emission Spectroscopy (XES) probes density of occupied states and this makes the two techniques complimentary. However, the usefulness of the X-ray emission spectra measured with a conventional solid-state detector is very limited, because of their low energy resolution [~ 150 eV (FWHM)], which allows to resolve only the main Kα and Kβ lines. An energy resolution down to 1 eV (FWHM) is possible by monochromatizing the emitted photons by an analyzer crystal (see Sec. 4.3). This is the attainable energy resolution with the spectrometer used in this experiment [196]. Examples of some of the possible applications, mainly concerning transition metal oxides, and their advantages will be given in this chapter.

3.1 Non-resonant HRXES

When a 1s electron is excited well above the Fermi level, the atom relaxes, leading to emission of the intense Kα (2p-1s transition) and Kβ (3p or valence band-1s transitions) lines (see Fig. 3.1 a)). The spin-orbit coupling splits the Kα line, which is around 8 times more intense than the K$\beta_{1,3}$ line, into a Kα_1 and a Kα_2 lines. The exchange interaction between the unpaired 3d valence electrons and the created 2p hole is very weak, therefore these emission lines exhibit weak chemical sensitivity [64]. The Kα lines of series of Mn oxides are shown in Figure 3.1. When the formal oxidation state of Mn increases, the number of spin-up electrons in the 3d state decreases, i.e., the ground state valence configurations of Mn(II), Mn(IV) and Mn(VII) are $3d^5$, $3d^3$ and $3d^0$ respectively; as a result, the two Kα lines become more narrow and the Kα_2 line shifts towards lower energies. The exchange interaction is stronger in the case of the Kβ line and with the increase of the number of spin-up electrons in the 3d state, a satellite peak Kβ' rises on the low energy site of the K$\beta_{1,3}$ peak; in addition, the main and satellite peaks move towards each other. Kβ' and K$\beta_{1,3}$ peaks represent the 3p-1s spin-up and spin-down transitions, respectively [43, 49, 64, 65, 144, 147].

The shape of the K$\beta_{1,3}$ emission line is also sensitive to the formal oxidation state and the chemical environment of an element. This fingerprint of an oxidation state is used in Section 6.2.4 in a valence study of manganese-doped LN crystals.

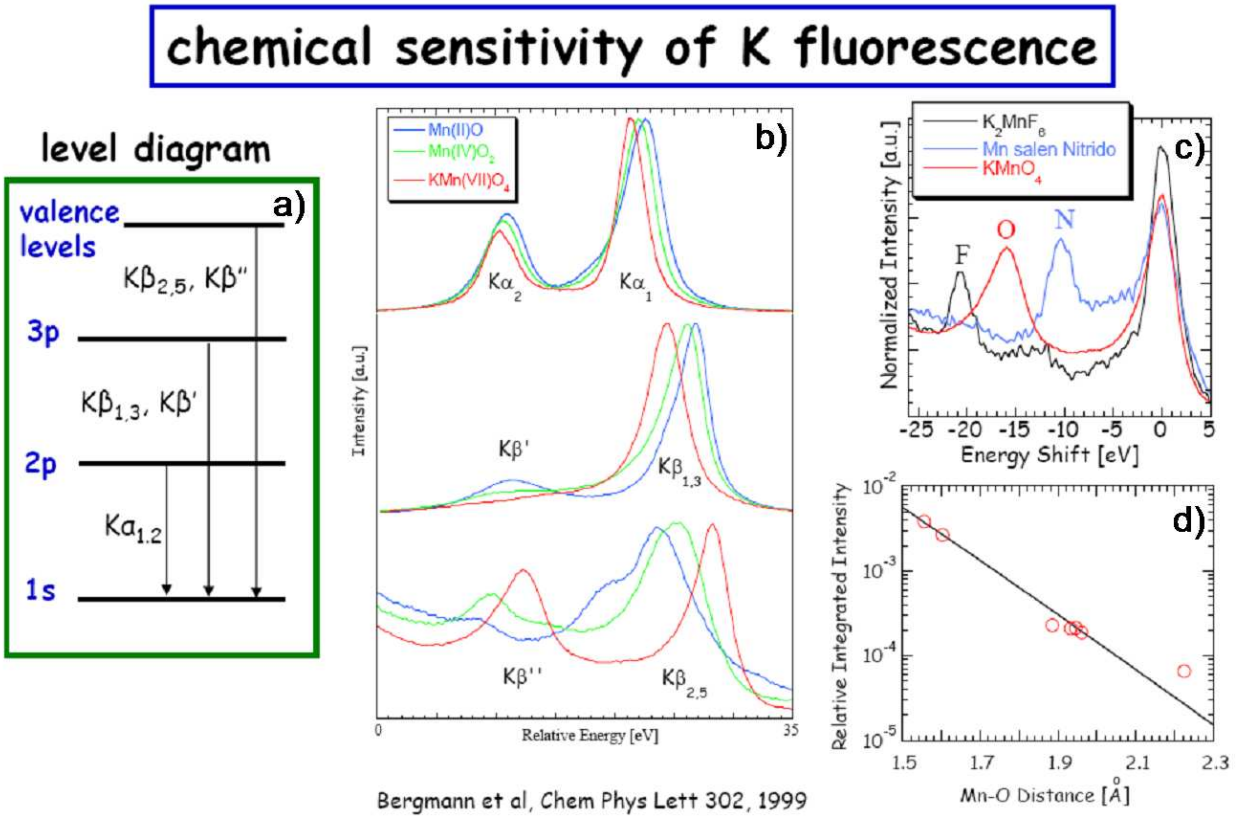

Figure 3.1: A level diagram a); Kα and Kβ emission lines of MnO, MnO_2 and $KMnO_4$ b); K$\beta_{2,5}$ and Kβ'' emission lines of K_2MnF_6, Mn Salen Nitrido and $KMnO_4$ c); the amplitude dependence of the Kβ'' peak from the Mn-O distance d). (from Uwe Bergmann's talk given on 15th of March, 2004 in Upton, NY [182])

The satellite K$\beta_{2,5}$ emission line (transitions of metal and ligand electrons, which contribute to the p metal occupied density of states) and the cross-over peak Kβ'' [electrons from the ligand valence levels [17]] (see Fig. 3.1 a) and b)) have ~ 500 times less intensity than the Kα lines [64]. However, they exhibit the strongest chemical sensitivity, directly probing the type of ligand and its distance to the absorbing atom. By integrating the intensity of the Kβ'' peak, the Mn-O distance can be found (see Fig. 3.1 b) and d)). The energy position of the cross-over peak depends on the type of ligand (see Fig. 3.1 c))[17].

Clearly, in the case of transition metal oxides, the emission lines show a pronounced chemical sensitivity, which in some cases enables determination of the formal oxidation state of an element, the type of ligand and its distance to the probed atom. How this sensitivity can be used for obtaining spin and site and/or valence selective XAFS spectra is shown in Section 3.2.1.

3.2 Resonant HRXES

In the resonant HRXES, which is also called Resonance Inelastic X-ray Scattering (RIXS), the 1s electron is excited to the lowest unoccupied states, i.e., varying the excitation energy, and the

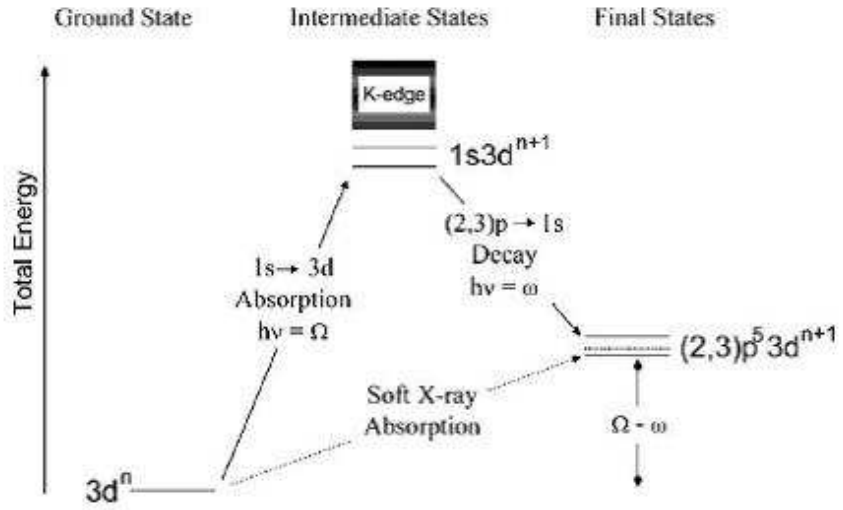

Figure 3.2: RIXS energy scheme for 1s(2,3)p RIXS in a transition metal ion. For simplicity, atomic configurations are used and only 1s-3d excitations are shown. (from [64])

intensity of the Kα (1s2p RIXS) or Kβ (1s3p RIXS) emission lines is recorded.

The RIXS or the Resonant X-ray Emission (RXE) are described by the Kramer-Heisenberg formula (see, e.g., [61, 103])

$$F(\Omega,\omega) = \sum_f \left| \sum_n \frac{\langle f|T_2|n\rangle\langle g|T_1|n\rangle}{E_g - E_n + \Omega - i\Gamma_K/2} \right|^2 x \frac{\Gamma_f/2\pi}{(E_g - E_f + \Omega - \omega)^2 + \Gamma_f^2/4}, \tag{3.1}$$

where $|n\rangle$ is the intermediate state, which is reached from the ground state $|g\rangle$ via the transition operator T_1. The intermediate state in RIXS is the final state in K-edge XAS. T_1 depends on the local symmetry of the metal ion and it can be dipole or quadrupole, where T_2 is a dipole transition operator, because the final states $|f\rangle$ are reached via 2p or 3p-1s transition. The three states can be written by using atomic configurations: $|g\rangle = 3d^n$, $|n\rangle = 1s3d^{n+1}$ (1s electron is resonantly excited into a 3d orbital) and $|f\rangle = (2,3)p^5 3d^{n+1}$ (a core hole in the 2p or 3d shell and an additional electron in the 3d orbital). The final state is identical to the X-ray L or M-edge absorption final states [43, 64]. Γ_K and Γ_f are the lifetime broadenings for the intermediate and final states respectively, whereas the experimental spectrum will be broadened also by the energy resolutions of the primary monochromator and the analyzer crystal.

The RIXS spectra can be plotted as a surface (see, e.g., [64]), contour (see, e.g., [64]), waterfall (see, e.g., Figure 3.3 left, where an extended 1s2p RIXS plot is shown) or line plot (see Fig. 3.3 right). In the first three types of plots, the recorded intensity of the Kα or Kβ emission lines is plotted versus a two-dimensional grid. One of the axis is the excitation energy Ω, while the second axis can be the energy transfer $\Omega - \omega$ or the emission energy ω.

The Kα emission lines of wet chemically synthesized Co nanoparticles [20] measured at excitation energies below and above the K absorption edge of Co (7709 eV) are shown as line plots in Figure 3.3 right. Three peaks, denoted as A, B+C and D, are visible in the emission spectra. The intensity of the B+C and D peaks increases by increasing the excitation energy, where peak A merges with

peak B+C (not shown in this plot, see [190]). Peak A might be assigned to an electronic transition or it might be the Kα_2 emission line of a second cobalt species in the studied material. The shift of the Kα lines to higher energies, as the excitation energy increases (energies below an absorption edge) has been observed in 1s2p RIXS studies of CuO (see [77, 78, 185]). As it was shown in Section 3.1, the energy shift of the Kα lines of an element in different valence states is small, leading to overlap of the emission lines off resonance; as a result, by probing a compound with mixed-valence states of an element, only one pair of Kα emission lines (Kα_1 and Kα_2) is observed (see, e.g., [66, 88]). However, Figure 3.3 right suggests that high-resolution and high-intensity RIXS spectra can be used for detecting different chemical species of an element in a complex compound, identifying them by comparison with RIXS spectra of suitable reference compounds.

The RIXS spectra are also extremely useful for revealing transitions to electronic states, which are observed in calculated but not in conventionally measured XANES spectra (see, e.g., [77, 78]). For example, Hayashi et al. reported weak emission lines in his 1s2p RIXS of CuO and assigned them to Cu 1s to $4p'_z$ dipole transition, which should be visible at about 8983 eV in the experimental XANES absorption spectrum [77]. Resonance is missing at this energy in the experimental XANES spectrum. However, Bocharov et al. observed such a feature in his real-space multiple-scattering calculation study of CuO [21].

By plotting the emission intensity as a function of the energy transfer, line plots similar to the conventionally measured LIII and LII (1s2p RIXS) or MIII and MII (1s3p RIXS) XANES spectra are obtained (see, e.g., [43, 64, 103, 114]). However, the intrinsically low core-hole lifetime broadenings of the L and M states require better than 1 eV experimental resolution [42, 68], which will allow to resolve better the XANES features; an improved resolution permits a full exploitation of the potential of this technique (see, e.g., [35]). The possibility for measuring soft X-ray absorption spectra with hard X-rays gives the great advantage to perform the experiment in ambient conditions.

More examples of RIXS studies can be found in [51, 67, 80, 96, 108, 132, 165].

3.2.1 Extended resonant HRXES

The extended resonant HRXE map goes beyond the absorption edge and includes also non-resonant X-ray emission.

Spin selective XANES

The intensity of the Kβ' peak vanishes in the pre-edge regions of RIXS spectra of transition metal compounds with filled spin-up 3d electronic states (see, e.g., [79, 81, 145, 146]). The spin selectivity of the Kβ lines is discussed in Section 3.1. This effect is demonstrated in Figures 3.4 and 3.5 left, where the 1s3p RIXS maps of Fe_2O_3 and Fe_3O_4 are plotted. The valence band configurations of Fe_2O_3 is $3d^5$, whereas Fe_3O_4 is a mixture of FeO ($3d^6$) and Fe_2O_3. In Figures 3.4 and 3.5 right, the XANES spectra, obtained by integrating an emission band ± 0.5 eV around the maximum of the Kβ' and K$\beta_{1,3}$ peaks, are plotted along XANES spectra of Fe_2O_3 and Fe_3O_4 measured in transmission mode. Except for the low intensity in the pre-edge region of the Fe_2O_3 - Kβ' spectrum, which is possibly noise, no intensity is visible in this region (see Fig. 3.4 inset) in the XANES spectra extracted from the Kβ' emission lines. Moreover, the energy positions, intensities and shapes of the WLs and the A resonances, which are partially assigned to transitions to p-type of unoccupied states, tend also to exhibit spin selectivity.

Examples of spin-selective XANES and/or XE studies can be seen in the following references: [79, 81, 144, 160, 187–189]

Site and/or valence selective XANES

The chemical sensitivity of the Kβ and Kα emission lines is successfully employed in extracting partially valence and/or site-selective XANES and EXAFS spectra [40, 66, 71, 88, 145, 146, 209]. The selectivity is achieved by tuning the analyzer crystal to the maximum of the Kα_1 or K$\beta_{1,3}$ emission line of each valence species in a mixed-valence compound, while the excitation energy is scanned through the absorption edge of the chosen element. Instead of monitoring the maximum emission intensity, an emission band around the emission energy at half maximum of the Kα_1 or K$\beta_{1,3}$ emission lines can be integrated (see Section 6.3.4). Another possible approach is to use the spin selectivity of the Kβ lines. In the case of wet chemically synthesized Co nanoparticles protected by a smooth oxidation procedure, the metal cobalt core is covered by an protective shell formed by cobalt oxides or more complex cobalt compounds. It is extremely difficult to distinguish these additional species from a conventional XANES spectrum because of their 10-20% contribution. Since the Kβ emission line of Co^0 does not have intensity in the satellite Kβ' region (see [94]), its contribution is filtered out by integrating this region resulting with XANES spectral features sensitive to the complex cobalt species.

The cross-over peak Kβ'' is extremely valuable for obtaining ligand selective XANES spectra (see Fig. 3.1). However, its low intensity restricts these type of experiments to third generation synchrotron radiation facilities.

High-resolution XANES

The Mn K-edge XANES spectra obtained from 1s3p RIXS maps of MnO, Mn_2O_3 and MnO_2 are plotted along with Mn K-edge XANES spectra measured in fluorescence mode in Figures 3.6, 3.7 and 3.8. In order to obtain spectra with high signal-to-noise ratio, only the K$\beta_{1,3}$ line is monitored. The pre-edges of all XANES spectra extracted from the RIXS have considerably higher intensity and are better separated from the main absorption edge compared to the respective of the MnO, Mn_2O_3 and MnO_2 XANES spectra. In addition, sharpening of all resonances from the MnO - K$\beta_{1,3}$, Mn_2O_3 - K$\beta_{1,3}$ and MnO_2 - K$\beta_{1,3}$ XANES spectra is also visible. The often insufficient experimental energy resolution in conventional XAFS measurements prevent from fully exploiting the potential of the pre-edge resonances of transition metal oxides, which are extremely valuable for determining site-symmetry and valency of a probed element [18, 41, 42, 67, 68, 82, 181] .

However, despite the gain in quality, the experimental resolution of the here presented spectra is lower than the K-edge core-hole lifetime broadenings of Fe and Mn, which restricts the usefulness of the measured pre-edges. For example, the crystal field splitting of the 3d state of Fe_2O_3 is not resolved in the Fe_2O_3 - K$\beta_{1,3}$ XANES spectrum (see Fig. 3.4). In a 1s2p RIXS study of Caliebe et al. with 0.45 eV experimental energy resolution, the pre-edge peak reveals a complex structure [35]. Similar experimental energy resolution (0.5 eV at 6 keV) is achieved by M. Wilke in conventional Fe K-edge XANES measurements by employing a Si (111) four-crystal monochromator [200].

It is possible to extract core-hole lifetime-broadening-suppressed K and L edge XANES spectra from RIXS maps by employing the Kramers-Heisenberg formula. For examples see [41, 78, 80].

Extended EXAFS

In many complex systems, the usable EXAFS range is restricted by the absorption of an element, which is present in the sample but is not of interest. The same problem occurs when EXAFS is measured at a LIII edge, because of the energetically close LII absorption edge. By tuning the analyzer crystal to the emission energy of interest, the undesired emission is filtered out. In this way, an extended EXAFS range is measured, which allows better resolution [148, 209].

A tremendous reduction of the background emission (emission from heavy elements and scattered photons) is achieved (see, e.g., [89, 90]) by selecting with an analyzer crystal the emitted photons of a element with a trace amount in a heavy-matrix sample.

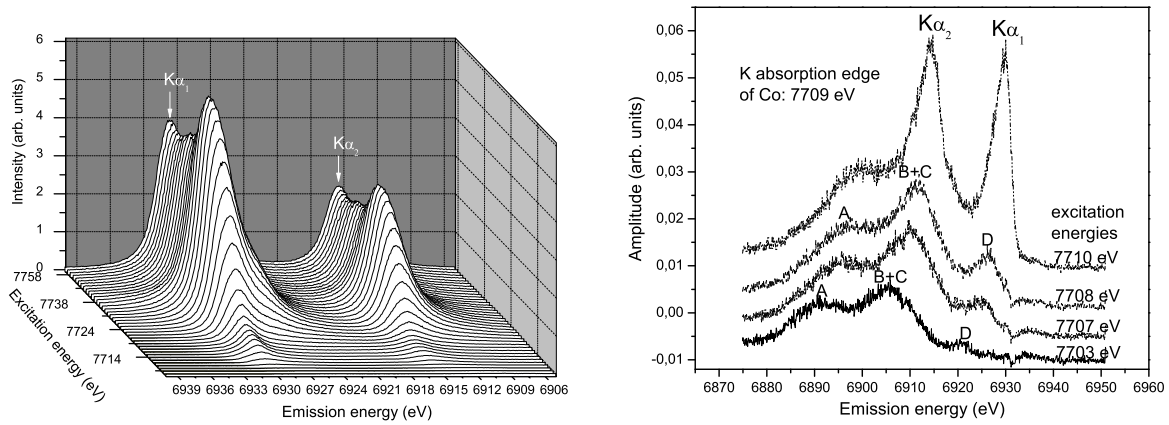

Figure 3.3: 3d Waterfall plot of the extended 1s2p RIXS plane of Co nanoparticles (left); line plots of Kα emission from Co nanoparticles measured below and above the absorption edge of Co (right).

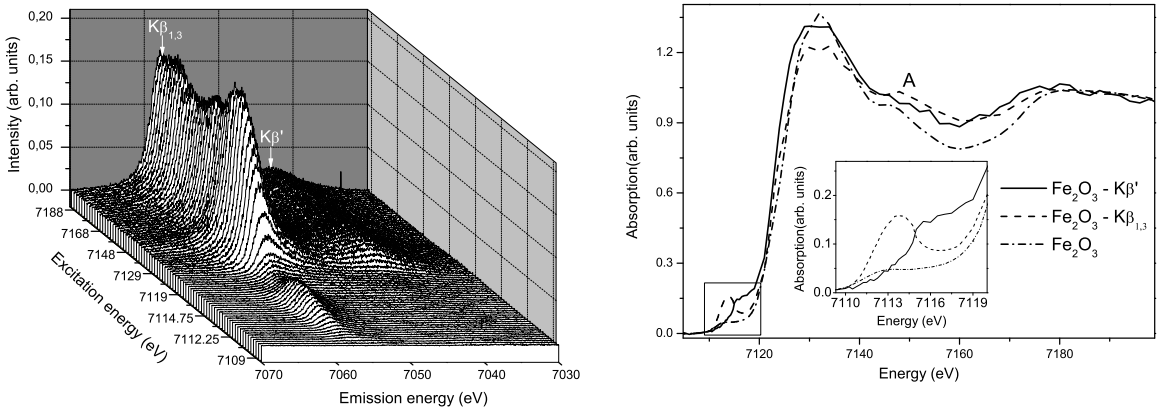

Figure 3.4: 3d Waterfall plot of the extended 1s3p RIXS plane of Fe_2O_3 (left); Fe K-edge XANES spectra of Fe_2O_3 measured in transmission mode (Fe_2O_3) and obtained by integrating the RIXS plane ± 0.5 eV around the K$\beta_{1,3}$ (Fe_2O_3 - K$\beta_{1,3}$) or Kβ' (Fe_2O_3 - Kβ') emission lines (right).

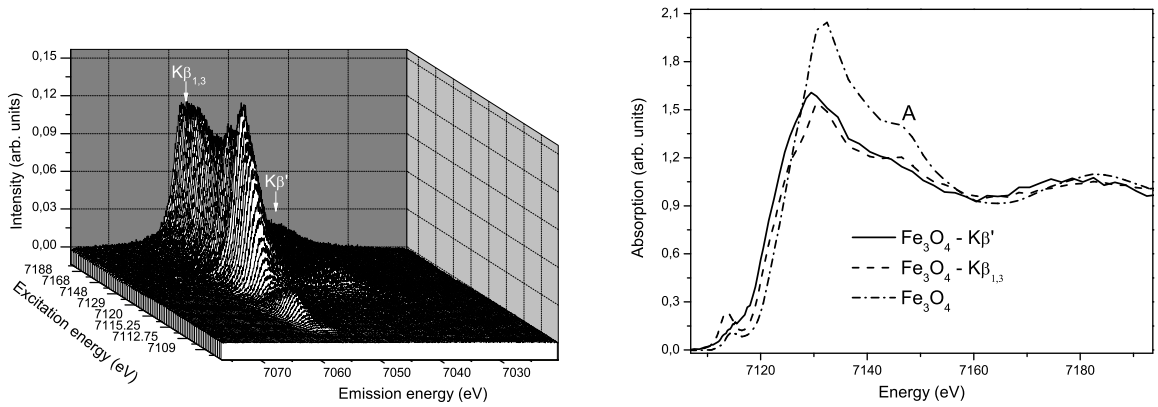

Figure 3.5: 3d Waterfall plot of the extended 1s3p RIXS plane of Fe_3O_4 (left); Fe K-edge XANES spectra of Fe_3O_4 measured in transmission mode (Fe_3O_4) and obtained by integrating the RIXS plane ± 0.5 eV around the K$\beta_{1,3}$ (Fe_3O_4 - K$\beta_{1,3}$) or Kβ' (Fe_3O_4 - Kβ') emission lines (right).

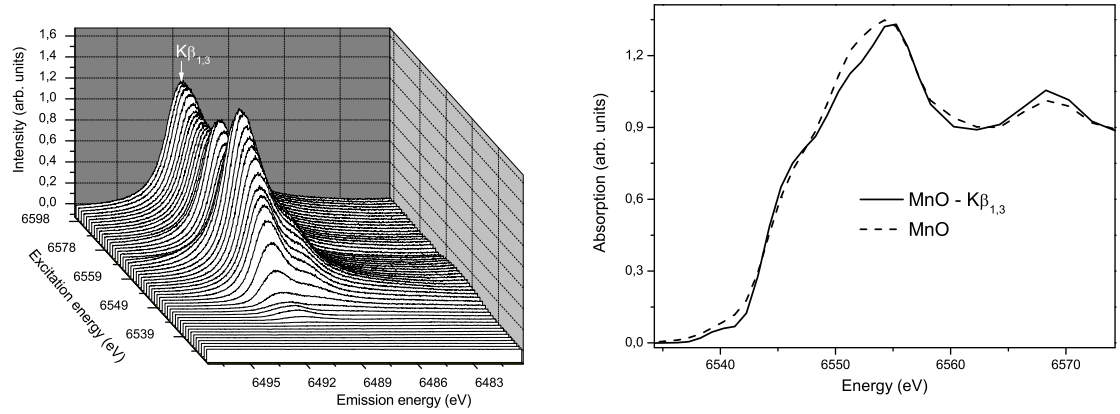

Figure 3.6: 3d Waterfall plot of the extended 1s3p RIXS plane of MnO (left); Mn K-edge XANES spectra of MnO measured in fluorescence mode (MnO) and obtained by integrating the RIXS plane ± 0.5 eV around the K$\beta_{1,3}$ (MnO - K$\beta_{1,3}$) emission line (right).

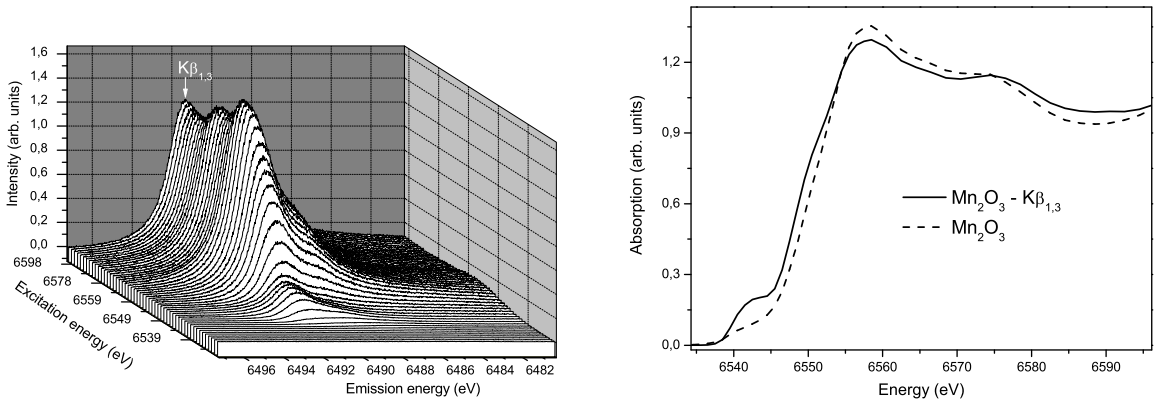

Figure 3.7: 3d Waterfall plot of the extended 1s3p RIXS plane of Mn_2O_3 (left); Mn K-edge XANES spectra of Mn_2O_3 measured in fluorescence mode (Mn_2O_3) and obtained by integrating the RIXS plane ± 0.5 eV around the K$\beta_{1,3}$ (Mn_2O_3 - K$\beta_{1,3}$) emission line (right).

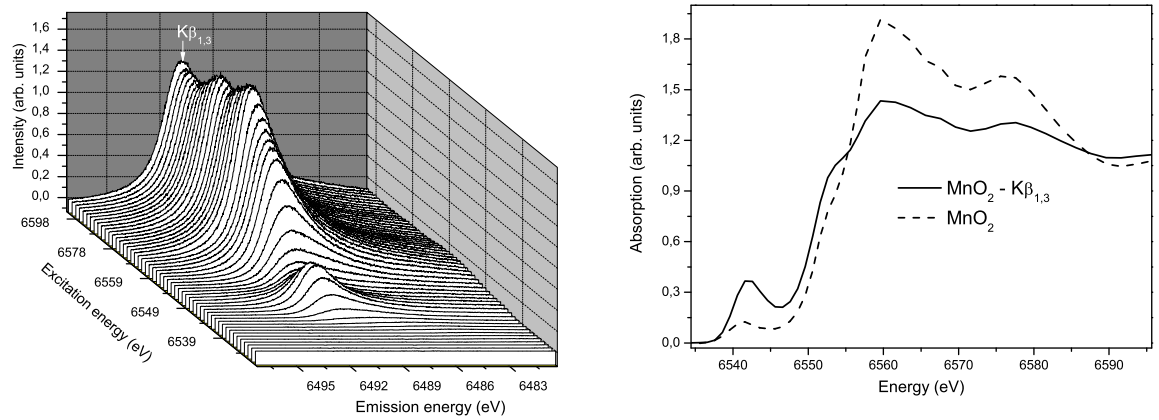

Figure 3.8: 3d Waterfall plot of the extended 1s3p RIXS plane of MnO_2 (left); Mn K-edge XANES spectra of MnO_2 measured in fluorescence mode (MnO_2) and obtained by integrating the RIXS plane ± 0.5 eV around the K$\beta_{1,3}$ (MnO_2 - K$\beta_{1,3}$) emission line (right).

Chapter 4

The experiments

4.1 ANKA and DORIS III

The major part of the XAFS measurements are done at the Ångtromquelle Kalrsruhe (ANKA), the 2.5 GeV synchrotron radiation facility located in Forschungszentrum Karlsruhe (FZK) (see Fig. 4.1). The INE-Beamline, located at a bending magnet port, was employed for the experiments (see Fig. 4.1). The High Resolution X-ray Emission (HRXE) measurements in Chapter 3 and some of the measurements in Sections 6.2.4 and 6.3.4 were done at the DORIS III, 4.45 GeV synchrotron radiation facility located in HASYLAB, Hamburg. The W1 beamline used is a wiggler type beamline. The most important parameters of the two synchrotrons are summarized in Figures 4.2 and 4.4. The spectral brilliance of ANKA is given in Figure 4.3. Figure 4.5 shows the spectral angular flux of DORIS III. More information about the characteristics of synchrotron radiation induced by bending magnets or insertion devices (wiggler or undulator) can be found in [104]. Test measurements at the K absorption of Mg (1303 eV) were done at the Center of Advanced Macrostructure and Devices (CAMD), 1.5 GeV synchrotron radiation facility located in Baton Rouge, USA. For more information see [2].

4.2 The INE-Beamline

The INE-Beamline has been built and is operated by the Institute for Nuclear Waste Disposal (Institut für Nukleare Entsorgung) [45] in collaboration with the Bonn Syli group. The beamline is primarily dedicated to actinide research with the possibility to perform XAFS studies on radioactive samples with activity up to 10^6 times the limit of exemption.

A schematic outline of the INE-Beamline is presented in Figure 4.6. The beamline is divided into two sections: an "optical" hutch and an experimental hutch. The photon beam entering the optical hutch is collimated by a system of aperture and slits; thereafter it is vertically collimated by the first cylindrically bent mirror. The beam passes through a Be-window, separating sections of different vacuum conditions, and enters the Double Crystal Monochromator (DCM). The monochromatized beam is focused horizontally and vertically to 600 μm x 350 μm by a second toroidal mirror and finally enters the experimental hutch.

The Rh coated silicon mirrors (collimating and focusing) define the upper energy limit of the beamline, as their reflectivity abruptly decreases (80%) at the K absorption edge of Rh (23220 eV).

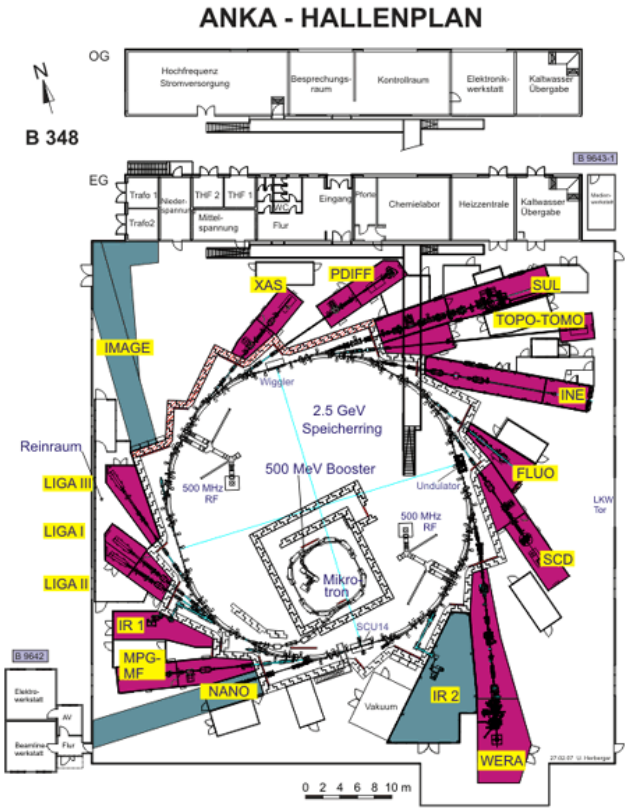

Figure 4.1: Beamlines at ANKA, status 2007. (from [1])

Parameter	Unit		
Circumference	m	110.4	
Number of long straight sections		4	
Photon critical energy	keV	6.0	
Injection energy	GeV	0.5	
End energy	GeV	2.5	
Operating electron beam current	mA	200	
RF-frequency	MHz	500	
Relative energy spread		9×10^{-4}	
Momentum compaction factor		0.01	
Horizontal emittance	nmrad	50	
Horizontal working point		6.73	
Vertical working point		2.69	
Horizontal beta-function, min-max	m	0.8 – 15	
Vertical beta-function, min-max	m	2 – 21	
Horizontal dispersion, max	m	0.7	
Port 5°, hor. beam size, divergence	mm/mrad (rms)	0.3	0.19
Port 5°, vert. beam size, divergence	mm/mrad (rms)	0.1	0.01
Port 11.25°, hor. beam size, divergence	mm/mrad (rms)	0.2	0.24
Port 11.25°, vert. beam size, divergence	mm/mrad (rms)	0.1	0.01
Straight section, hor. beam size, divergence	mm/mrad (rms)	0.9	0.06
Straight section, vert. beam size, divergence	mm/mrad (rms)	0.1	0.01
Dipole magnets			
Number		16	
Deflection angle	degrees	22.5	
Field strength	T	1.5	
Deflection radius	m	5.559	

Figure 4.2: Main Parameters of ANKA at 2.5 GeV. (from [1])

The reflectivity decreases with about 18 % at the LIII edge of Rh (3004 eV). The lower energy limit is determined mainly by the Be window with 50 μm thickness, which absorbs 30% of the

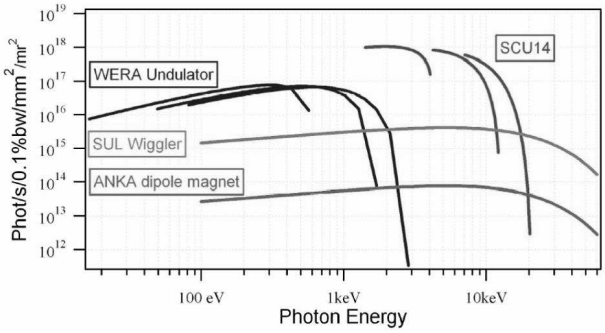

Figure 4.3: Brilliance of ANKA insertion devices in comparison with ANKA dipole magnet. (from [1])

Positron energy:	**4.45 GeV**
Initial positron beam current (5 bunches):	**140 mA**
Circumference:	**289.2 m**
Number of buckets:	**482**
Number of bunches:	**1 (for tests), 2 and 5**
Bunch separation (minimum):	**964 nsec (for tests), 480 nsec and 192 nsec**
Horizontal positron beam emittance:	**410 pi nmrad**
Coupling factor:	**3%**
Vertical positron beam emittance:	**12 pi nmrad**
Positron beam energy spread (rms)	**0.11%**
Curvature radius of bending magnets:	**12.181 m**
Magnetic field of bending magnets:	**1.2182 T**
Critical photon energy from bending magnets:	**16.04 keV**

Figure 4.4: Main parameters of DORIS III at 4.45 GeV. (from [3])

photons at 2500 eV. Successful measurements at the K-edge of phosphorus (2145) have already been performed.

4.2.1 The measuring modes and the experimental set-up

Three measuring modes are feasible for recording a XAFS spectrum, i.e., transmission, fluorescence and Total Electron Yield (TEY).

In transmission mode, Beer's law (2.1) is employed directly, i.e., the intensity of the primary and transmitted beams are monitored, while scanning the energy of the monochromotized beam through the desired absorption edge. In this case, the detectors are ionization chambers (Poikat, HASYLAB design), which are filled with gas, e.g., argon for Cu, Nb and Mo and nitrogen for Mn and Fe at ambient pressure. The beam ionizes the gas in the ionization chambers and the ions and electrons are collected on the condenser plates. The measured current is directly proportional to the number of photons. The current is converted to voltage through the relation:

$$V = \frac{eE_{ph}NG}{E_{eff}}, \tag{4.1}$$

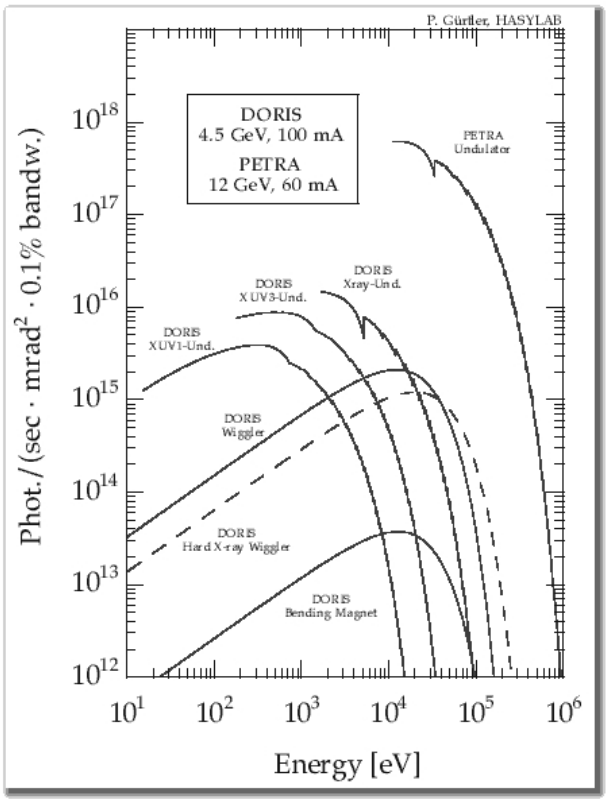

Figure 4.5: Spectral angular flux of insertion devices at DESY. (from [3])

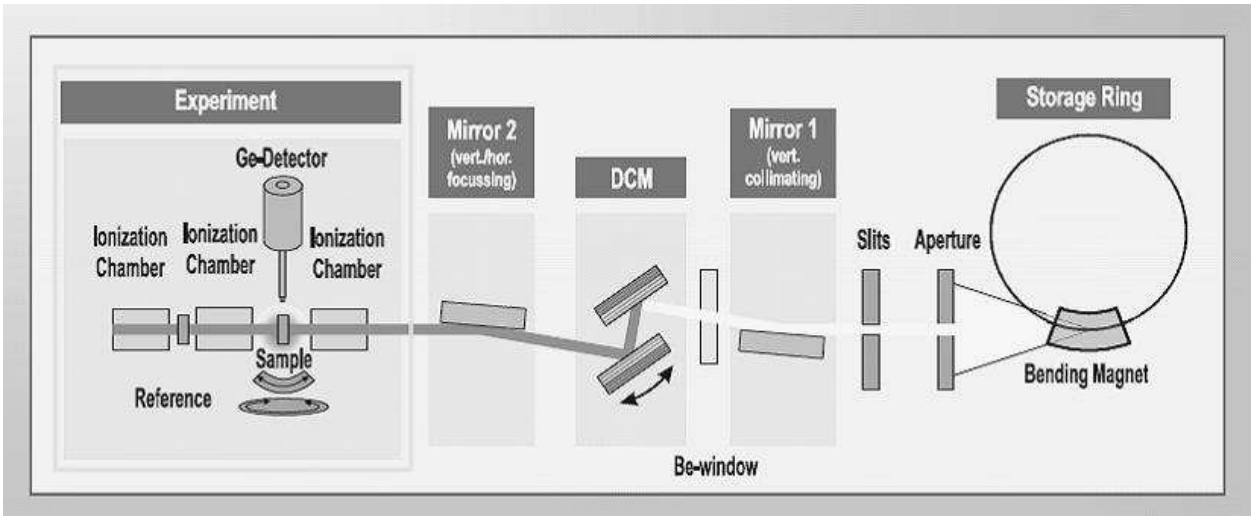

Figure 4.6: A schematic view of the INE-Beamline. (done by U. Herberger)

where E_{pn} is the energy of the incident photons, N is the number of photons per second impinging on the sample ($\approx 3.5{\times}10^{11}$ photons/sec at Zr K / Pu LIII edges using Ge (422) crystals). G is the

amplifier gain of the current-to-voltage converter and E_{eff} is the effective ionization energy of the gas (for nobel gases $E_{eff} \approx 30$) [178].

A third ionization chamber is used to measure a reference sample (usually a metal foil) simultaneously in order to assure correct energy calibration of the DCM during the experiment. The measurements are performed in air. The sample is mounted on a goniometer (HUBER type), which enables recording "thickness profiles", i.e., beam intensity vs beam's position on the sample, for monitoring the thickness of the sample and choosing a spot with homogeneous thickness. At the LIII absorption edge of Nb the ionization chambers of Bonn University optimized for low energy measurements are employed.

In fluoresces mode, usually the K_α emission line is recorded and its intensity (I_{fluo}) is normalized by the intensity of the primary beam (I_0), whose energy is scanned through the chosen absorption edge:

$$\mu \approx \frac{I_{fluo}}{I_0} \tag{4.2}$$

A five pixel high purity germanium solid state fluorescence detector (Canberra Ultra-LEGe type), cooled to liquid nitrogen temperature, is employed in this measuring mode. The detector is positioned under 90° and the sample mounted under 45°, with respect to the primary beam, in order to minimize the contribution of elastically scattered photons to the signal. After allocation of the K_α emission line, it is isolated by an electronic filter which filters out the contributions from scattered photons (elastically scattered photons and inelastically scattered photons: Compton peak) and other characteristic emission lines.

In TEY mode, a TEY chamber, design of Uni Bonn, was used. A metal plate is mounted over the sample, which is positioned under 45° with respect to the beam towards the metal plat. The emitted electrons are collected by the metal plate, which is connected to an electrometer (Femto type). The recorded current is proportional to the number of detected electrons. The signal is normalized by the intensity of the primary beam, which is monitored with an ionization chamber. The measurements were performed in low vacuum (continuous pumping of the chamber) or in helium (atmospheric pressure). No difference in the quality of the spectra was found. Since TEY is a more surface sensitive technique, the measurements at the LIII edge of Nb were repeated in transmission mode. The measured spectra were identical, therefore the spectra recorded in transmission mode are shown in this thesis.

The data acquisition set-up consists of Femto types of electrometers, whose output voltage is converted to frequency by voltage-to-frequency converters and finally the signal is counted by counter cards, which are connected through an optical wire to the data acquisition (daq) computer. SPEC daq software [171] is used for recording and visualizing the measurements.

Test measurements at the K-absorption edge of Mg were performed in TEY and transmission modes at the DCM beamline at CAMD. This beamline is located at a bending magnet. A differential-ion pump is installed before the DCM at the beamline maintaining different vacuum conditions. The use of a Be window is avoided, which provides the opportunity for low energy measurements. In order to minimize the absorption a Polypropylene window with 3 μm thickness and 12 mm diameter was used at the end of the beamline. The DCM (see Fig. 4.8) was equipped with a pair of Beryll (10-10) crystals. MgO XANES spectra were successfully measured in transmission mode. One of the spectra measured with 1eV energy step width and 1s integration time is shown in Figure 4.7. The ionization chambers, design of Uni Bonn, were filled with air, 7 mBar pressure. The sample

was prepared by spreading MgO powder over a piece of 3 μm thick Polypropylene foil. The powder was removed by shaking out the foil. As a result, an almost invisible layer of MgO was left on the foil. Signal from the actual samples was not detected, because of the low concentration of Mg (7 wt%) doped in the heavy matrix of LN.

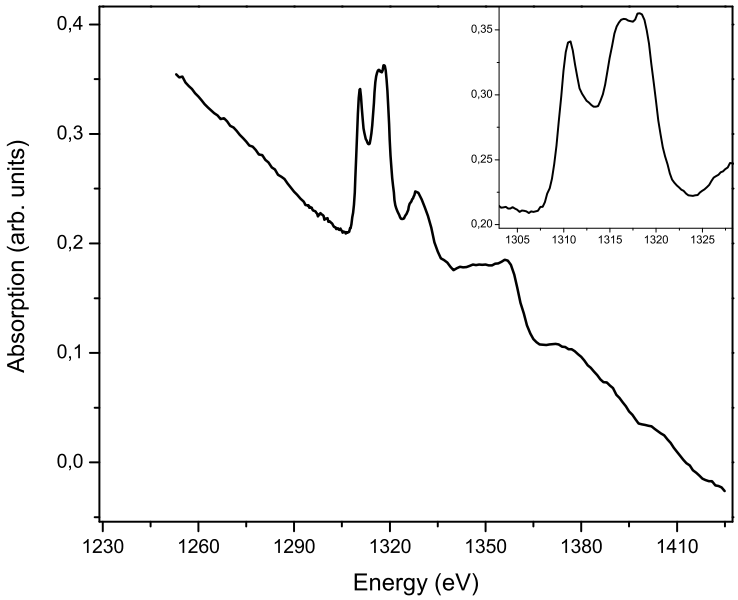

Figure 4.7: A Mg K-edge XANES spectrum of MgO.

4.2.2 The Double Crystal Monochromator (DCM)

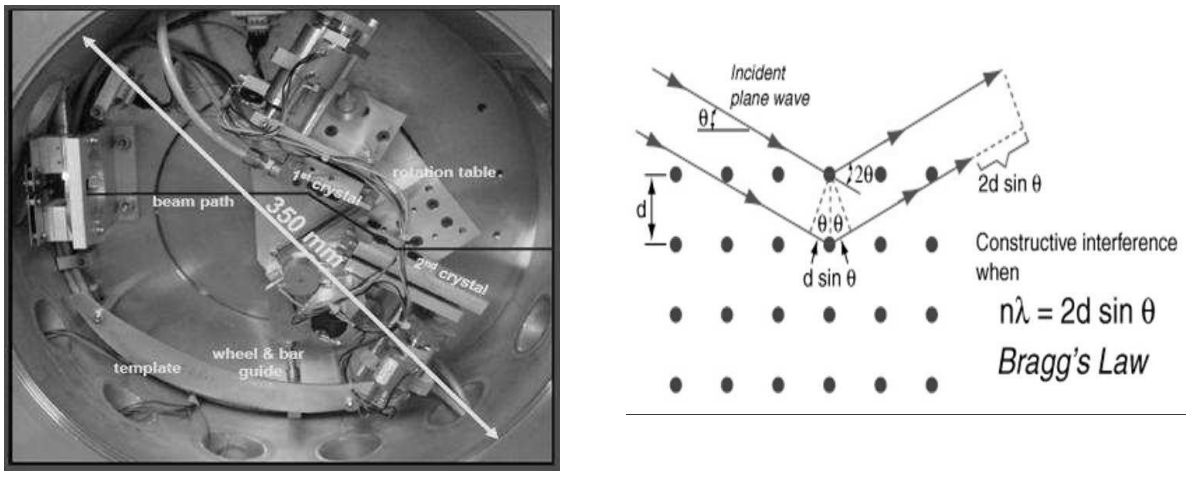

Figure 4.8: The DCM (left) and an illustration of the Bragg's law (right) (from Wikipedia).

The monochromator at the INE-Beamline is provided by Bonn University. It is a Lemonnier type DCM with a fixed exit beam (see Fig. 4.8 left). Fixed exit means that the horizontal and vertical

Crystal	Interplanar spacing (Å)	Energy range (eV)
Si(111)	3.1351	2190 - 7650
Ge(422)	1.1520	5938 - 20794

Table 4.1: Characteristics of the crystals used in this thesis.

.

positions of the monochromatic beam remain unchanged when the energy is scanned. The fixed exit design is achieved by a curved metal support (cam) (see Fig. 4.8 left), which keeps the distance between the first and the second crystal constant with the help of a bar guide ending with a wheel. This feature allows a stationary experimental set-up and a probe of the sample at the same sample spot, which limits the influence of thickness effects on the measured spectrum. The two crystal holders are mounted on a rotation stage, which is rotated by a Newport stepping motor (RV120HAHL type) with minimum step size of 0.0001°. The cam restricts the usable angle range from 15° to 65°.

The white beam is monochromatized by reflection from the first crystal. The process is described by Bragg's law:

$$n\lambda = 2d\ \sin\theta \tag{4.3}$$

or

$$E_n = \frac{hc}{2d \sin\theta}. \tag{4.4}$$

where d is the interplanar spacing of the crystal, θ is the incident angle (see Fig. 4.8 right) and E/λ is the energy/wavelength of the diffracted photons and n is the order of reflection. The d spacing of a crystal depends on the type of the crystal and the orientation of the plane of its cut, which is denoted by the Miller's indexes, e.g., Si(111). The crystals used in this thesis are given in Table 4.1. The first order of reflection is preferred, i.e., $n = 1$, because the diffracted photon flux has the highest intensity. However, the Bragg condition is also satisfied for photons with higher energies, e.g., for measurements with Si(111) at 2371 eV (the LIII-edge of Nb) photons with an energy around 7000 eV will be diffracted as well, i.e., $n = 3$. This higher harmonic can distort the spectrum as they are detected by the second ionization chamber without being absorbed by the sample. The angular distribution of the reflectivity of a crystal differs for different n (see, e.g, [121]), therefore it is possible to avoid contributions from high energy photons by detuning the angular position of the second crystal from the exact Bragg angle. However, this approach lowers the intensity of the beam and the energy resolution. At the INE-Beamline, the second crystal is equipped with a piezo feedback system, which fine tunes the angular position of the crystal to a selectable level from the maximum beam intensity. Therefore, the piezo is synchronized with the intensity of the signal in the first ionization chamber. This set-up compensates for the decreasing current in the ring, i.e., decreasing intensity of the primary beam, and allows for systematic studies on higher harmonics on the spectrum. The two crystals are mounted on copper holders. The heat load is reduced by a water cooling system installed on the first crystal.

The choice of the crystal usually determines the experimental resolution.

$$\delta E = E \cot\theta \delta\theta \tag{4.5}$$

$$\delta\theta = \sqrt{\psi_v^2 + \frac{1}{2}\delta\alpha^2}, \tag{4.6}$$

where ψ_v describes the vertical divergence of the beam and $\delta\alpha$ is the width of the rocking curve. From equation 4.5 we see that for optimal energy resolution θ should be as large as possible and the crystal should have a narrow reflectivity profile. A concurrent contribution to the resolution of the measured spectrum is the core-hole life time broadening, which is caused by the finite life time of the core hole leading to a Lorentzian type of broadening. For example, the core-hole lifetime broadening for a deep core level as the K-edge of Fe is 1.15 eV [183].

The procedure for setting-up the INE beamline for measurements of XAFS spectra is as follows: first, the chosen crystal pair is mounted in the monochromator. Second, the beam focus by the focusing (second) mirror is optimized. The INE-Beamline has a CCD camera, which is has been used for this purpose. Third, the ionization chambers are filled with gas. Fourth, the monochromator is calibrated by measuring a XANES spectrum from a reference metal foil and setting the maximum of the first peak of the derivative of the XANES spectrum to the energy of the absorption edge of the element of interest. For fluorescence measurements the filters to select the desired emission line have to be set.

Additional experimental information is given in the respective sections of the studied samples.

4.2.3 The samples

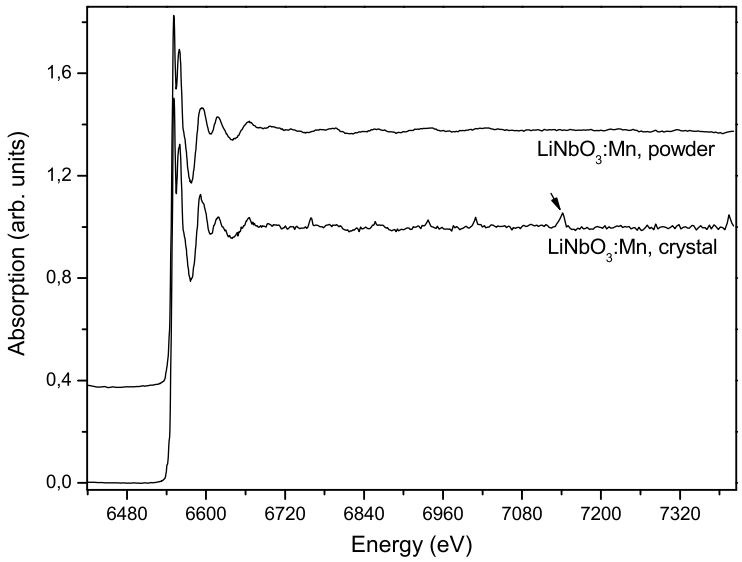

Figure 4.9: Nb K-edge XAFS spectra of $LiNbO_3$:Mn measured as a single crystal and as a powder sample.

Most of the reference samples in this thesis are measured in transmission mode. This is the preferred measuring mode for concentrated samples, which can be prepared with a defined thickness. The practice has shown that the optimum sample's thickness, leading to a low signal-to-noise ration, is that yielding an "edge jump" of $\leqq 1$. Homogeneous samples, sample with small grain size and

samples free from holes and spots with various thicknesses are required for high quality spectra. More information on the topic of sample homogeneity can be found in [177] and [176].

Because of the low amounts of the transition metals doped in the LN crystals, the XAFS measurements were performed in fluorescence mode. However, the significant amount of diffracted photons led to severe distortions (see Fig. 4.9) of the spectra. The problem was solved by grinding the crystals to fine powder and rotating the powder sample by 0.001°, with respect to the primary beam, after each spectrum, so that any contributing small diffraction peaks cancel out after averaging the spectra.

4.3 The W1 beamline

A High Resolution X-ray Fluorescence (HRXF) spectrometer is installed at the W1 beamline [196], which is able to reduce the energy resolution of measured fluorescence lines to ~ 1 eV (FWHM) for Cu K_α and 4.9 eV for Cu $K\beta_{1,3}$ compared to ~ 150 eV resolution of a conventional fluorescence detector (e.g., the Canberra type used at the INE-Beamline). This tremendously improved energy resolution provides an opportunity for obtaining chemical and structural information, which is often not possible to extract from conventionally measured XAFS or X-ray emission spectra (see Section 6.3.4).

A principle scheme of the spectrometer is shown in Figure 4.10 left. An analyzer crystal, a CCD chip (Roper Scientific/Princeton Instruments type) and a sample holder (see Fig. 4.10 right) are set in a vacuum tank on a Rowland circle with diameter equal to the radius of the curvature of the spherically bent analyzer crystal, i.e., 1000 mm. In this geometry, the emitted photons from the sample are diffracted and focused by the analyzer crystal onto the detector, where the energy range of the recorded emission spectrum depends on the source size and the width of the CCD camera. More information about the spectrometer can be found in [196].

The geometry of this set-up is the so called wavelength dispersive geometry. If no position sensitive detector is available, a $\theta/2\theta$ scanning geometry is applied (see, e.g., [64]).

Important parameters influencing the experimental energy resolution are the diameter of the Rowland circle, the size of the source, the quality of the crystal (free of defects), as well as the width of its reflectivity curve (see equations 4.5 and 4.6); the value of θ (see equation 4.5). This explains the choice of backscattering geometry. For more information on the topic see, e.g., [196].

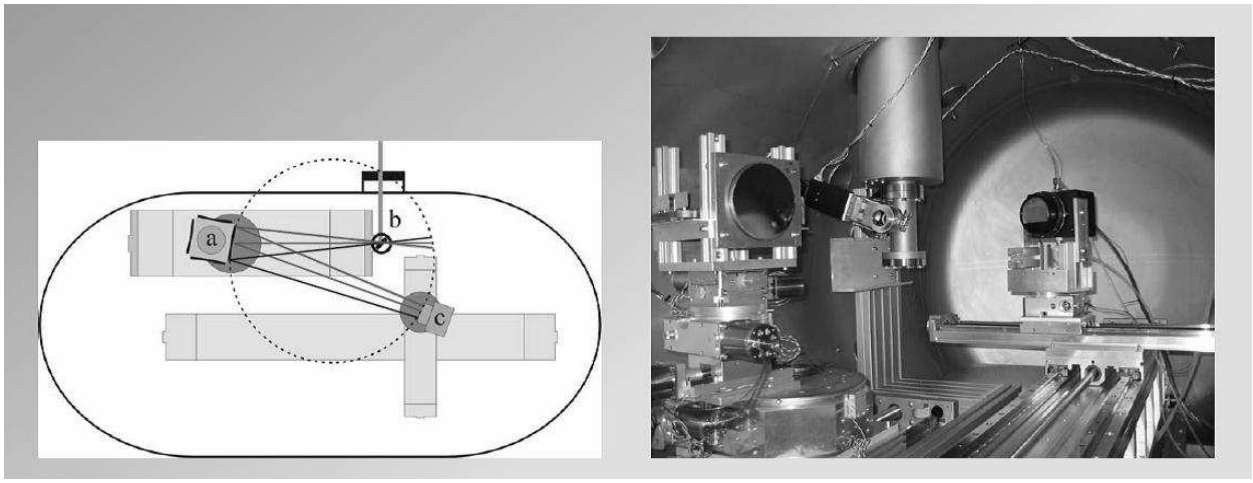

Figure 4.10: A schematic view (left) and photograph (right) of the HRXE spectrometer at the W1 beamline. (from [196])

Chapter 5

Lithium niobate

The electro-optic, photorefractive, and ferroelectric properties, as well as the robustness and uncomplicated fabrication of Lithium Niobate (LN, $LiNbO_3$), have been drawing the interest of research and industry for several decades. Improved optical properties of the LN crystals are achieved, for example, by doping them with transition metals such as Cu, Mn and Fe or by irradiating them with high energy ions. In this chapter, a brief overview on the growth, structure, intrinsic defects and optical absorption of the LN crystals will be given. The Nb K and LIII-edge XAFS spectra of $LiNbO_3$ will be discussed as well.

5.1 Growth, defects and structure of the lithium niobate crystals

The congruently-melting LN is pulled in a single crystal (Boules) employing the Chochralski method (see Fig. 5.1 left). The Li_2O composition is 48.4 mol% in the melt, leading to a Lithium-to-Niob-ratio < 1, i.e., Li/Nb=0.942 [163]. Despite the commonly used stoichiometric chemical formula $LiNbO_3$, precise diffraction analyses have shown that the correct formula of a congruently-melting LN crystal is $[Li_{1-5x}Nb_{5x}]Nb_{1-4x}O_3$, where x=0.0119 [5]. One type of intrinsic defect in the non-stoichiometric LN crystals are the 5.9% missing Li atoms [163]. The free Li positions in the LN matrix are filled by Nb atoms, called antisite defects (Nb_{Li}), with respective Nb vacancies on the Nb sites (V_{Nb}), thereby maintaining charge neutrality in the crystal (Li, Nb and O have 1+, 5+ and 2- oxidation states respectively). The congruently-melting LN crystals are used in this work as they are usually doped by metal atoms. Details on the doping techniques of the copper-doped, manganese-doped and iron-doped LN crystals (LN:Cu, LN:Mn and LN:Fe) will be given in the sixth chapter.

The LN belongs to the $3m$ point group with one symmetry axis usually denoted with c. At room temperature LN is spontaneously polarized along this axis in its ferroelectric phase. The structure of LN consists of hexagonal close packed oxide ions, where two thirds of the face sharing octahedral sites are occupied by cations, i.e., Li or Nb atoms, and one third is empty. Due to electrostatic repulsions in its ferroelectric phase, the Li and Nb atoms are not in the middle of the octahedrons, but are shifted in opposite directions along the z axis (see Fig. 5.1 right) [195]. LN is birefringent with one anisotropy axis, i.e., the c axis.

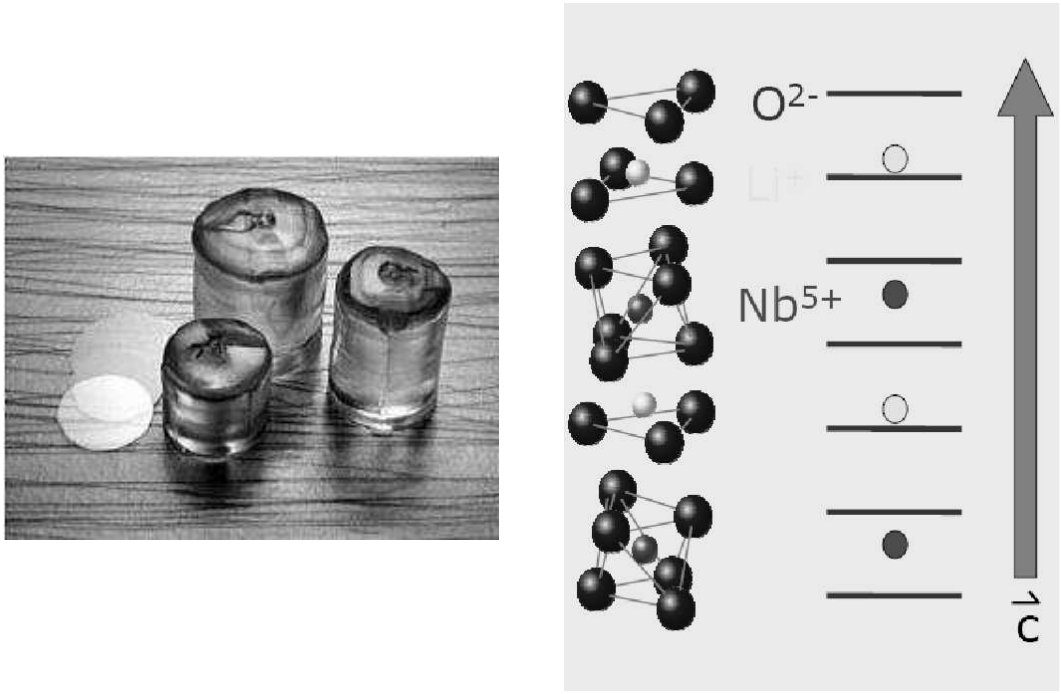

Figure 5.1: 3 and 4 inches $LiNbO_3$ Boules and wafers grown by the Chochralski method (left). A schematic view of the structure of LN along the c axis (right).

5.2 Absorption spectra of lithium niobate from IR to hard X-ray regions

Lithium Niobate does not absorb in the near IR, visible and near UV regions until its fundamental absorption, which starts at around 319 nm (α = 319 nm) (see Fig. 5.2) [101]. The fundamental absorption is caused by transition of electrons from O to Nb [38, 99] and the absorption wavelength can change its position when the composition of LN is altered. Usually, water molecules are trapped in the LN crystals. The H atoms bind with O atoms forming OH^- groups, which can be excited with IR light resulting in a characteristic IR absorption band (see Fig. 5.2).

Nb has a Z number 41 and can be described as a 4d transition metal, as its ground-state valence-band configuration is $5s^14d^4$. The XANES spectra of LN measured at the Nb K (18986 eV) and L (2371 eV) edges are displayed in Figure 5.3 and 5.4. The resonance *A* at around 18994 eV in the Nb K-edge XANES spectrum is assigned to the transition of the 1s electron to the 4d state, which is forbidden in compounds with inversion symmetry due to the dipole selection rule. The noncentrosymmetric positions of the Nb and Li atoms in the oxygen octahedra lead to hybridization of the Nb 4d with the O 2p atomic orbitals, introducing p character to the d type molecular orbitals (9e, 7a1 and 11e; see Fig. 5.5) of $LiNbO_3$ [72]. This enhances the probability for this otherwise forbidden 1s→4d transition. The core-hole lifetime broadening of the K-edge of Nb is ≈3.9 eV [6], which exceeds the experimental resolution estimated as 1 eV. This intrinsic broadening prevents resolving the pre-edge A resonance, which appears as a single structure (see Figure 5.3). The 4d state is split by the trigonal crystal field into the energetically close 9e and 7a1 and 11e molecular orbitals but this splitting is not resolved (see Fig. 5.5 [72]).

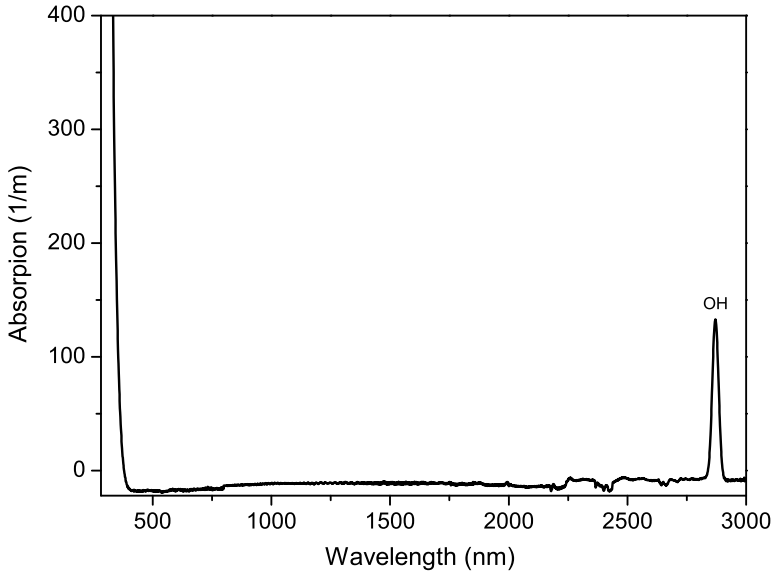

Figure 5.2: Absorption spectrum of undoped congruently-melting $LiNbO_3$ from near IR to near UV regions.

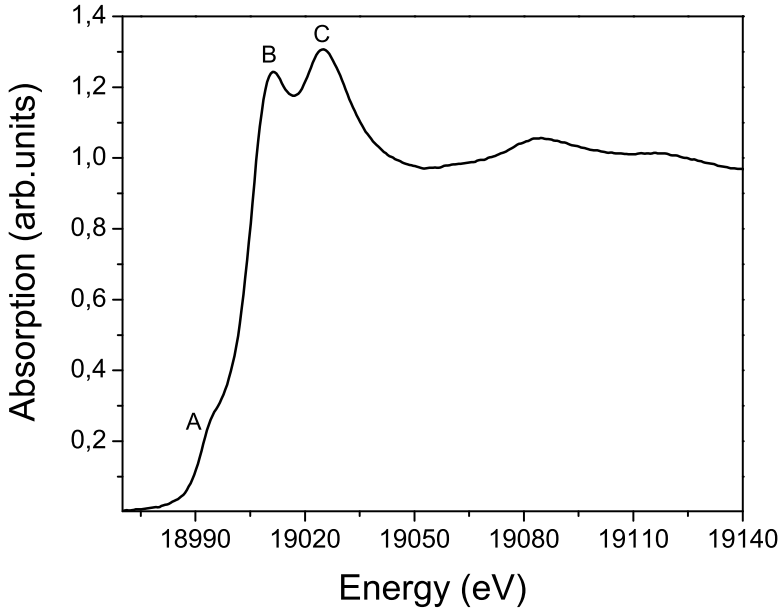

Figure 5.3: XANES spectrum of $LiNbO_3$ measured at the Nb K absorption edge.

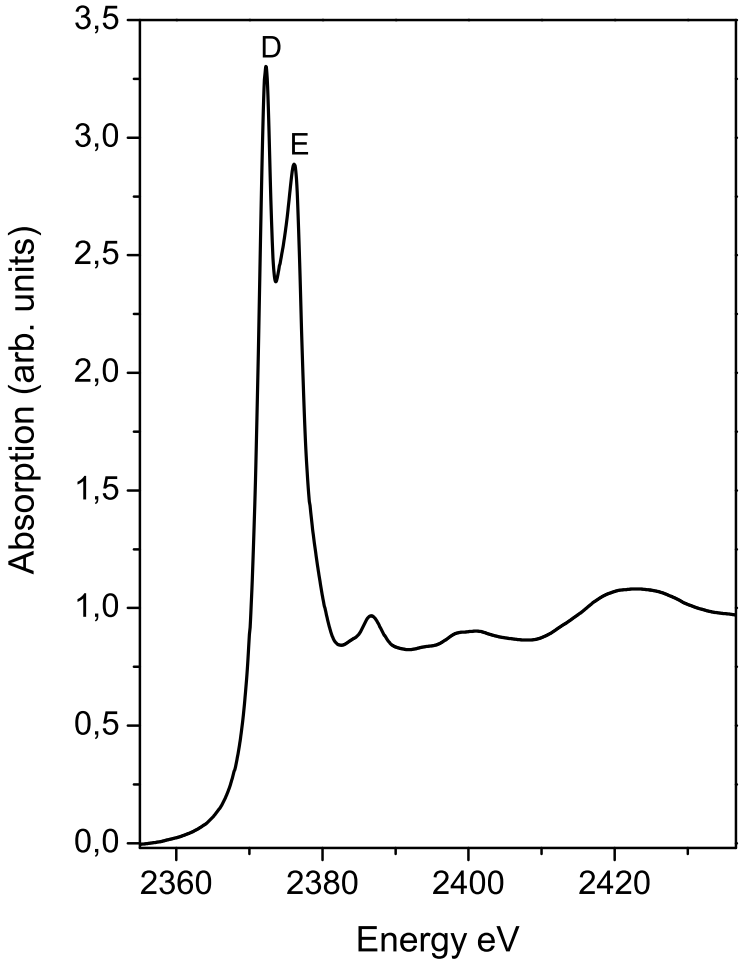

Figure 5.4: XANES spectrum of $LiNbO_3$ measured at the Nb LIII absorption edges.

The most intense double-featured resonance (white line) in the Nb LIII-XANES spectrum probes the 4d unoccupied states, because of the 2p→4d dipole allowed transition (see peaks D and E in Fig. 5.4). The splitting of the WL into two resonances represents transitions of the $2p_{3/2}$ electron to the 9e and 7a1 or 11e molecular orbitals. The direct observation of this molecular orbital splitting is possible, because of reduced core-hole lifetime broadening of the L-edge of Nb, which is estimated as ≈1.5 eV [138]. The white line of the K-edge XANES spectrum of Nb exhibits a similar splitting, which is due to splitting of the 5p state (see peaks B and C in Fig. 5.3). Shell-by-shell calculations with FEFF8.2 code of the Nb K-edge XANES spectrum are presented in Figure 5.6. The WL of the Nb K-edge XANES spectrum develops from a broad structure to two pronounced resonances after calculating the Nb K-edge XANES spectrum on a cluster of atoms large enough to include atoms from the third coordination shell. The core-hole lifetime broadening is taken into account in the calculations, which explains the very weak splitting of the pre-edge resonance *A*.

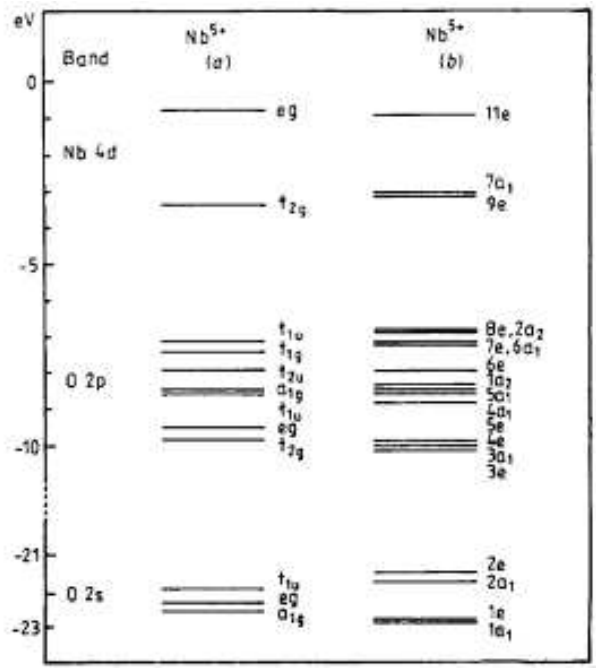

Figure 5.5: Energy level diagram for NbO_6^{-7} clusters. O_h symmetry (representative of $KNbO_3$) a), C_{3v} symmetry (representative of $LiNbO_3$) b) (from [72])

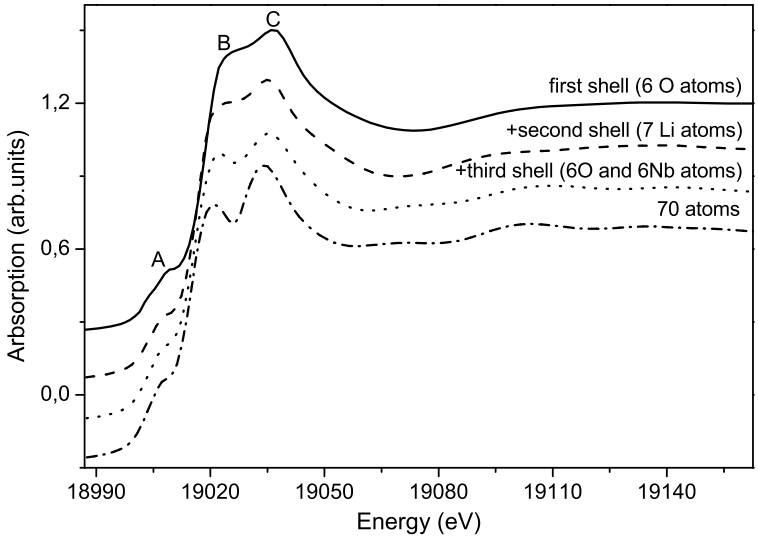

Figure 5.6: Shell-by-shell calculation of the Nb K-edge XANES spectrum of $LiNbO_3$. The structure of $LiNbO_3$ with ICSD 28294 was used as a model.

Chapter 6

Doped lithium niobate

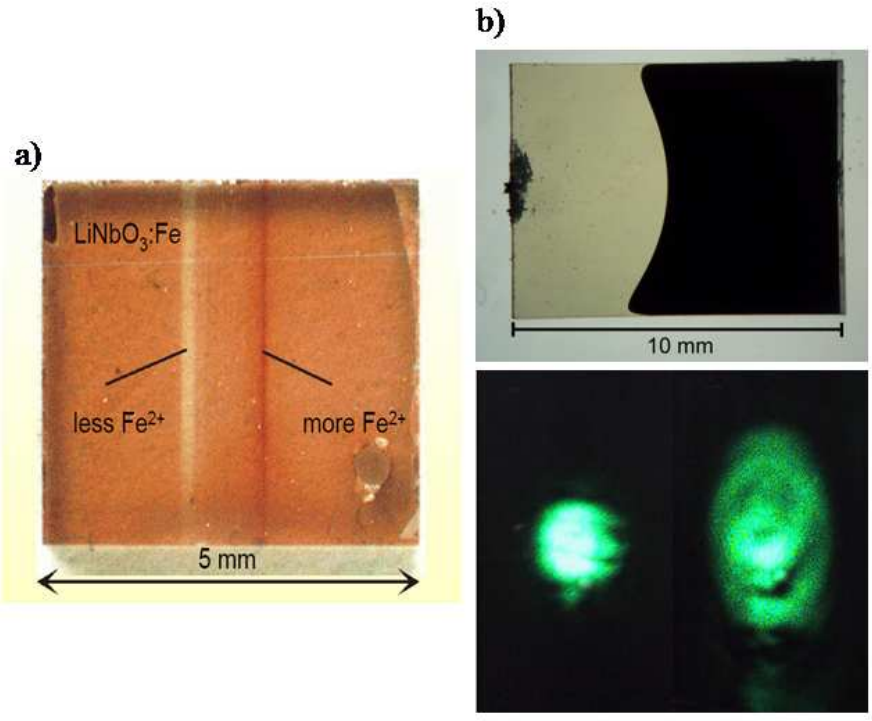

Figure 6.1: a) An iron-doped $LiNbO_3$ crystal has been illuminated for days with a light stripe. As a result, a region with deficit of Fe^{2+} (more Fe^{3+}) and saturated with Fe^{2+} (no Fe^{3+}) are formed (from [32]). b) An iron-doped $LiNbO_3$ has been half oxidized (the left side of the crystal) with thermo-electric oxidization method. The treatment avoids the "optical damage". This effect is demonstrated on the lower picture, where transmission of a focused green laser (532 nm wavelength) is shown. The light is confined on the left side and scattered on the right side of the crystal.

6.1 Copper-doped lithium niobate

6.1.1 Introduction

It has been shown that highly concentrated copper doping in LN crystals causes a refractive index change (Δn) comparable to less concentrated iron doping in LN crystals [141]. However, copper doped crystals can be prepared by a cheaper and easier diffusion process [86, 140], as the diffusion constant of copper exceeds that of iron by a factor of 500 [86, 98]. An increase in Δn, the key factor in enhancing the storage capacity of a hologram [141], is achieved by raising the content of Cu^{2+} traps in a LN crystal. However, at a high level of Cu^{2+} a decrease of Δn is observed [141]. In order to tune the photorefractive properties of the doped crystals, a detailed knowledge of the average valency of the copper atoms, as well as their local structure, e.g., site of occupation, is desirable. The majority of the published studies on copper atoms incorporated into a LN matrix (prepared by a solid-state reaction [120] or an ion exchange method [34]) support the hypothesis that the doped Cu atoms dominantly occupy Li sites [34, 120]. However, detailed study on electronic and geometrical structure upon systematic change in copper valence and concentration (0.1-0.7 wt% of Cu) is not yet available.

The goals of the following investigation on copper-doped LN crystals are: (i) to define the average formal oxidation state of Cu in indiffused, reduced and oxidized LN crystals with different (0.1-0.7 wt% of Cu) doping levels of copper atoms, (ii) to identify not only the major site of incorporation (Li or Nb site) of the Cu atoms in all crystals, but also the structural differences between the Cu^{1+} and Cu^{2+} sites in the indiffused and reduced LN crystals, and finally, (iii) to provide evidence for the charge compensation mechanisms during the reduction treatment.

6.1.2 Preparation of the samples

The $LiNbO_3$:Cu samples were prepared from commercially available *x*-cut wafer material (thickness 1 mm). The wafers were cut into pieces of 9×10 mm^2, where the 10 mm axis is parallel to the crystallographic c axis. After cutting, layers of copper were evaporated onto the surface in thicknesses ranging from 200 nm to 2000 nm. The samples were then annealed at 1000°C for 24 h in air to allow Cu to diffuse into the crystal volume[140]. The samples 200_1, 500_1 and 1000_1 were prepared in one single diffusion step. Sample 2000_1_a is first coated with 1000 nm Cu, annealed, coated for a second time, and subsequently annealed again. For comparison sample 2000_1 was prepared in one single step using a 2000 nm layer.

After the diffusion process, samples were either oxidized in O_2 atmosphere at 1000°C for 5 hours or reduced in vacuum about 10^{-3} mbar for 5 hours at 1000°C. Thereby the concentration ratio $c_{Cu^{2+}}/c_{Cu^{1+}}$ was changed. One sample, 3000_2_a, was diffused and reduced in a single step by annealing at 1000°C in vacuum for 24 hours. The 200, 500 and 1000 sample series were diffused and either reduced or oxidized at the same time.

The notation of all studied LN crystals and the XANES spectra are listed in Table 6.1. The three digit number in the notation indicates the thickness of the copper layer in nm, e.g., 200 nm. The numbers from 1 to 3 specify the presence or lack of subsequent treatment of the crystal: _1: indiffused, _2: reduced, _3: oxidized. The letter _a shows a two-step diffusion proccess for the 2000_1_a sample and simultaneous diffusion and reduction of the crystal for the 3000_2_a sample.

Notation of the samples and the spectra	Cu-layer thickness in nm	$c_{Cu^{1+}}$ (10^{24} m^{-3}) ±15%	$c_{Cu^{2+}}$ (10^{24} m^{-3}) ±15%	c_{Cu} (10^{24} m^{-3}/ wt%) ±15%
200_1	200	8	33	41/0.1
200_2	200	17	13	30/0.1
200_3	200	6	31	37/0.1
500_1	500	18	56	74/0.2
500_2	500	31	35	66/0.2
500_3	500	12	59	71/0.2
1000_1	1000	24	81	105/0.3
1000_2	1000	38	52	90/0.2
1000_3	1000	19	99	118/0.3
2000_1	2000	73	48	121/0.3
2000_1_a	2000	90	184	274/0.7
3000_2_a	3000	87	23	110/0.3

Table 6.1: The concentrations of Cu^{1+} and Cu^{2+} ($c_{Cu^{1+}}$ and $c_{Cu^{2+}}$) and the total Cu concentration determined by UV-VIS/IR absorption measurements (c_{Cu}).

.

6.1.3 Experiment, methods and data evaluation

XAS experiments were performed at the INE-Beamline at the ANKA 2.5 GeV synchrotron radiation facility, Karlsruhe, Germany. For details about the instrumentation at this beamline, see Ref. [45] and Section 4.2. A Lemonnier-type [111] double crystal monochromator equipped with a set of Ge(422) (Cu K-edge) or Si(111) (Nb LIII-edge) crystals was employed for energy monochromatization. For energy calibration of Cu K-edge spectra a photon energy of 8979 eV was set to the first inflection point of the K-edge spectrum of a copper foil, simultaneously measured with the samples and references. The Nb LIII-edge spectra were energy calibrated against the Sulfur K-edge WL (the first intense absorption resonance of the spectrum) of $ZnSO_4$ set to 2481.44 eV. The copper doped LN crystals were ground and absorption spectra of the powder samples were recorded at the Cu K-edge (8979 eV) in fluorescence mode and at the Nb LIII-edge (2371 eV) in transmission mode.

All Cu K-XANES spectra were measured in the energy interval from 8930 eV to 9130 eV, with 0.5 eV step width and 2s integration time. At the Nb LIII-edge, the XANES spectra were measured in the energy interval from 2324 to 2360 eV, with 0.1 eV step width and 2s integration time. At least five XAS (XANES + EXAFS) spectra were collected from each sample measured in fluorescence mode, in order to check for reproducibility of the spectral features and to improve the statistics. XANES data reduction consisted of subtraction of a linear background fit to the pre-edge region, from 8829 eV to 8959 eV for Cu K-edge spectra and from 2324 eV to 2360 eV for Nb LIII-edge spectra, followed by normalization of the spectra to an edge jump of one at 9121 eV (Cu) or 2439 eV (Nb).

The ARTEMIS [151] program package was used for EXAFS analyses. The XAFS signal [χ(k)] measured at the Cu K-edge, covering a k range from 2.3-10 Å^{-1}, was Fourier-transformed to R space using a k weighting of 1, 2 and 3 and a Hanning Window with window sills dk equal to 2. The ARTEMIS option for simultaneous fits with each three k weightings (1, 2 and 3) was used. The fit

was performed in R space over a range from 1-3.1 Å for the 200, 500 and 1000 sample series and 1-3.7 Å for 2000 and 3000 sample sets. For the initial model the structure of $LiNbO_3$ (ICSD 28294) was used. The amplitude reduction factor was held constant to 0.85 (S_0^2), the value obtained from initial fits for a Cu foil FT-EXAFS spectrum measured under the same experimental conditions. The error of the S_0^2 is estimated to be ± 0.04.

During fits of the FT-EXAFS spectra the E_0 and the Debye-Waller factors were varied. The first coordination shell (Cu-O) was first fit using a defined coordination number, according to the model, and varying the distance. The fit was repeated while fixing the distance and varying the coordination number to ascertain if this led to reduction of the coordination number. This was the case for the reduced crystals. Therefore, the distance and coordination number were consecutively fixed and varied until the best fit was obtained. In the next step the coordination number and distance for the first coordination shell were held constant at their best fit values and the fit range was extended to 3.1/3.7 Å. The fit procedure was repeated using first single scattering paths with the highest amplitude contribution, i.e., Cu-Nb, in this distance range. During the fit procedure, care was taken that the number of varying parameters was always half or less the number of independent data points *Nind* (see Section 2.3.1) For all performed fits, the obtained $\Re$ factor (overall goodness of fit) was 0.01 or smaller, which means that data and fit agree on average within 1% or better.

We attempted to simulate the Cu K-XANES spectra of the 3000_2_a and 200_1 samples using the FEFF8.2 code [154]. The purpose of the calculations was to check if it is possible to reproduce the Cu K-XANES spectra using the results from the EXAFS analyses as input. The calculations were done for a cluster of 230 atoms and no experimental broadening was taken into account. In the FEFF8.2 calculations the EXCHANGE, SCF, FMS and XANES cards were used. The Hedin-Lundqvist self-energy was chosen as exchange correlation potential, which is the default setting of the EXCHANGE card. We did the calculations using a modified structural model with Cu incorporated into the Li site in two ways, either by substituting only the absorbing Li atom by a Cu atom or by substituting 100% of the Li atoms by Cu atoms. As the obtained spectra are very similar, only the first calculations (substitution of the absorbing Li atom by a Cu atom) are shown below. The atomic cluster employed in the calculation was modified, in order to approximately reflect the distances and coordination numbers obtained from the EXAFS analysis.

The modifications for simulating the 200_1 and 3000_2_a spectra are as follows: (1) To simulate the 200_1 experimental spectrum O and Li atoms were initially moved −0.2 Å (if the *z* coordinate is positive) or +0.2 Å (if the *z* coordinate is negative) along the *z* axis; the Li atoms and the absorbing Cu atom with *z* coordinates equal to zero were not moved. For a second simulation step Nb atoms were shifted +0.1 Å (if the *x* coordinate is positive) or −0.1 Å (if the *x* coordinate is negative) along the *x* axis. The cluster was then modified by shifting the central absorbing Cu atom +0.16 Å along the *z* axis, the three O atoms from the first shell with negative *z* coordinates +0.5 Å along the *z* axis and the remaining three first shell O atoms −0.05 Å along the z axis. In a final step, the coordinates of the four Nb atoms closest to the absorbing Cu atom were refined in the simulation until close agreement with the Cu-Nb1 and Cu-Nb2 distances obtained from the EXAFS analysis was achieved; (2) The modifications of the atomic cluster used for simulation of the 3000_2_a spectrum included removing three O atoms with positive *z* coordinates and one O atom with negative *z* coordinate from the first coordination shell from the list of atomic cluster coordinates. The two remaining O atoms in the absorber Cu first coordination shell were then shifted by +0.2 Å along the *z* axis. The coordinates of the four Nb atoms closest to the absorbing Cu atom were changed by shifting the Nb1 atom +0.1 Å along the *z* axis, the two Nb2 atoms with negative *x* coordinates −0.2 Å along the *x* axis, and the one Nb2 atom with a positive *x* coordinate +0.1 Å along the *x* axis.

Copper has two characteristic absorption bands in the UV-VIS/IR spectrum of $LiNbO_3$:Cu. Copper in the valence state Cu^{1+} shows a band in the UV-VIS spectral range at 385 nm, whereas Cu^{2+} exhibits a band in the IR at 1040 nm [105, 140]. By measuring the corresponding absorption coefficients, Cu^{1+} and Cu^{2+} concentrations and hence the average formal oxidation state of Cu can be determined.

6.1.4 Results and discussion

Average formal oxidation state of Cu

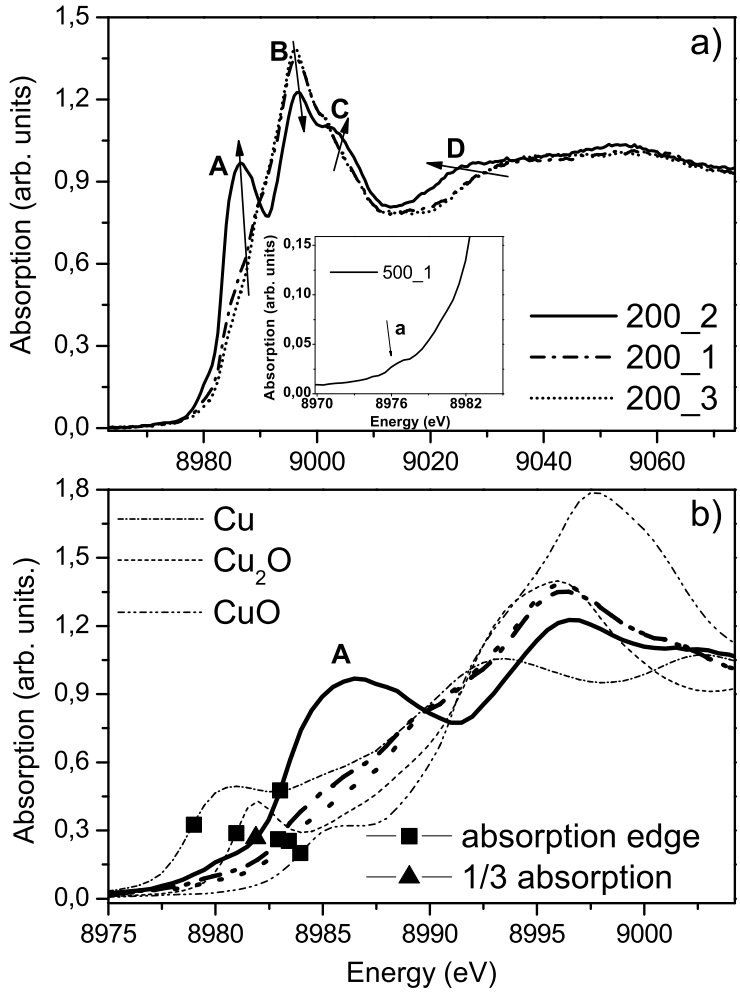

Figure 6.2: Cu K-XANES experimental spectra of the a) 200_1, 200_2 and 200_3 samples and b) compared to Cu, Cu_2O and CuO references over a smaller energy range. In the inset: the pre-edge region of the Cu K-XANES experimental spectrum of the 500_1 sample.

In Figure 6.2, the three spectra of the 200 sample series are plotted along with Cu, Cu_2O and $CuNb_2O_6$ reference spectra. The energy position of the series spectra are located between the Cu^{1+} and Cu^{2+} references, indicating a mixed valence state (Cu^{1+} and Cu^{2+}) of the copper atoms in the samples. The energy of the 200_2 spectrum lies closer to the Cu_2O reference spectrum, suggesting

Sample	X-ray results ± 0.2	IR/VIS results ± 0.2	Averaged value from the two methods ± 0.2
200_1	1.7	1.8	1.8
200_2	1.2	1.4	1.3
200_3	1.8	1.8	1.8
500_1	1.7	1.8	1.8
500_2	1.4	1.5	1.5
500_3	1.8	1.8	1.8
1000_1	1.7	1.8	1.8
1000_2	1.4	1.6	1.5
1000_3	1.8	1.8	1.8
2000_1_a	1.7	1.7	1.7
2000_1	1.4	1.4	1.4
3000_2_a	1.2	1.2	1.2

Table 6.2: Formal oxidation state of Cu for all studied samples determined by X-ray and IR/VIS absorption spectroscopy.

its having a higher valence than Cu^{1+}. The trends in the three spectra in Figure 6.2 a) also indicate a shift in copper oxidation state towards higher average valence going from the 200_2, to the 200_1, to the 200_3 samples. The A and C resonances increase as B decreases, and resonance D shifts towards lower energies with reduction of the formal copper valency. The minor changes in the 200_3 spectrum compared to the 200_1 spectrum may indicate that the 200_1 sample is already considerably oxidized during the diffusion process performed in air.

One way to quantitatively determine the formal valency of a metal oxide, is to determine the energy position of the absorption edges in comparison with suitable reference compounds. These positions can be defined, for example, as the first inflection points of the respective spectra, i.e., the maximum of the first intense peak in the first derivative spectrum. However, this widely applied approach is not valid for the spectra of the reduced samples as they exhibit structures on the rising edge of their XANES. For example, the energy positions of the first inflection points of the 200_1 and 200_2 spectra almost coincide; whereas the 200_2 spectrum is distinctly shifted towards lower energies [see Fig. 6.2 b)]. We therefore, define the absorption edge energy as the energy point 1/3 the absorption level of the normalized spectra [an example is displayed in Fig. 6.2 b)]. Similar approaches for defining absorption edges are found in the literature, e.g., the energy position of the maximum of a resonance on the absorption edge [201] or from the WL is used [156]. A linear model was employed to fit the edge energy position of the reference oxides Cu, Cu_2O and CuO as a function of copper valence 0, +1 and +2 formal oxidation states, respectively. This linear function was used as a calibration line to determine the average formal oxidation states of all samples; a graphical example of this empirical method can be seen in Ref. [134]. Within the error bars, the obtained values (Table 6.2) are in agreement with the values obtained from the absorption measurements in the IR and visible spectral ranges.

The 500_1 and 1000_1 Cu K-XANES spectra (not shown) resemble the 200_1 spectrum. There is no qualitative or quantitative evidence for changes in copper average valency in these three samples; the average valency of copper is 1.8 ± 0.2 in all three (see Table 6.2). Since the crystals are diffused simultaneously, this finding shows that the average formal oxidation state of copper

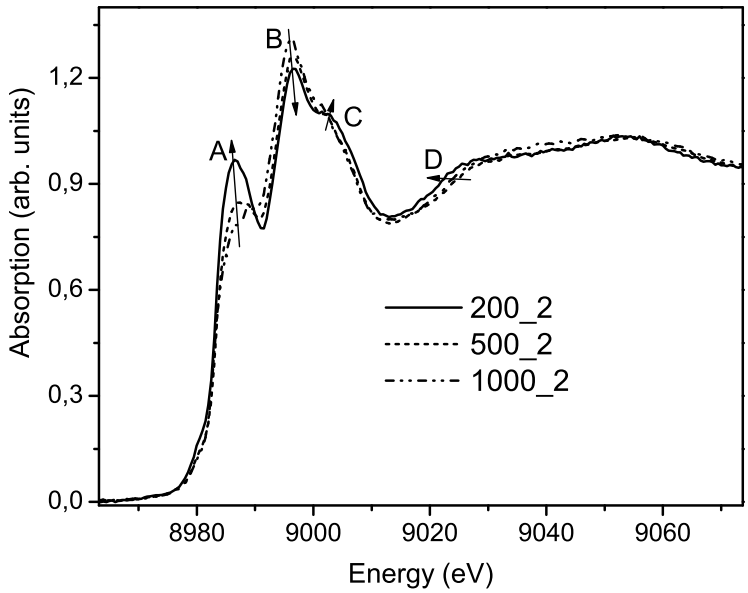

Figure 6.3: Experimental Cu K-XANES for the 200_2, 500_2 and 1000_2 samples.

does not depend on the copper concentration within the concentration range studied (0.1-0.3 wt% of Cu). The average formal copper valency is also the same for the three oxidized crystals, as the 500_3 and 1000_3 spectra (not shown) are identical to the 200_3 spectrum (Fig. 6.2). However, pronounced differences are present in the spectra of the simultaneously reduced samples, shown in Figure 6.3. Analogous trends in spectral changes in features A, B, C, D (Fig. 6.3) discussed above are observed here as a function of decreasing copper concentration. This indicates an increase in Cu^{1+} in the order 1000_2, 500_2, 200_2.

The average copper valency differs in the 2000_1_a, 2000_1 and 3000_2 crystals (Table 6.2), i.e., it is 1.7 ± 0.2 for the 2000_1_a sample, 1.4 ± 0.2 for the 2000_1 sample, and 1.2 ± 0.2 for the 3000_2_a sample. The Cu K-XANES spectra of the three samples are displayed in Figure 6.4. The resonance A, which increases with increasing contribution of Cu^{1+} (Fig. 6.4, Table 6.2), is observed in the 2000_1 and the 3000_2_a spectra. Clearly, it is possible to reach a desirable average Cu valency and high doping level of copper (0.3-0.7 wt% of Cu) by applying simultaneous or subsequent diffusion and annealing procedures. The Cu K-XANES spectra of samples with high concentration (Fig. 6.4) resemble the spectra of the LN crystals with low copper concentration, which suggests that there are no major electronic or geometrical structural differences in the highly doped crystals.

Local atomic environment of the Cu atoms

Figures 6.5, 6.6, 6.7 and 6.8 depict the EXAFS spectra (in R, q and k space) of all studied LN crystals. The fit results (Table 6.3) allow us to conclude that the Cu atoms occupy the Li site. Three Nb atoms are found at about 3.1 Å distance, varying from 3.04 Å to 3.15 Å from the indiffused to the reduced crystals. The model Cu_on_Li_site implies 3 Nb at 3.06 Å. The high scattering amplitude of the heavy Nb atoms leads to a pronounced peak A at around 3 Å. If Cu were located at Nb sites, backscattering from the lighter Li atoms at this distance would result in a significantly less pronounced feature. Moreover, the fingerprint for a Cu_on_Nb_site model, i.e., a distinct peak

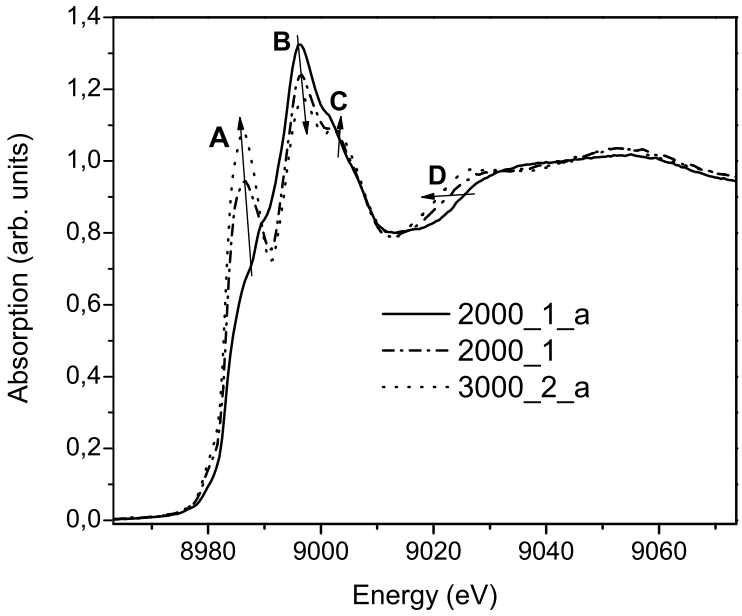

Figure 6.4: Experimental Cu K-XANES for the 2000_1_a, 2000_1 and 3000_2_a samples.

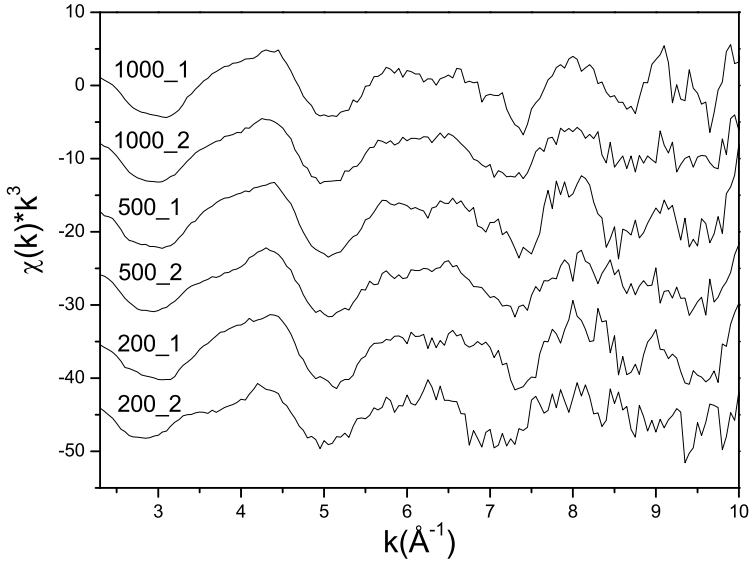

Figure 6.5: EXAFS spectra in k space of the 200_1, 200_2, 500_1, 500_2, 1000_1 and 1000_2 samples.

due to the Nb-Nb coordination at around 3.5 Å, is not present in the experimental spectra (see Fig. 6.7 and Fig. 6.8), also indicating that Cu does not occupy Nb sites.

In principle, the FT peak A (Fig. 6.7 and Fig. 6.8) might also be caused by scattering of the photoelectron on other heavy metal atoms, i.e., in our case other Cu atoms. Thus, we have assumed and tested two more models: incorporation of Cu into Li and Nb sites and formation of a copper oxide phase embedded within the $LiNbO_3$ matrix. In both cases, the quality of the fits using those models was poor, which gives us confidence to rule them out. Please note that this excludes presence of

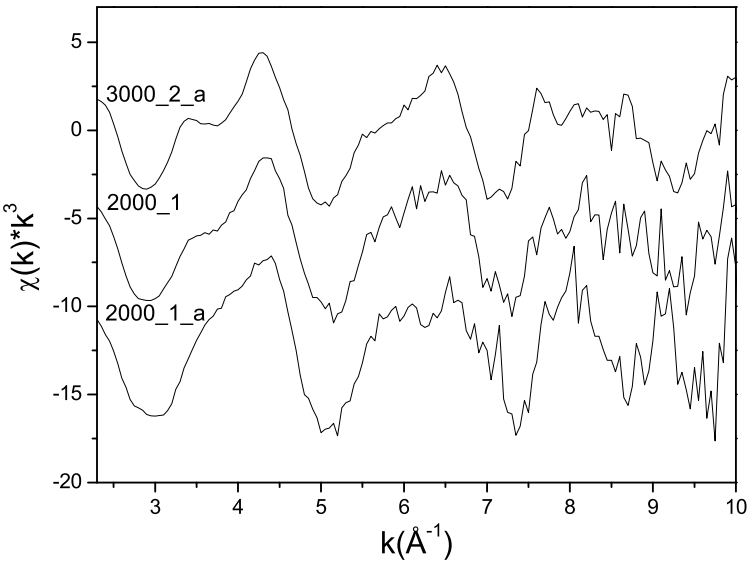

Figure 6.6: EXAFS spectra in k space of the 2000_1_a, 2000_1 and 3000_2_a samples.

Cu-O-Cu coordination in the copper-doped LN crystals.

After diffusion of Cu atoms, around 20% ± 15% Cu^{1+} and 80% ± 15% Cu^{2+} are found in the crystals (Table 6.1). After reduction of the doped crystals, the amounts are converted to around 80% ± 15% Cu^{1+} and 20% ± 15% Cu^{2+} (Table 6.1). Our results support strongly the hypothesis that there is just one site for all Cu atoms, independent of their formal valency, namely, the Li site. It is now important to identify the changes in the local geometry that are connected with valency changes due to oxidation/reduction.

Changes in the local coordination geometry upon changes in formal oxidation state are reflected in the reduced number of O atoms in the first coordination shell in the samples with average formal valency of Cu equal or lower than 1.5 ± 0.2 (Fig. 4 and 5, Table 6.3). The effect is most significant for the 200_2, 2000_1 and 3000_2_a samples showing a decrease in average coordination number from 6 O to around 3 O atoms. Changes in coordination symmetry with copper valence is also observed in the XANES spectra. The weak pre-edge peak at around 8978 eV (inset in Fig. 6.2) is not present in XANES spectra of compounds containing Cu^{1+} because of the completely filled Cu 3d shell. The pre-edge peak is assigned to a 1s-3d transition in the case of CuO by Bocharov et al. [21] However, in compounds with absent inversion symmetry, this feature can also be due to transition of the 1s electron to a molecular orbital, formed by hybridization of the O 2p and Cu 3d orbitals. The existence of the pre-edge peak can serve as a fingerprint for a high contribution of Cu^{2+}, and its energy position can serve as a fingerprint for site symmetry of the Cu^{2+} atoms [92, 118, 167]. This feature is also detectable in first derivative of a spectra. Figure 6.9 displays the pre-edge region of the first derivative XANES of all studied samples and references. The pre-edge peaks show up as maxima and are indicated with a line and arrows in the figure. The energy position of the XANES pre-edge peaks of the 200_3, 500_3, 1000_1, 1000_3 and 2000_1_a samples coincides with the one of the octahedral compound $CuNb_2O_6$. This feature, in contrast, is shifted by 1 eV to higher energies for the square planar compound CuO (Fig. 6.9). This suggests dominant octahedral site symmetry of the Cu^{2+} atoms in these samples. The coordination numbers obtained from the EXAFS analysis also suggest octahedral site symmetry of the Cu atoms in the crystals

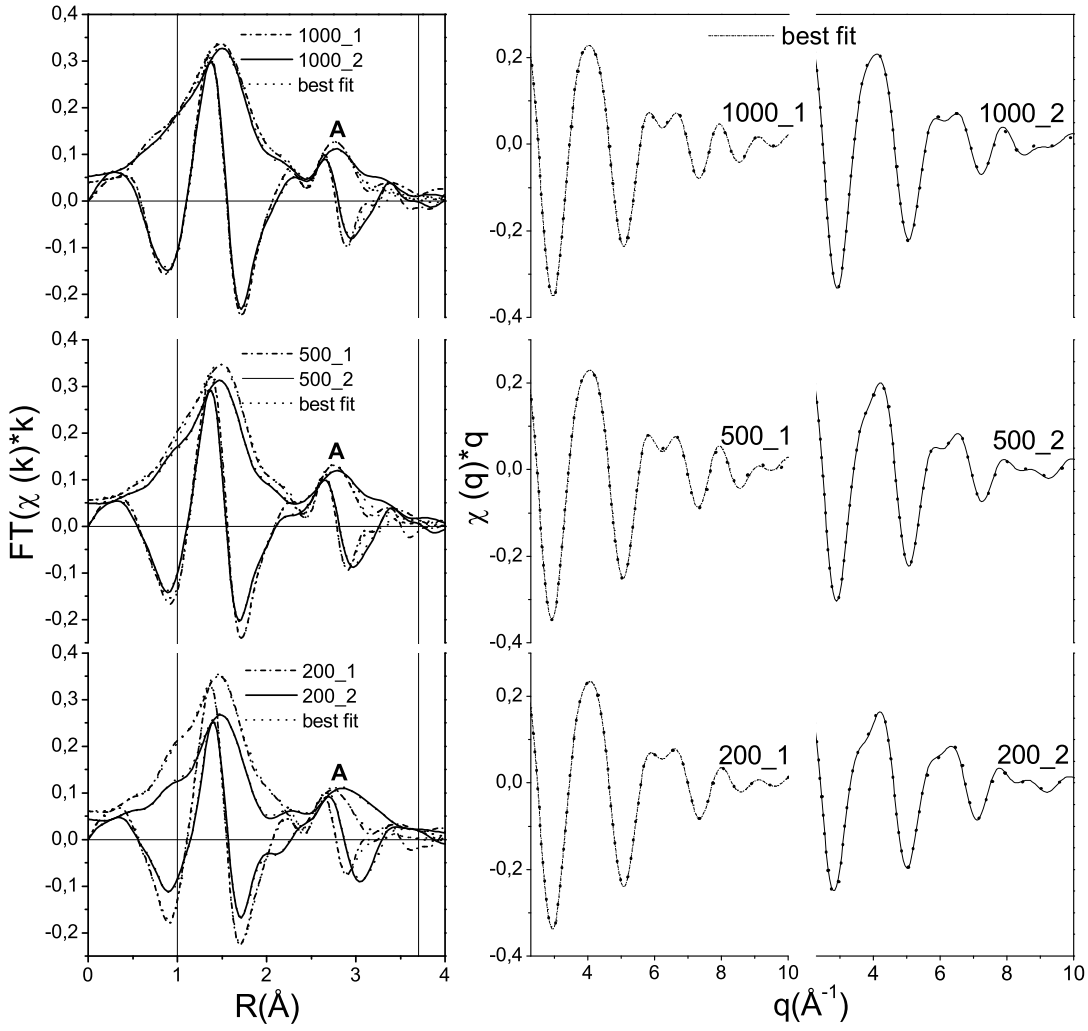

Figure 6.7: EXAFS spectra in R (amplitude and imaginary parts of the FT EXAFS spectrum) (left) and q (right) space and their best fits for the 200_1, 200_2, 500_1, 500_2, 1000_1 and 1000_2 samples.

with formal valency equal or higher than 1.7 ± 0.2.

We therefore can use the 200_1, 500_1 and 1000_1 Cu K-XANES spectra as a sort of reference containing mainly Cu^{2+} in an octahedral geometry and the 3000_2_a Cu K-XANES spectrum as a reference containing mainly Cu^{1+}. Linear combination least square fits of the 200_2, 500_2, 1000_2 and 2000_1 spectra were performed using the 200_1 and 3000_2_a spectra as Cu^{2+} and Cu^{1+} reference compounds. The aim was to verify whether Cu^{2+} atoms in an octahedral geometry contribute to the samples with formal valency equal or higher than 1.5 ± 0.2. An example from these analyses is shown in Figure 6.10. The linear combination of 30% of the 200_1 spectrum and 70% of the 3000_2_a spectrum is plotted along with the 2000_1 spectrum. The good agreement between simulated and experimental spectra and the finding that Cu^{2+} and Cu^{1+} atoms contribute about 40% ± 15% and 60% ± 15% respectively in the 2000_1 sample suggest that the Cu^{2+} atoms in the 2000_1 sample are mainly sixfold coordinated by O atoms and the Cu^{1+} atoms are twofold

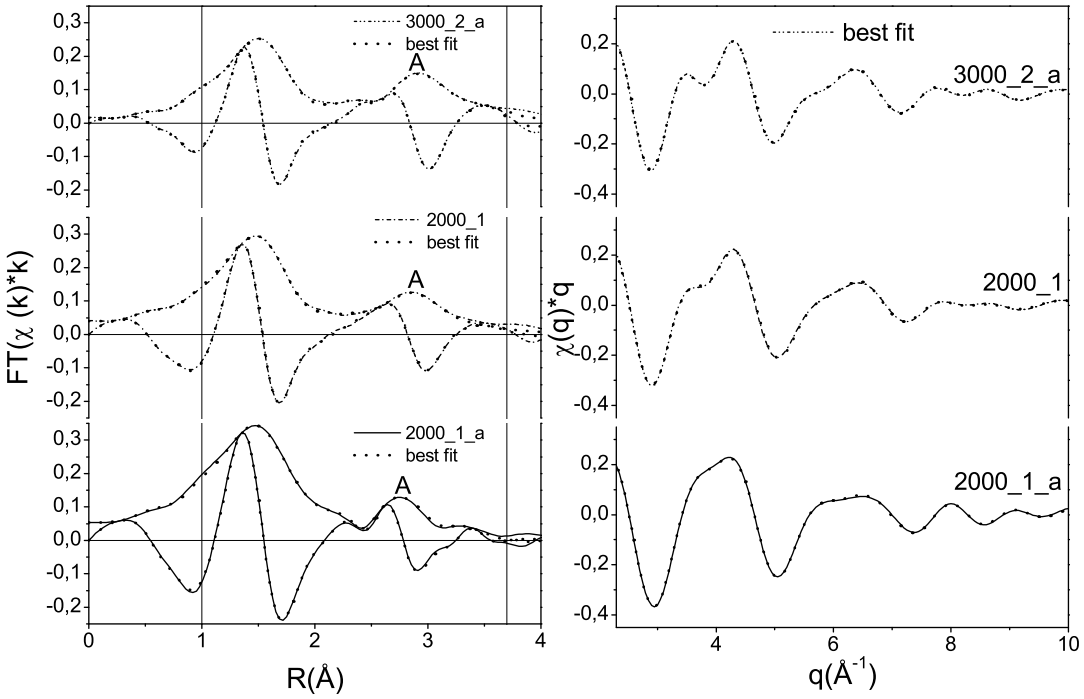

Figure 6.8: EXAFS spectra in R (amplitude and imaginary parts of the FT EXAFS spectrum) (left) and q (right) and their best fits for the 2000_1_a, 2000_1 and 3000_2_a samples.

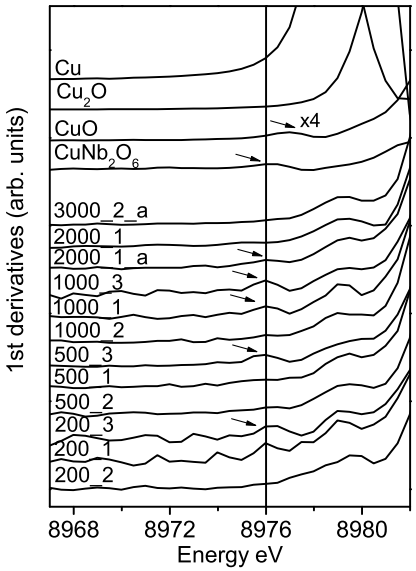

Figure 6.9: First derivative of the experimental Cu K-XANES spectra of all studied samples and Cu, Cu_2O, CuO and $CuNb_2O_6$ references.

coordinated by O atoms; 4 O atoms in average in the first coordination shell are found by the EXAFS analysis for this sample. This result is valid for all reduced crystals, as it was possible to simulate their spectra with linear combination of the 200_1 and 3000_2_a spectra (200_2: 30%

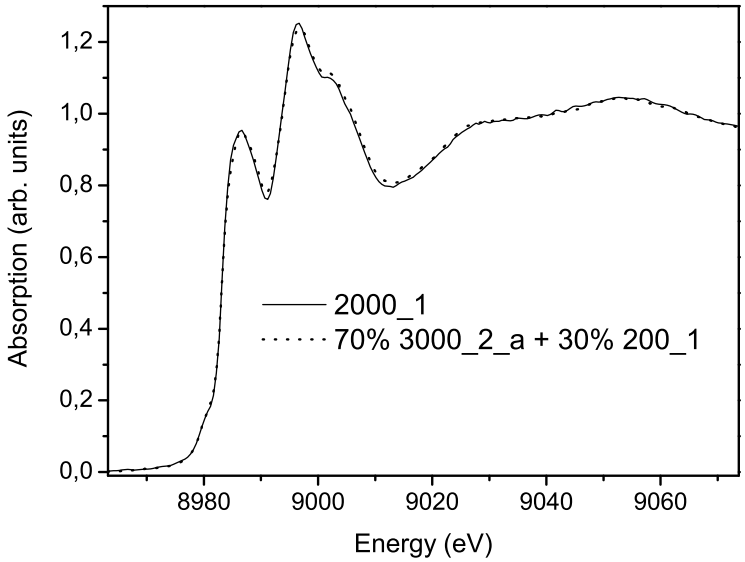

Figure 6.10: Experimental Cu K-XANES for the 2000_1 sample and a result of a linear combination least square fit using 70% 3000_2_a XANES and 30% 200_1 XANES.

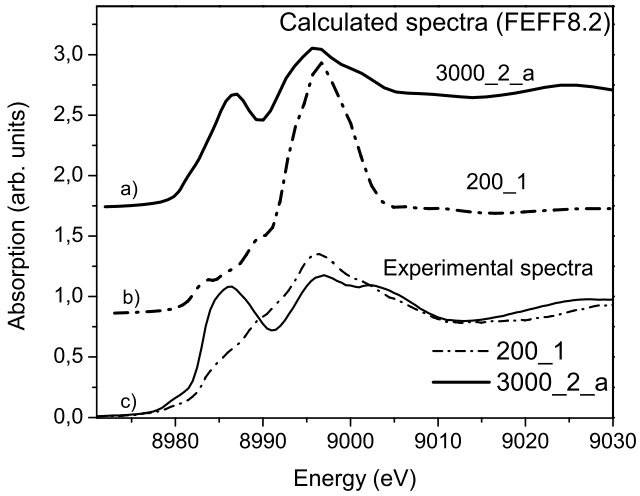

Figure 6.11: Simulated a) 3000_2_a and b) 200_1 Cu K-XANES spectra and c) experimental 200_1 and 3000_2_a Cu K-XANES spectra.

200_1 + 70% 3000_2_a; 500_2: 50% 200_1 + 50% 3000_2_a; 1000_2: 60% 200_1 + 40% 3000_2_a).

The resonance A [Fig. 6.2 a)] is assigned to the transition of the 1s electron to the doubly degenerated $4p_{x,y}$ state [92]. In their systematic XAS study of 19 Cu^{1+} and 40 Cu^{2+} containing compounds, Kau et al. showed that resonance in Cu K-XANES between 8983.5 and 8984.5 eV with an intensity comparable to the intensity of the WL of a conventionally normalized XANES spectrum appears in Cu K-XANES spectra of twofold coordinated Cu^{1+} compounds [92]. The presence of resonance A, which resembles that described by Kau at al. (Fig. 6.2-6.4) in the Cu K-XANES spectra of the reduced LN crystals confirms the EXAFS result that the Cu^{1+} atoms in these crystals are twofold coordinated. The resonance is most intense in the Cu K-XANES spectra of the crystals with highest

Cu^{1+} contribution (e.g., sample 3000_2_a with average copper valence 1.2).

In order to compare the Cu-O bond lengths for the crystals with formal valency of Cu ≤ 1.5 ± 0.2 and ≥ 1.7 ± 0.2, several factors should be considered. A bond length is influenced by the formal valency of the absorbing atom, electronegativity of the ligands and the local coordination symmetry. A metal-oxygen bond distance increases with a decrease in the formal oxidation state of the metal, e.g., Ref. [24]. This trend is valid for the Cu-O bond distance in the Cu^{1+} containing compounds Cu_2O (1.85 Å, ICSD 63281) compared to the Cu-O distance in the Cu^{2+} compound CuO (1.69 Å, ICSD 67850). Site symmetry also has a significant influence on the metal-oxygen bond length. The Cu^{2+} compound $CuNb_2O_6$, which has Cu in octahedral coordination, has a Cu-O bond length (1.97 Å , ICSD 74424), 0.12 Å longer than CuO with square planar coordination. Such a symmetry variation could explain almost the same Cu-O distance for the indiffused and reduced samples obtained from the EXAFS analysis.

The obtained σ^2_{Cu-O} parameters are comparable to values obtained from temperature dependent EXAFS study of copper-doped magnesium oxides [84]. We consider this material an appropriate model system, because the nearly perfect octahedral oxygen coordination of the Cu^{2+} ions at room temperature distorts at higher temperatures. Moreover, the Cu^{2+} (0.73 Å) and Mg^{2+} (0.72 Å) have almost the same ionic radii,[166] which explains the result that the substitution of Mg by Cu does not lead to significant structural distortion [84]. The σ^2_{Cu-O} parameters in Ref. [84] vary from 0.012 $Å^2$ (300 K) to 0.024 $Å^2$ (1500 K). Comparison of these values to the σ^2_{Cu-O} values obtained for our copper-doped LN crystals (0.006-0.013 $Å^2$) indicate that our crystals have undistorted sixfold coordinated Cu^{2+}. The reduced distortion of the octahedral Li site compared to undoped LN can be explained by the differing ionic radii of Li^{1+} (0.63 Å, sixfold coordination) and Cu^{2+} (0.73 Å, sixfold coordination) [166].

Contrary to a near invariant Cu-O bond distance, the Cu-Nb distance is affected by the reduced formal valency and average oxygen coordination of the Cu atoms. The Cu-Nb distance increases with increasing copper reduction. For example, the 200_1 sample has a Cu-Nb2 distance of 3.04 ± 0.01 Å, whereas this distance in the 200_2 sample is 3.14 ± 0.01 Å (see Table 6.3). This result suggests that the incorporated Cu atoms cause local structural disorders, i.e., local changes in the crystallographic parameters of the $LiNbO_3$ crystal. Formation of crystalline phases other than $LiNbO_3$ is reported by X-ray diffraction studies on LN crystals doped with copper by an ion exchange method [34]. However, copper is inhomogeneously distributed in the sample studied in Ref. [34], whereas this is not the case for the copper-doped LN crystals studied here. See Ref. [139] for an example of a typical copper distribution profile.

Simulation of the Cu K-XANES spectra

In Figure 6.11, the experimental and theoretical Cu K-XANES spectra calculated with the FEFF8.2 [154] code for the 3000_2_a and 200_1 samples are shown. These samples are selected as they are representatives of the two copper coordination symmetries twofold coordinated: Cu^{1+} and sixfold coordinated Cu^{2+}. In our simulation approach the atom coordinates of the atomic cluster used in the calculations were modified in order to reproduce values obtained from EXAFS analysis for distances, within the error bars up to ~3 Å, and coordination numbers. For simulation of the 200_1 spectrum, the used distances are Cu-O = 1.98 Å, Cu-Nb1 = 3.0 Å and Cu-Nb2 = 3.04 Å. For simulation of the 3000_2_a spectrum, the distances are Cu-O = 2.01 Å, Cu-Nb1 = 3.11 Å and Cu-Nb2 = 3.16 Å. It was not sufficient to modify only the coordinates of the atoms of the first two shells for the 200_1

	N	Nm	R (Å) ± 0.01	R-Rm (Å)	s^2 (Å^2) ± 0.001	N	Nm	R (Å) ± 0.01	R-Rm (Å)	s^2 (Å^2) ± 0.001	N	Nm	R (Å) ± 0.01	R-Rm (Å)	s^2 (Å^2) ± 0.001
			200_1					500_1					1000_1		
O1	6.0	3.0	1.98	-0.08	0.012	6.0	3.0	2.00	-0.07	0.012	6.0	3.0	2.0	-0.06	0.013
O2		3.0					3.0					3.0			
Nb1	1.0	1.0	2.99	-0.02	0.012[a]	1.0	1.0	3.01	0.00	0.010	1.0	1.0	3.02	0.01	0.010
Nb2	3.0	3.0	3.04	-0.02	0.012[a]	3.0	3.0	3.05	0.00	0.010	3.0	3.0	3.06	0.01	0.010
O3	3.0	3.0	3.22	-0.06	0.012	3.0	3.0	3.22	-0.06	0.012	3.0	3.0	3.24	-0.05	0.013
			200_2					500_2					1000_2		
O1	3.4±0.4	3.0	2.01	-0.06	0.005	4.4 ±0.2	3.0	1.99	-0.07	0.007	5.5±0.5	3.0	2.01	-0.05	0.012
O2		3.0				1.1±0.3	3.0	2.25	0.01	0.007		3.0			
Nb1	1.0	1.0	3.09	0.08	0.007	1.0	1.0	3.09	0.08	0.019[a]	1.0	1.0	3.03	0.02	0.012[a]
Nb2	3.0	3.0	3.14	0.08	0.007	3.0	3.0	3.14	0.09	0.019[a]	3.0	3.0	3.07	0.02	0.012[a]
O3	1.7±0.7	3.0	3.14	-0.14	0.005	3.0	3.0	3.21	-0.07	0.007	2.3±0.8	3.0	3.15	-0.13	0.012
Nb3	3.0	3.0	3.30	-0.08	0.007										
			2000_1_a					2000_1					3000_2_a		
O1	6.0	3.0	1.99	-0.07	0.012	4.2±0.3	3.0	1.99	-0.08	0.008	3.3±0.2	3.0	2.00	-0.06	0.006
O2		3.0					3.0					3.0			
Nb1	1.0	1.0	3.01	0.00	0.011	1.0	1.0	3.08	0.07	0.016	1.0	1.0	3.10	0.09	0.007
Nb2	3.0	3.0	3.06	0.00	0.011	3.0	3.0	3.13	0.08	0.016	3.0	3.0	3.15	0.10	0.007
O3	3.0	3.0	3.21	-0.08	0.012	3.2±0.4	3.0	3.16	-0.12	0.008	2.0±0.4	3.0	3.24	-0.05	0.006
Nb3	3.0	3.0	3.72	0.30	0.011	3	3.0	3.21	-0.17	0.016	3.0	3.0	3.29	-0.08	0.007
O5											0.7±0.2	3.0	4.06	0.13	0.006

Table 6.3: Results of the EXAFS analyses. The type of atom neighboring the absorbing Cu atom is given in the first column. The structural parameters and the employed model are in the remaining columns: N: coordination numbers, R (Å) distances, Nm coordination numbers of the Cu into the Li site model, R − Rmodel (Å), Debye-Waller factors: σ^2 (Å^2).

[a] the error bar is: ±0.002

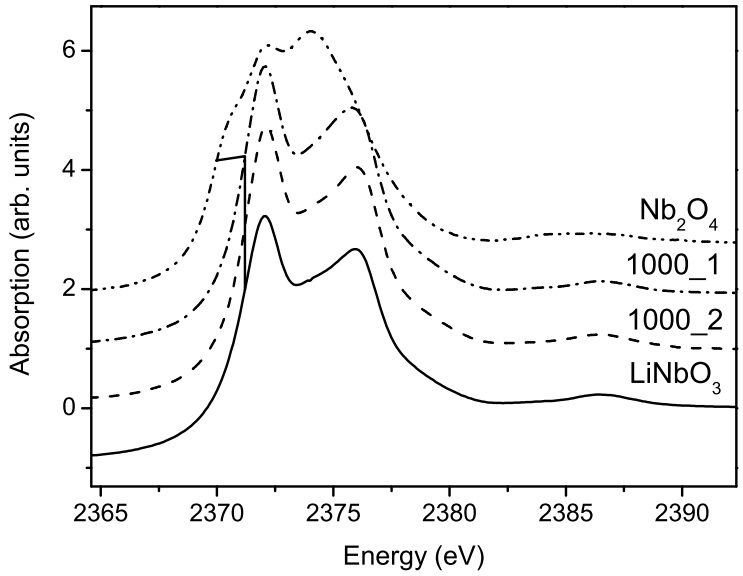

Figure 6.12: Nb LIII-XANES experimental spectra of the 1000_1 and 1000_2 samples and Nb_2O_4 and $LiNbO_3$ references.

spectrum (see section III). Therefore, additional refinements of atomic coordinates of the more distant atoms were done until close agreement between the experimental and simulated spectra was achieved. A similar approach for reproduction of an experimental XANES spectrum is followed by using the MXAN package [16, 128]. In this package the initial atomic coordinates of a model compound with known structure are refined and a XANES spectrum is repeatedly calculated until the experimental and theoretical spectra closely agree. The refined distances between the absorber and the closest neighboring atoms are compared to these obtained from EXAFS analysis and XRD [128].

There is at least one configuration of atomic coordinates leading to satisfactory agreement between calculated and experimental spectra of the 200_1 and 3000_2_a samples that accounts for the EXAFS results. Refined atomic coordinates from the XANES simulations support the hypothesis of the existence of two different Cu sites, i.e., twofold and sixfold coordinated by O atoms, in the samples with formal valency of Cu equal to or lower than 1.5 ± 0.2. The calculations demonstrate the usefulness of a top-down approach refining atomic coordinates by using EXAFS results as initial input to obtain good agreement between experimental and calculated spectra.

Charge compensation mechanism

The average number of oxygen ions next to Cu is reduced from 6 to 3 upon reduction of the doped LN crystals (Table 6.3). This finding suggests that one of the mechanisms, providing charge compensation upon reduction of the doped crystals, is the outgassing of O atoms. In principle, the reduction treatment might lead not only to a lower formal valency of copper, but also to a change in the formal oxidation state of the Nb atoms, i.e., from an initial 5+ formal valency to a lower one. In order to identify Nb valence changes the Nb LIII-XANES spectra of the copper doped LN have been recorded. The spectra for samples 1000_1 and 1000_2 are shown in Figure 6.12 as

examples and compared to spectra for $LiNbO_3$ (Li^{1+}, Nb^{5+}) and Nb_2O_4 (Cu^{2+}, Nb^{4+}) references. The LIII absorption edge of Nb of the Nb^{4+} reference is shifted around 1.2 eV towards lower energies compared to the Nb^{5+} reference compound (Fig. 6.12). The 1000_1 and 1000_2 spectra do not exhibit any energy shift compared to that of $LiNbO_3$. This result suggests that the formal oxidation state of Nb remains 5+ after reduction of the doped LN crystals.

Let us examine possible mechanisms for charge compensation. In case of reduction of all Cu atoms in the 3000_2_a crystal (0.3 wt% of Cu), 0.2% of all O atoms should leave the structure for charge compensation (Cu atoms are 1.3% of all Li atoms). The EXAFS analyses suggest that Cu atoms do not share the same O atoms, as no Cu-O-Cu coordination was found (Table 6.3); hence, the number of the outgassed O atoms leading to oxygen vacancies should be four times of all copper atoms, which is ~1.7% all O atoms. Charge compensation for the remaining ~1.5% O atoms must come through reduction of ~2.2% Nb atoms from Nb^{5+} to Nb^{4+}. However, at least 6% of the Nb atoms must have formal oxidation state 4+, in order to shift the Nb LIII-XANES spectrum 0.1 eV towards lower energies. The error bar in energy position of the Nb LIII edge is estimated as 0.1 eV, which is the width of one step. Reduction of Nb atoms, theoretically likely, cannot be detected, because the energy resolution is not sufficient.

6.1.5 Conclusion

The performed XAS studies lead to the following conclusions:

(1) The average formal oxidation state of Cu in all samples is between Cu^{1+} and Cu^{2+} (Table 6.2).

(2) It was found that the average formal valency of Cu does not notably depend on the Cu concentration (for the range 0.1-0.3 wt% of Cu) upon simultaneous diffusion and oxidation of the doped crystals. However, it does depend on the Cu concentration upon reduction of the doped crystals.

(3) Strong experimental evidence was found that the Cu atoms occupy dominantly Li sites for all samples. It was possible to distinguish between Cu^{1+} and Cu^{2+} sites: (i) the Cu^{2+} atoms are sixfold coordinated by O atoms in the LN crystals having a formal Cu valence equal to or higher than 1.7 ± 0.2 (ii) Cu^{1+} atoms are twofold coordinated and Cu^{2+} sixfold coordinated by O atoms in the LN crystals, having formal Cu valency equal to or lower than 1.5 ± 0.2.

(4) Upon reduction of the doped LN crystals, one of the charge compensation mechanisms is outgassing of O atoms.

(5) No experimental evidence for metal copper or copper oxide cluster formation in the LN matrix was found, even for the highly doped LN crystals (0.3-0.7 wt% of Cu).

(6) Change in the formal oxidation state of the Nb atoms upon reduction of the crystals is necessary for charge compensation, but was not detected by the XAS measurements at the Nb LIII-edge due to the expected change being lower than the attainable energy resolution.

Understanding the microstructure of the copper centers, as well as the charge compensation mechanisms during the reduction process is essential for fine-tuning the optical properties of copper-doped LN crystals. Moreover, insight into the site-symmetry of the impurity centers can help interpreting the deviating from a perfect Gaussian shape UV-VIS/IR absorption spectra (see, e.g., Ref. [75]).

6.2 Manganese-doped lithium niobate

6.2.1 Introduction

The material and structural parameters of iron-doped LN crystals have been extensively studied [31, 53, 134, 139, 170]. LN crystals doped with Mn (LN:Mn) are of particular importance since they have a number of advantages. It was shown (e.g., for Fe, Cu or Mn) that a high level of impurity centers leads to a greater refractive index change [53, 140, 208]. However, the dark decay time of a hologram decreases with increasing dopant concentration and this restricts the practical doping level. [53, 140, 208] The energy level connected to Mn centers is deeper in the gap between the valence and conduction bands than that of Fe centers [184]; thus, higher practical doping levels of Mn with acceptable dark decay constants are feasible [208]. In addition, the usual decrease of the sensitivity of a hologram, as a consequence of the increased level of Mn^{3+}, is not observed in highly doped (0.5 wt%) LN:Mn crystals [208]. A high doping level of Mn^{3+} centers is desirable in order to attain a high dynamic range. Furthermore, manganese is of particular interest since it allows persistent data storage [33].

One of the still open questions is whether only Mn^{2+} and Mn^{3+} are present in a LN:Mn crystals [137, 158, 208] or also Mn with higher formal oxidation state [208]. The combination of VIS and X-ray Absorption (XAS) and High Resolution non-resonant X-ray Emission Spectroscopy (HRXES) measurements are suitable for answering this question. Furthermore, the X-ray Absorption Near Edge Structure (XANES) technique is an appropriate tool for determining the formal oxidation state of Mn in the LN:Mn crystals [134].

The site of incorporation of Mn in different oxidation states in LN crystals is still a matter of a discussion. Three experimental studies [Electron Paramagnetic Resonance [119] (EPR) (Mn^{2+}), Electron Nuclear Double Resonance [39] (ENDOR) (Mn^{2+}) and XAS [212] (Mn^{2+})] and two theoretical studies (Mn^{2+} and Mn^{3+}) [50], (Mn^{2+}) [203] show that the Mn impurity centers are incorporated into the Li sites. Another theoretical study suggests that Li and Nb sites are the energetically favorable Mn incorporation sites (Mn^{2+}) [11]. We report an EXAFS investigation of the site of incorporation of Mn in as-grown, reduced and oxidized crystals LN:Mn 1wt%.

The electron tunneling mechanism dominates the dark decay of a hologram in highly doped LN crystals [131, 207]. According to this mechanism, the dark decay probability depends on the distances between the impurity centers [208], which get closer to each other with increasing doping level. The Extended X-ray Absorption Fine Structure (EXAFS) technique probes the local structure around the absorbing atom up to ≈6 Å, which makes it capable of not only detecting close neighboring Mn atoms but also of identifying their trapping sites.

The aims of our study include verification of the applicability of the thermo-electric oxidization [52] method for oxidation of Mn atoms in LN:Mn crystals. This technique proved to be an excellent method for complete oxidation of Fe:LN crystals [52, 134]. The formal oxidation state of Mn in thermo-electrically oxidized, as-grown, and reduced Mn:Mn 1wt% crystals, as well as LN crystals with various doping levels of Mn (0.05-0.5 wt%), are determined by XANES analysis. By comparing XANES results with VIS absorption spectra, the question will be answered whether Mn atoms with a higher than Mn^{3+} formal oxidation state exist in the LN:Mn crystals. In addition, we will clarify whether this third formal valency of Mn is present in the LN:Mn 1 wt% as-grown, reduced, and oxidized crystals by comparing the high resolution $K\beta_{1,3}$ emission lines of the crystals with those of suitable reference compounds. EXAFS analysis is used to characterize the incorporation site/s of

the Mn atoms in highly doped as-grown, reduced and oxidized LN:Mn 1wt% crystals and to identify whether Mn atoms are close neighbors (~4Å) in these crystals.

6.2.2 Samples

The studied congruently-melting LNcrystals are grown by the Czochralski technique by Shanghai Crystals, China. The doping is done by adding MnO to the melt. The concentrations of Mn in all studied LN crystals and the notations of the crystals are given in Table 6.4.

6.2.3 Experimental details

The XAS experiments were also performed at the INE-Beamline at ANKA. For energy monochromatization a set of Si(111) crystals was employed in the DCM. The Mn-doped LN crystals were ground and absorption spectra of the powder samples and MnO, Mn_2O_3, and MnO_2 references were recorded at the Mn K-edge (6539 eV) in fluorescence mode. The reference samples were diluted with cellulose in order to avoid saturation and self-absorption effects.

All Mn K-edge XANES spectra were measured in the energy interval from 6490 to 6700 eV, with 0.5 eV step width and 2 s integration time. At least six XANES spectra were collected from each sample and reference and at least eight EXAFS spectra from the LN:Mn 1wt% as-grown, reduced, and oxidized crystals, in order to check reproducibility of the spectral features and to improve counting statistics. For energy calibration, the first inflection point of the K-edge spectrum of a manganese foil measured simultaneously was set to the photon energy of 6539 eV. The data reduction of the XANES spectra consisted of subtraction of a linear background fitted to the pre-edge region from 6490 to 6530 eV and normalization of the spectra to an edge jump of one at 6700 eV.

The absorption measurements of all LN:Mn crystals studied (as-grown, reduced, and oxidized LN:Mn 1wt% and LN:Mn 0.05-0.5 wt%) were performed in the VIS spectral range in transmission geometry with a CARY spectrometer. Mn^{3+} has a characteristic absorption band at around 575 nm [76].

Measurements of the Mn K$\beta_{1,3}$ non-resonant high-resolution emission lines of the $LiNbO_3$ crystals doped with 1 wt% Mn (LN:Mn 1wt%), as-grown, reduced, and oxidized, as well as MnO, Mn_2O_3, and MnO_2 references, were performed at the wiggler beamline W1 at HASYLAB. The incident X-rays were monochromatized by two Si(111) crystals to an energy of 6700 eV, which is approximately 160 eV above the Mn K-edge. X-rays scattered from the sample were energy analyzed by using of a Johann spectrometer in dispersive geometry [196]. A spherically bent Si(440) crystal with a radius of curvature of 1 m was employed as an analyzer and a CCD camera (Roper Scientific/Princeton Instruments type) as a position sensitive detector. The measurements were performed at a Bragg angle of θ_B= 84.17°, and the energy range of the fluorescence radiation monitored by the CCD camera was 17 eV. The experimental resolution was estimated as 1.3 eV at the K absorption edge of Mn (6539 eV).

The ARTEMIS [151] program package was used for the EXAFS analyses. The X-ray Absorption Fine Structure (XAFS) signals [χ(k)] measured at the Mn K-edge in a k range from 2.3-11 $Å^{-1}$ were Fourier-transformed to R space using a k weighting of 1, 2, and 3, with a Hanning window having window sills dk equal to 2. The fit was performed in R space over a range from 1-3.6 Å. The structure of $LiNbO_3$ (ICSD 28294) was used for the initial model. The amplitude reduction

notation of the samples and the spectra	LN:Mn wt%	formal oxidation state of Mn	XANES	VIS	EXAFS	HRXES
C1	0.05	2.6 ± 0.2	×	×		
C2	0.1	2.4 ± 0.2	×	×		
C3	0.2	2.3 ± 0.2	×	×		
C4	0.5	2.6 ± 0.2	×	×		
	LN:Mn 1 wt%					
C5AG	as-grown	2.8 ± 0.2	×	×	×	×
C5RE	reduced	2.6 ± 0.2	×	×	×	×
C5OX	oxidized	2.9 ± 0.2	×	×	×	×

Table 6.4: The notations of all LN:Mn crystals, the concentration of Mn in wt%, the average formal oxidation state of Mn determined by XANES analyses and the used structural characterization techniques.

factor was hold constant at 0.74, the value obtained by a fit of a FT-EXAFS spectrum of a Mn foil measured under the same experimental conditions. For all fits, the obtained $\mathfrak{R}$ factor (overall goodness of fit) was 0.02 or better, which means that data and fit agree on average within 2% or better.

For thermo-electric oxidization (see Fig. 6.13) [52] the crystals were heated up to 700 °C, the temperature kept for 6 hours and then the samples were cooled down to room temperature. During the whole process an electrical field of 500 V/mm was applied to the crystals, while the current density was limited to 0.01 $\mathrm{mA/mm^2}$. At elevated temperatures around 500 °C the current limit was reached and the voltage was lowered automatically. At a temperature of 700 °C an electrical field of about 50 V/mm was present. During cooling the field roses again. The oxidization was performed in air.

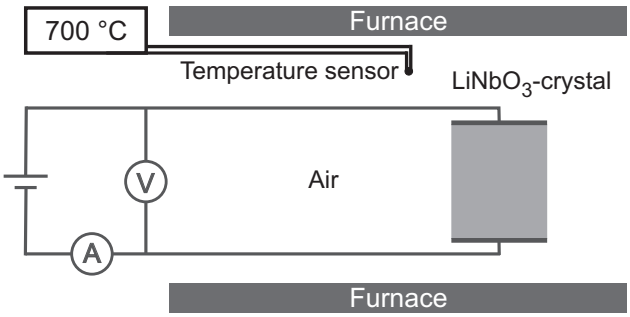

Figure 6.13: A schematic view of the experimental set-up for thermo-electric oxidization.

The reduction of the crystals was performed in a partial hydrogen atmosphere (10^{-3} mbar). The crystals were heated up to 1000 °C for 24 h. The temperature was changed with 10 °/min.

6.2.4 Results

XANES analysis

In Figure 6.14, the experimental Mn K-edge XANES spectra of the C5AG, C5RE, and C5OX samples are plotted along with the spectra of the reference compounds containing Mn^{2+} (MnO),

	C5AG			C5RE			C5OX			used model	
	R(Å) ±0.01	N	σ^2 (Å^2) ±0.001	R(Å) ±0.01	N	σ^2 (Å^2) ±0.001	R(Å) ±0.01	N	σ^2 (Å^2) ± 0.001	R(Å)	N
O1	2.09	6	0.012	2.09	5.6±0.7	0.009	2.07	6	0.018	2.07	3 Mn_Lisite
O2										2.24	3 Mn_Lisite
O1										1.89	3 Mn_Nbsite
O2										2.11	3 Mn_Nbsite
Nb1	3.08	1	0.008	3.08	1	0.008	3.09	1	0.008	3.01	1 Mn_Lisite
Nb2	3.12	3	0.008	3.12	3	0.008	3.13	3	0.008	3.05	3 Mn_Lisite
Nb3	3.14	3	0.008	3.11	3	0.008	3.10	3	0.008	3.38	3 Mn_Lisite
Mn	3.23	2.9±0.4	0.008	3.22	1.7±0.5	0.008	3.25	2.5±0.6	0.008	3.14	3 MnO
O	3.97	8	0.012	3.98	8	0.009	3.98	8	0.018	3.85	3 MnO
Nb1	3.73	6	0.008	3.74	6	0.008	3.75	4.5±1.2	0.008	3.76	6 Mn_Nbsite

Table 6.5: The results from the EXAFS analyses of the C5AG, C5RE, and C5OX crystals. The structural parameters are named as follows: N: coordination numbers, R (Å): distances, σ^2 (Å^2): Debye-Waller factors.

.

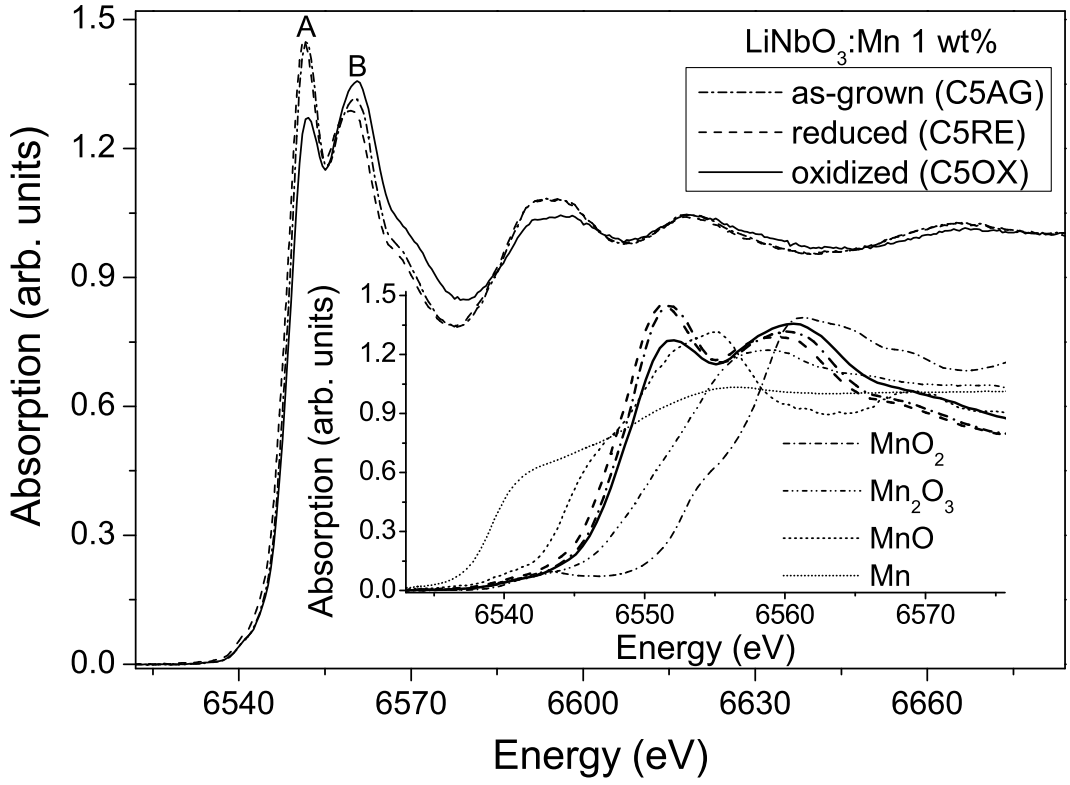

Figure 6.14: Mn K-edge XANES experimental spectra of the C5AG, C5RE, and C5OX crystals, and spectra of the MnO, Mn_2O_3, and MnO_2 reference compounds are shown in the inset.

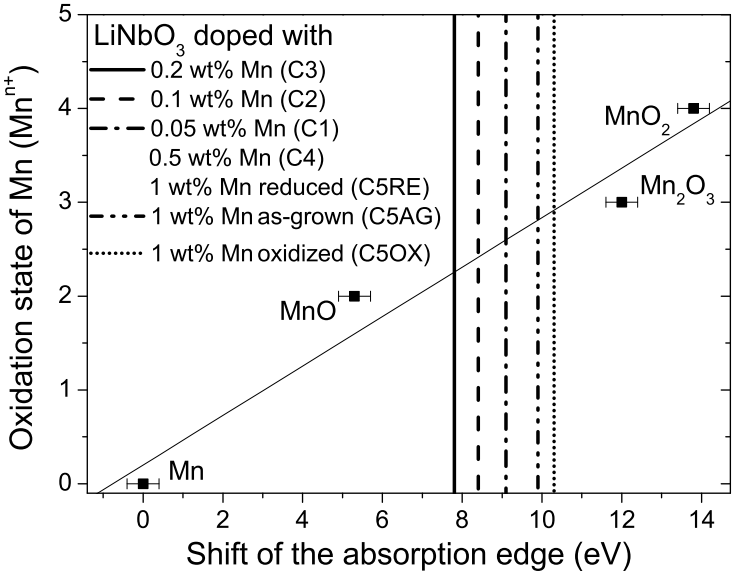

Figure 6.15: Determination of the formal oxidation state of Mn in all LN:Mn crystals.

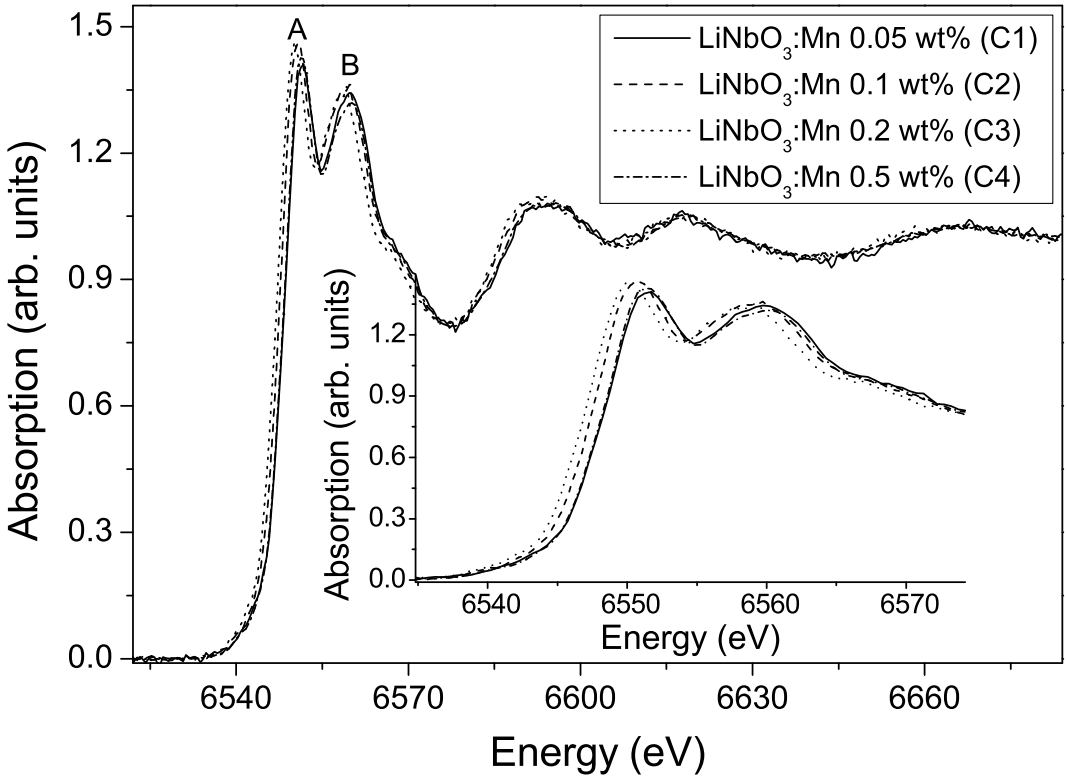

Figure 6.16: Mn K-edge XANES experimental spectra of the C1, C2, C3 and C4 crystals. The near edge region of the spectra is magnified in the inset.

Mn^{3+} (Mn_2O_3), and Mn^{4+} (MnO_2). Compared to the C5AG spectrum, the energy of the C5RE spectrum is shifted towards that of the MnO reference, whereas the C5OX spectrum is shifted towards Mn_2O_3. The absorption edges of all samples and references were defined as the maximum of the first peak in the first derivative of their XANES spectrum. The dependence of the energy position of the absorption edge of Mn from the formal oxidation state of Mn in the MnO, Mn_2O_3, and MnO_2 reference compounds was fit with a linear regression (see Fig. 6.15). This was used to determine the formal oxidation state of Mn in the LN:Mn crystals (see Fig. 6.15 and Table 6.4). The obtained values for the formal oxidation state of Mn in the C5AG, C5RE, and C5OX samples are 2.8 ± 0.2, 2.6 ± 0.2 and 2.9 ± 0.2, respectively. Comparing the three spectra (Fig. 6.14) we observe a difference in the amplitudes of the resonances A and B in the WL regions of the spectra. For example, the amplitude of resonance A in the C5RE spectrum is significantly higher than that in

ions	d_i^{Li}	d_i^{Nb}
Mn^{2+}	0.320	1.575
Mn^{3+}	0.861	0.296
Mn^{4+}	1.900	0.765

Table 6.6: Calculated d_i values for Mn ions occupying Li (d_i^{Li}) or Nb cites (d_i^{Li}). The unites are valence unites (v.u.)

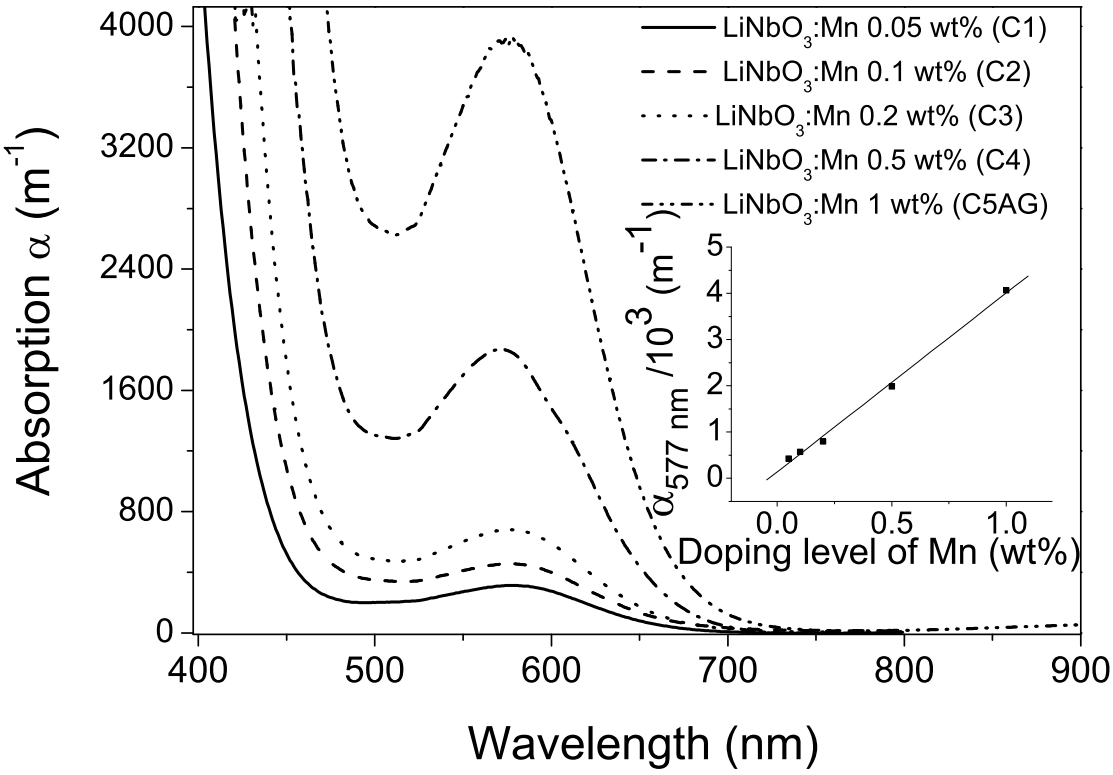

Figure 6.17: VIS absorption spectra of the C1, C2, C3, C4 and CAG crystals.

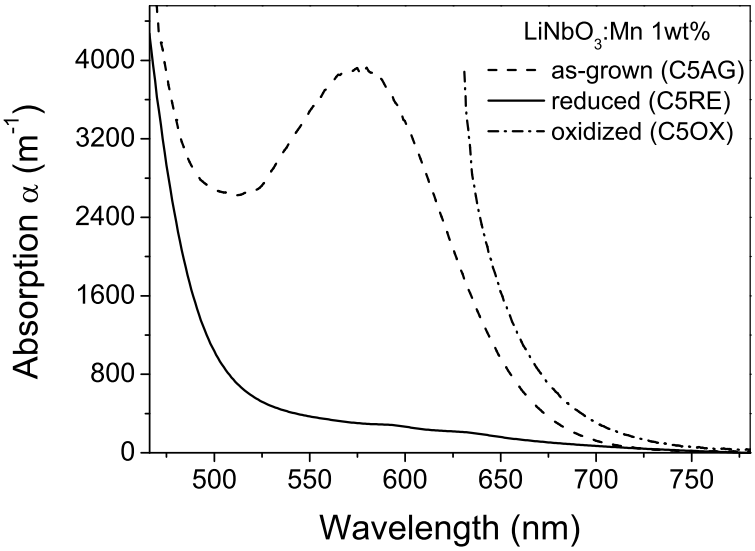

Figure 6.18: VIS absorption spectra of the C5AG, C5RE, and C5OX crystals.

the C5OX spectrum. The amplitude of resonance B behaves the opposite way, i.e., it is lower in the C5RE spectrum compared to the C5OX spectrum. The resonances A and B might be assigned to

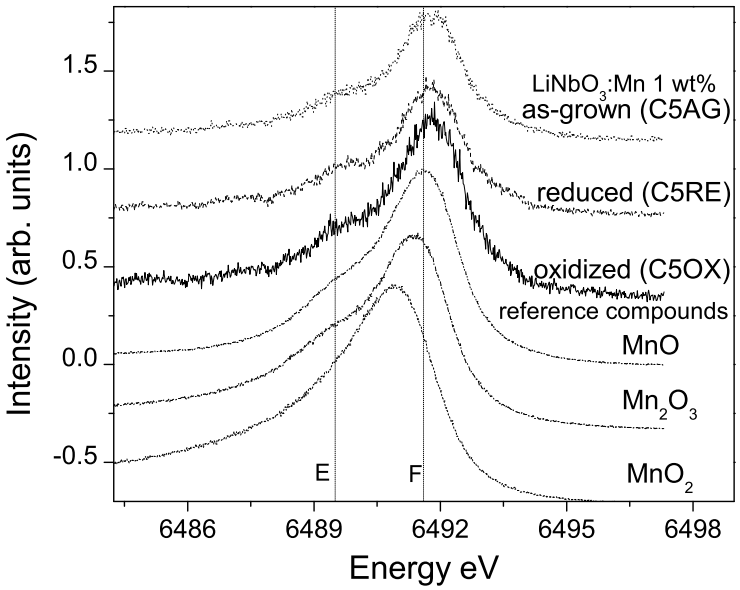

Figure 6.19: The K$\beta_{1,3}$ emission lines of the C5AG, C5RE, and C5OX crystals and the MnO, Mn_2O_3 and MnO_2 reference compounds.

contributions from Mn^{2+} and Mn^{3+} sites respectively. A similar effect is observed in the Cu K-edge XANES and Fe K-edge XANES spectra of Cu- and Fe-doped LN crystals. In the case of LN:Cu, it is shown that the effect is caused by changes in the contributions from Cu^{1+} and Cu^{2+} sites [191] (see Section 6.1.4).

In Figure 6.16, the C1-C4 spectra of the LN crystals doped with 0.05, 0.1, 0.2, or 0.5 wt% Mn are displayed. The formal oxidation state of Mn also differs in these samples. Mn in the C3 crystal is the most reduced (2.3 ± 0.2) and the C1 and the C4 crystals have the most oxidized Mn from the group (2.6 ± 0.2) (see Table 6.4).

VIS absorption analysis

The VIS absorption spectra of the C1-C4 and C5AG samples are plotted in Figure 6.17. Yang et al. assigned the band at 577 nm to Mn^{3+} [208]. The amplitude of the VIS absorption band increases linearly with the Mn concentration (see inset Fig. 6.17).

The VIS absorption spectra of the C5AG, C5RE, and C5OX samples are plotted in Figure 6.18. The VIS band vanishes after reduction, whereas its amplitude drastically increases after oxidation of a LN:Mn 1 wt% crystal.

HRXES

In Figure 6.19, the non-resonant high-resolution K$\beta_{1,3}$ emission lines of the C5AG, C5RE, and C5OX crystals are plotted along with the respective spectra of the MnO, Mn_2O_3, and MnO_2 references. The shoulder on the low energy side of the 1s3p emission line (marked with line E) for MnO and Mn_2O_3 is due to the spin flip of one electron in the 3d state upon transition of one electron from the

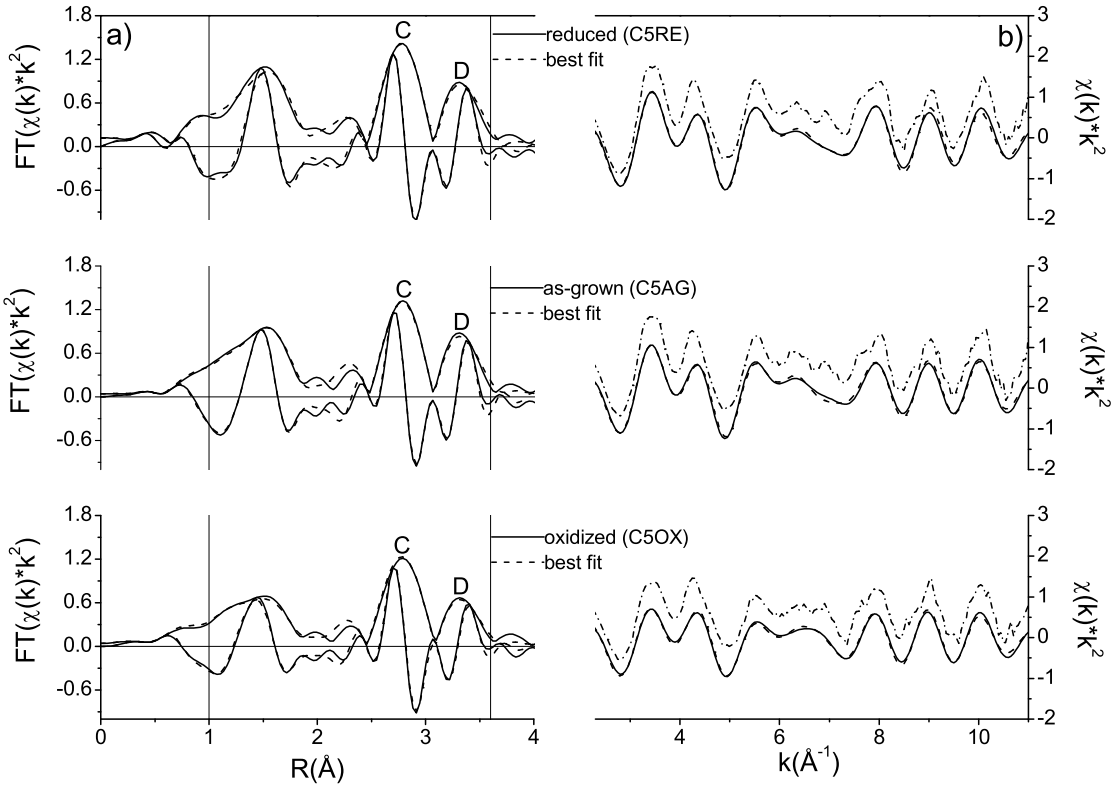

Figure 6.20: The EXAFS spectra and their best fits in R (magnitude and imaginary curves) a) and q space b) of the C5AG, C5RE, and C5OX crystals. The EXAFS spectra in k space (dash dot) are shown in b) too.

3p to the 1s state [64, 65, 144]. The shoulder is not present in the emission line of MnO_2 and missing in the Mn^{4+} compounds shown in Ref. [144] and [64]. The shoulder is present in the emission lines of all crystals. This finding suggests that Mn^{2+} and Mn^{3+} are the major species present, even in the oxidized crystal. Moreover, from these spectra there is no evidence for existence of Mn^{4+} in the three crystals. Figure 6.19 shows that the K$\beta_{1,3}$ line shifts towards lower energies with increasing formal Mn oxidation state. The emission lines of the three crystals are clearly shifted to higher energies with respect to those of the three reference oxides. The structural differences between the three crystals and the reference oxides could account for this effect. In Ref. [64] it is shown that the energy position of the K$\beta_{1,3}$ emission line for different compounds having Mn in the same formal valency slightly varies.

EXAFS analysis

The obtained structural values (see Table 6.5) for the three crystals are very similar. A model with Mn incorporated into the Li sites (Mn_Lisite) was first employed in the EXAFS analysis. The first coordination shell at around 2 Å was fit with 6 oxygen atoms, where the two distances expected from the model were not resolved. It was not possible to fit the characteristic peak C in Figure 6.20 with only 4 Nb atoms (Nb1 and Nb2), according to the model. Additional 3 Nb (Nb3) atoms and approximately 3 Mn atoms were required in order to obtain a good fit. This result suggests that the

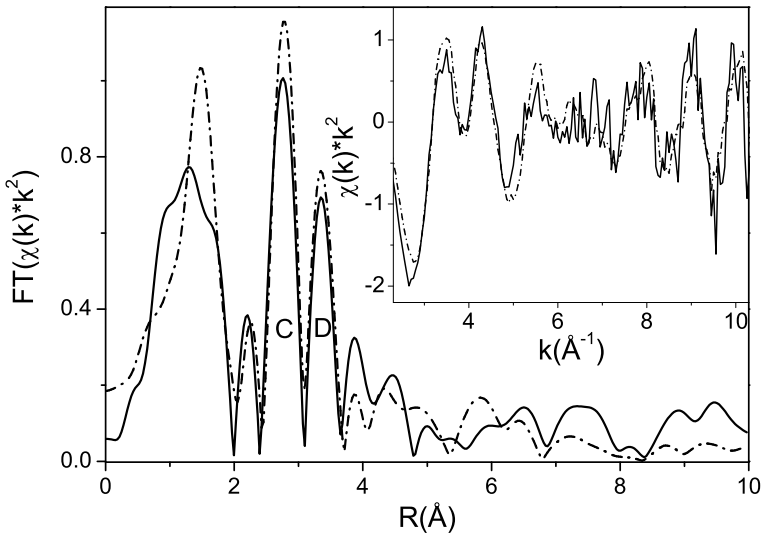

Figure 6.21: The FT EXAFS spectra of the C1 (solid) and CAG (dash dot) crystals. The EXAFS spectra in k space are shown in the inset.

3 Nb atoms at 3.38 Å from the Mn_on_Li_site model are closer to the absorbing Mn atom. A small contribution of MnO clusters (Mn-O-Mn coordination) was assumed in order to fit completely this coordination shell. The next pronounced peak at around 3.8 Å (see Fig. 6.20 peak D) was fit with 6 Nb atoms according to a model of Mn occupying Nb sites (Mn_Nbsite).

In Fig. 6.21, the FT EXAFS spectra of the C1 (0.05 wt% Mn) and C5AG (1 wt% Mn) crystals are displayed. Despite the high noise level in the C1 spectrum, an overall similarity of the two spectra is obvious in the regions, where the Mn-Nb single scattering paths contribute (see Fig. 6.21 peaks C and D).

Bond Valence Model

The incorporation site of ions in different formal oxidation states in a LN crystal has been predicted by applying the Bond Valence Model (BVM) [203]. The difference between normal valence state and bond valence sum, i.e., a parameter d_i (see Sec. 6.4 for details), is compared for ions trapped in Li (d_i^{Li}) or Nb (d_i^{Nb}) sites. The more probable trapping site (Li or Nb) is the one, which yields smaller di value. Large d_i value mean a strained bond, which causes instability in the crystal structure. The d_i values for three different formal oxidation states of Mn determined by the BVM are given in Table 6.6. The BVM predicts that Mn ions with formal oxidation state higher than 2+ incorporate Nb sites.

6.2.5 Discussion

Incorporation site of the Mn atoms

Obviously, the Mn atoms do not occupy only one distinct site. The results from the EXAFS analysis imply however, that the Mn atoms do not occupy neighboring Li and Nb sites. The presence of

a small percentage of MnO clusters in the LN:Mn 1wt% crystals can explain why the electron tunneling mechanism dominates the dark decay of a hologram in crystals highly doped with Mn.

The BVM predicts that Mn atoms with formal oxidation state higher than 2+ are incorporated into Nb sites. This agrees with the EXAFS result, i.e., Mn atoms are incorporated into Li and Nb sites. Doping concentrations over a certain threshold, depending on the LN stoichiometry and the dopant ion, also induce changes of the doping site, i.e., from Li to Nb sites (see, e.g., Ref. [203]). However, the C5AG FT-EXAFS spectrum is very similar to the C1 FT-EXAFS spectrum (see Fig. 6.21), which indicates that Mn atoms occupy Li and Nb sites already at low doping concentrations; therefore, it is more likely that a less strained bond governs the choice of trapping site.

Formal oxidation state of the Mn atoms

The amplitude of the VIS absorption spectrum of the thermo-electrically oxidized LN:Mn crystal (C5OX) increases drastically, which agrees with the increase of the average formal oxidation state of Mn in this sample (from 2.8 ± 0.2 to 2.9 ± 0.2). This suggests that the thermo-electric oxidation is an appropriate method for strong oxidation, not only of iron-doped but also of manganese-doped LN crystals.

The XANES results indicate that the reduction and oxidation treatments lead to changes in the formal valency of Mn, i.e., to variations in the relative amounts of Mn^{2+} and Mn^{3+}. The VIS results imply that Mn^{3+} increases linearly with the Mn concentration. However, one has also to consider the average formal oxidation state of Mn (Table 6.4). For example, the C3 sample (0.2 wt% Mn) is more "reduced" than the C1 sample (0.05 wt% Mn). This deviation from the linear trend and from one average formal oxidation state suggest the presence of Mn^{2+}, Mn^{3+}, and Mn in a formal oxidation state higher than 3+ in the C1 and C3 crystals. The assumption that a third Mn species with oxidation state higher than 3+ exists in the LN:Mn crystals is supported also by the XANES result and the VIS absorption spectrum of the reduced crystal (C5RE) (Table 6.4, Fig. 6.18). There is no VIS absorption band at around 577 nm in Figure 6.18, although the C5RE sample has an average formal oxidation state higher than 2, i.e., 2.6 ± 0.2. However, impurity traps with Mn valency higher than 3+ must be filled first upon reduction, because of they are energetically lower than Mn^{3+}. If the reduced Mn^{3+} to Mn^{2+} centers do not change their site, they incorporate Nb sites, according to the BVM. As a result, two different Mn^{2+} sites (Li and Nb) may be present in the reduced crystal. The influence of the geometric structure around the absorbing atom on the energy position of the absorption edge is a known effect (see, e.g., Ref. [54]). For example, Farges shows Mn K-edge XANES spectra of two Mn^{2+} octahedral compounds with different crystal structures (MnO and $MnCO_3$), which have ~4.5 eV difference in the energy position of the absorption edges [54]. This hypothesis is supported by the HRXES results, which do not provide any evidence for existence of Mn with higher formal oxidation state than 3+ in the C5AG crystal.

6.2.6 Conclusion

The XAS, non-resonant HRXES and VIS absorption spectroscopy studies lead to the following conclusions:

(1) Mn atoms are incorporated both into Li and Nb sites in the C5AG, C5RE, and C5OX crystals, where these two sites are not neighboring. It is unlikely that selection of Nb trapping site is induced

by high Mn concentrations. The BVM predicts that Mn atoms with formal oxidation state higher than 2+ preferably occupy Nb sites. Indications for a small amount of MnO clusters were also found.

(2) The thermo-electric oxidization method led to oxidation of Mn^{2+} to Mn^{3+} (from 2.8 ± 0.2 to 2.9 ± 0.2). The reduction treatment caused full elimination of the Mn^{3+} site, leading to lower average Mn formal oxidation state (from 2.8 ± 0.2 to 2.6 ± 0.2). The higher than 2+ average formal oxidation state of the reduced crystal is possibly due to presence of two different Mn^{2+} sites (Li and Nb). Direct evidence for presence of Mn valency higher than 3+ was not found in the C5AG, C5RE, and C5OX crystals.

(3) The average formal oxidation state of Mn in the LN:Mn crystals with various doping levels of Mn (0.01-1 wt% Mn) is between 2+ and 3+. The deviation from a linear relation between average formal oxidation state and concentration, and from one average formal oxidation state might be due to existence of Mn valency higher than 3+.

6.3 Iron-doped lithium niobate

6.3.1 Introduction

Though light-induced refractive index changes are favorable for some applications, they are undesirable for others and called "optical damage". Some ppm of iron always exist in LN crystals. Upon illumination, refractive patterns develop, which disturb the phase matching conditions and the beam profile in nonlinear-optical applications. One way to avoid the "optical damage" in a LN crystal is to oxidize it. We apply here, a novel thermo-electric method for very efficient oxidation of Fe^{2+} to Fe^{3+} in LN:Fe crystals [52, 53].

Precise knowledge about the oxidation state and site occupation of the iron atoms is essential for tuning the photorefractive properties of the LN crystals. A recent X-ray Absorption Spectroscopy (XAS) study reported presence of Fe^{2+} and Fe^{3+} atoms in iron-doped LN crystals and their incorporation into the Li site [134]. However, no site-selective structural information was provided, which would allow to differentiate between the Fe^{2+} and Fe^{3+} sites.

The goals of the study presented here are: first, to determine the incorporation site of the Fe atoms in LN crystals doped with 2 and 4wt% of Fe (LN:Fe 2wt%, LN:Fe 4wt%) by the EXAFS technique; second, to verify that Fe^{2+} and Fe^{3+} are present in these LN crystals by analyzing their XANES and visible VIS absorption spectra; third, to provide site-selective information about the local symmetry and incorporation site of the Fe^{2+} and Fe^{3+} atoms by in situ XAS measurements of thermo-electric oxidization of a $LiNbO_3$:Fe 2wt% crystal, non-resonant HRXE spectroscopic measurements and analyses of partially site-selective XANES spectra extracted from a Resonant Inelastic X-ray Scattering (RIXS) map.

6.3.2 Samples

The studied samples are iron-doped $LiNbO_3$ crystals supplied by Crystal Technology, Inc.. They were grown by the Czochralski technique from a congruent melt that contained 2 or 4 wt% iron oxide (Fe_2O_3). The $LiNbO_3$:Fe 2wt% and $LiNbO_3$:Fe 4wt% crystals are denoted as C1 and C2 crystals, respectively.

6.3.3 Experimental details

XAS experiments were performed at the INE-Beamline at ANKA with Si(111) crystals in the DCM. The iron-doped LN crystals were ground and absorption spectra of the powder samples and the FeO and Fe_2O_3 references were taken at the Fe K-edge in fluorescence and transmission modes, respectively.

All Fe K-edge XANES spectra were measured in the energy interval from 7060 to 7260 eV, with a 0.5 eV step width and 2 s (in fluorescence mode) or 1 s (in transmission mode) integration time. At least six XAS (XANES and EXAFS) spectra were collected from the LN:Fe 2wt% and LN:Fe 4wt% crystals, in order to check for reproducibility of the spectral features and to improve the counting statistics. For energy calibration, the first inflection point of the K-edge spectrum of an iron foil measured simultaneously was set to the photon energy of 7112 eV. The data reduction of the Fe K-edge XANES spectra consisted of subtraction of a linear background fit to the pre-edge region from 7060 to 7100 eV and normalization of the spectra to an edge jump of one at 7260 eV.

During the in situ XAS measurements of the thermo-electric oxidization of a LN:Fe 2wt% crystal, the monochromator was operated in a quick scanning mode, with one minute measuring time per EXAFS spectrum. The LN crystal was mounted under 45 degrees with respect to the incoming photon beam. The crystal was put in a furnace in the middle of two perpendicularly crossed quartz tubes (see Fig. 6.13). The first tube was directed towards the fluorescence detector. The second tube provided access to the sample for the primary beam. In order to oxidize the crystal thermo-electrically, an electric field was initially applied, where the voltage and current were restricted to 1000 V and 0.1 mA, respectively. Then the crystal was heated to 700 °C with a ramp of 3.9°C/min and abruptly cooled down. At room temperature the electric field was switched off [52].

The measurements of the Fe K$\beta_{1,3}$ and Kβ' emission lines of FeO and Fe_2O_3 references and the RIXS map of the LN:Fe 4wt% crystal were performed at the wiggler beamline W1 at HASYLAB (Hamburg). For the HRXE measurements, the incident X-rays were monochromatized by two Si(111) crystals to the energy of 7500 eV, which is approximately 300 eV above the Fe K-edge. X-rays scattered from the sample were energy analyzed by a Johann spectrometer in dispersive geometry [196], where for the HRXE measurements and the RIXS measurement the sample was moved by 200 mm and 100 mm, respectively inside the Rowald circle. A spherically bent Si(531) crystal with radius of curvature of 1 m was employed as an analyzer and a CCD camera (Roper Scientific/ Princeton Instruments type) as a position-sensitive detector. The measurements were performed at a Bragg angle θ_B=71.7°. The experimental energy resolution is estimated as 1.4 eV at the Fe K-edge (7112 eV).

The ARTEMIS [151] program package was used for EXAFS analyses. From the X-ray Absorption Fine Structure (XAFS) signals [χ(k)] measured at the Fe K-edge covering a k range from 2.4 to 8.4 $Å^{-1}$ was Fourier-transformed to R space using a k weighting of 1, 2 and 3 and a Hanning Window with window sills dk equal to 2. Fits were performed in R space over a 1-3.4 Å range. As the initial model the structure of $LiNbO_3$ (ICSD 28294) was used. The amplitude reduction factor was held constant to 0.75, the value obtained for initial fits for a Fe foil FT-EXAFS spectrum measured under the same experimental conditions. For all performed fits, the obtained r-factor (overall goodness of fit) was 0.01 or better, which means that data and fit agree on average within 1% or better.

The measurement of the absorption coefficient of the 2 wt% iron-doped $LiNbO_3$ crystal was performed at 477 nm in transmission mode using a CARY 500 spectrometer in the VIS spectral range. Using the known relation [106] between Fe^{2+} concentration ($c_{Fe^{2+}}$) and the absorption at 477 nm ($\alpha_{477\ nm}$), $c_{Fe^{2+}} = 2.16\times10^{21}\ m^{-2}\alpha_{477\ nm}$, the concentration of Fe^{2+} was calculated. An independent measurement by atomic absorption spectroscopy of the $LiNbO_3$:Fe 2 wt% crystal leads to a total iron concentration of 1.11 ± 0.03 wt%.

6.3.4 Results and discussions

EXAFS analyses

The EXAFS spectra in R and k space of the C1 and C2 crystals are plotted along with their best fits in Figure 6.22. The structural values obtained by fitting the intense peak at around 1.5 Å (not phase corrected) suggest that the Fe atoms are sixfold coordinated by oxygen atoms in both samples (see Table 6.7). Best fits in the R-range up to 3.4 Å were achieved by employing a model with Fe atoms occupying Li sites, i.e., 3 Nb atoms located at around 3.05 Å and 3.14 Å for the C1 and C2 crystals, respectively (see Table 6.7). Fits using models of Fe_2O_3 clusters and incorporation

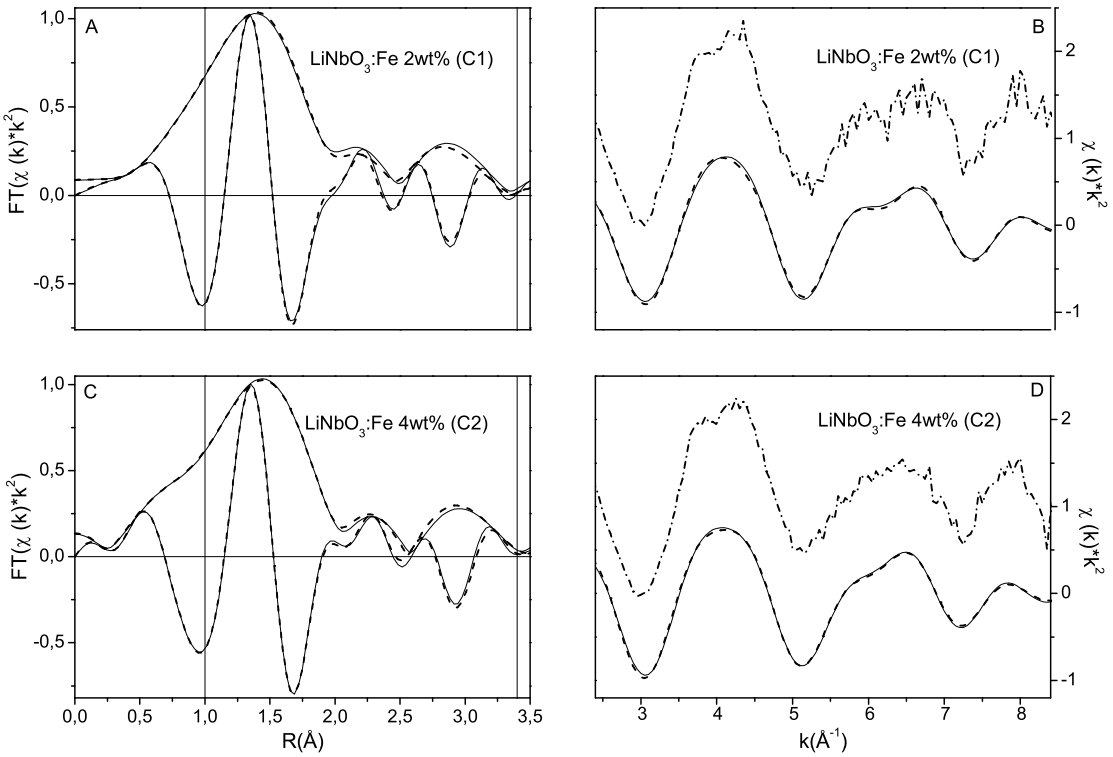

Figure 6.22: EXAFS spectra of the LN:Fe 2wt% (A and B) and LN:Fe 4wt% (C and D) crystals in R (distance) (A and C) (the magnitude and imaginary part) and k (wavenumber) (B and D) [the experimental (dash dot) and Fourier filtered data (solid)] space and their best fits (dash).

of Fe atoms into Li and Nb sites yielded unsatisfactory results, which made us confident to rule them out. Results from the EXAFS analysis suggest that the iron atoms are dispersed in the LN:Fe 4wt% crystal. This contradicts the result of Olimov et al., who reported indications for formation of small iron oxide (Fe_2O_3) clusters in a LN:Fe 4wt% crystal [134]. The crystal studied in this paper and by Olimov et al. originate from the same crystal boule. The discrepancy might be due to a inhomogeneous distributing iron oxide in the boule. This scenario is likely, because of the high doping level of iron. The significantly increased Fe-Nb distance in the case of the C2 crystal, from 3.05 to 3.14 Å, provides evidence for distortion of the LN crystal matrix, which might be caused by a decreased distance between the Fe centers.

XANES and VIS absorption analyses

Figure 6.23 depicts the XANES spectra of the C1 and C2 crystals along with those of the FeO and Fe_2O_3 reference compounds. On the energy scale, the spectra of the two samples are positioned close to the spectrum of Fe_2O_3, which indicates a major presence of Fe^{3+} and a minor presence of Fe^{2+} in both crystals. This qualitative estimate is supported by the VIS absorption result, which found 20% of Fe^{2+} and 80% of Fe^{3+} in the 2wt% iron-doped LN crystal. The energy positions of the absorption edge of Fe in the two samples, determined as the maximum of the first derivative of the respective XANES spectrum, are identical. This finding implies a similar Fe^{2+} to Fe^{3+} ratio in

	LN:Fe 2 wt% (C1)			LN:Fe 2 wt% (C2)			used model: Fe_on_Li_site	
	R(Å) ±0.01	N	σ^2 (Å^2) ±0.001	R(Å) ±0.01	N	σ^2 (Å^2) ±0.001	R(Å)	N
O1	1.98	6.6±0.5	0.011	2.00	6.9±0.6	0.012	2.07	3
O2							2.24	3
Nb1	3.01	1	0.011	3.10	1	0.012	3.01	1
Nb2	3.05	3.3±0.6	0.011	3.14	2.1±0.6	0.012	3.05	3
O3	3.28	3	0.011				3.29	3

Table 6.7: The results from the EXAFS analyses of the LN:Fe 2 wt% (C1) and LN:Fe 4 wt% (C2) spectra and the values of the structural parameters of the used Fe_into_the_Li_site model. The structural parameters are named as follows: N: coordination numbers, R (Å): distances, σ^2 (Å^2): Debye-Waller factors.

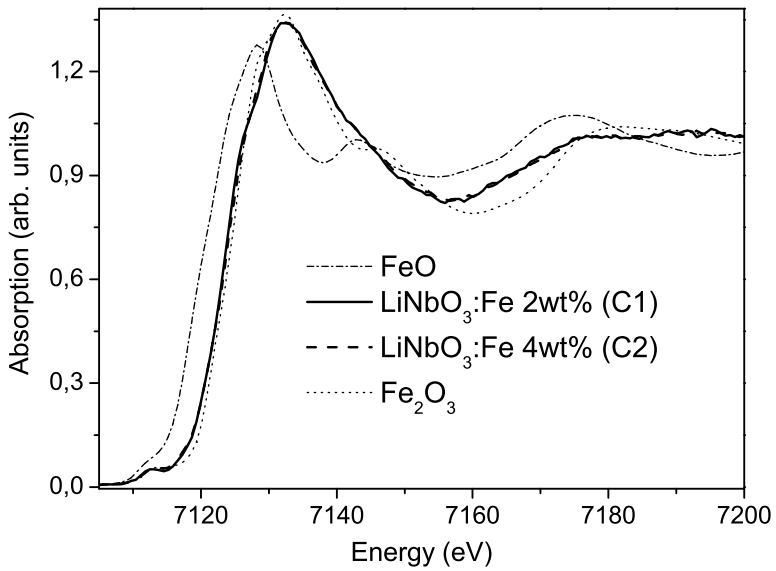

Figure 6.23: Fe K-edge XANES experimental spectra of the LN:Fe 2wt% and LN:Fe 4wt% crystals and the FeO and Fe_2O_3 references.

both crystal.

The overall shape of a XANES spectrum reflects the electronic and geometric structure of both Fe^{2+} and Fe^{3+} sites, which makes the extraction of site-selective structural information difficult. The in situ thermo-electric oxidization of LN:Fe 2wt% aimed not only to track the structural changes around the Fe atoms during the oxidation process but also to enable the assignment of spectral features to one of the two sites (Fe^{2+} and Fe^{3+}).

In situ studies

During thermo-electric oxidization, iron-doped LN crystals change their color from completely black to completely transparent [52]. This fingerprint was the first sign for successful oxidation of iron

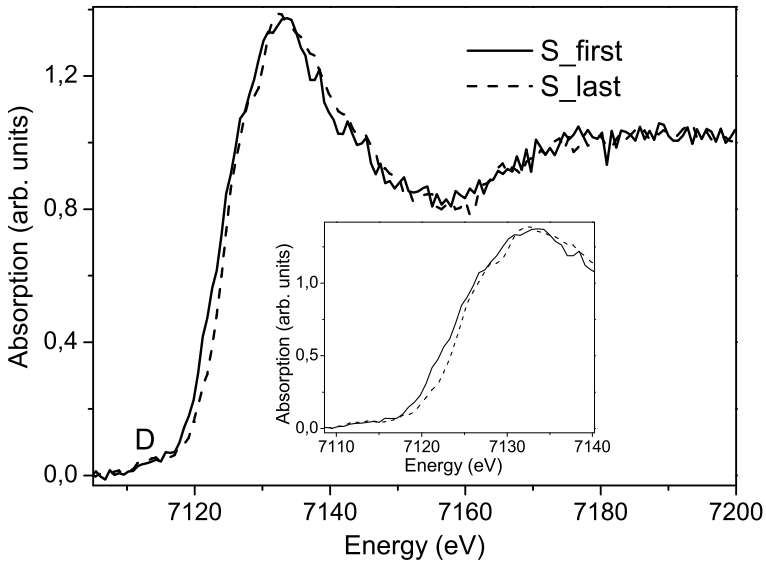

Figure 6.24: The first (S_first) and the last (S_last) Fe K-edge XANES experimental spectra recorded during the in situ thermo-electric oxidization of a LN:Fe 2wt% crystal.

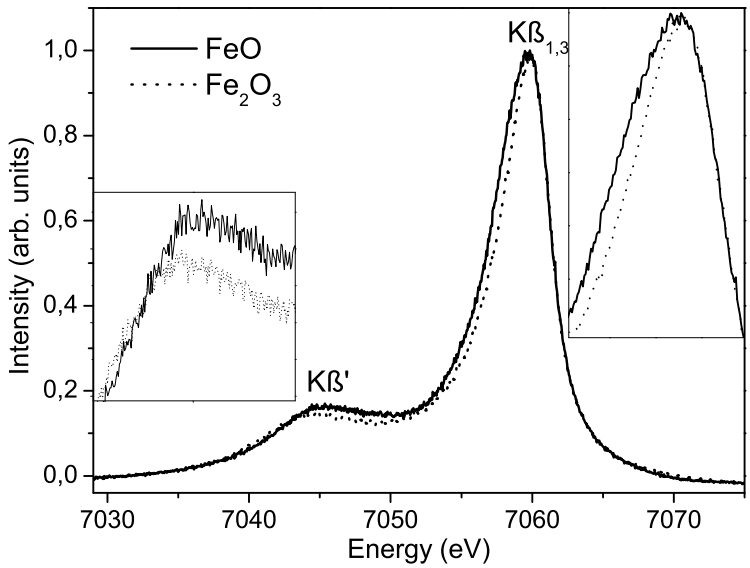

Figure 6.25: The HRXE spectra of the FeO and Fe_2O_3 reference compounds. The insets are enlargements of the Kβ' and Kβ lines.

in the LN:Fe 2wt% crystal investigated in our in situ experiment. In Figure 6.24, the XANES spectra, measured at the beginning (S_first) and at the end (S_ last) of the oxidation treatment are shown. A 0.5 eV energy shift of the S_last spectrum towards higher energies, compared to the S_first spectrum, was detected. The 0.5 eV energy shift is measured as the difference in energy positions of the first inflection points of the two spectra, which are defined as the maximum of the first derivative of the respective XANES spectrum. The change in color and the energy shift

of the spectrum towards higher energies indicate the successful oxidation of the crystal. However, the XANES spectrum does not show any other changes during the oxidation process, except this energy shift. Moreover, no significant differences were found in the measured EXAFS spectra. These findings suggest that both sites are most likely sixfold coordinated by oxygen atoms and that the Fe^{2+} and Fe^{3+} atoms occupy the Li site.

Despite the similarities in short and long range geometrical structures, the electronic structure of the Fe atoms in the two valance states differs. The resonance at the pre-edge region of the S_first and S_last spectra (see in Fig. 6.24 pre-edge region D) is assigned to the transition of the 1s electron to the lowest unoccupied states and it is expected to reflect electronic structural changes. However, the low signal-to-noise ratio and the restricted resolution of a conventional XANES measurement prevent detection of such differences. In order to overcome these limitations, partially site-selective XANES spectra were extracted from a high-resolution RIXS map employing the chemical sensitivity of the high-resolution Kβ emission lines of iron oxides with different oxidation states of iron.

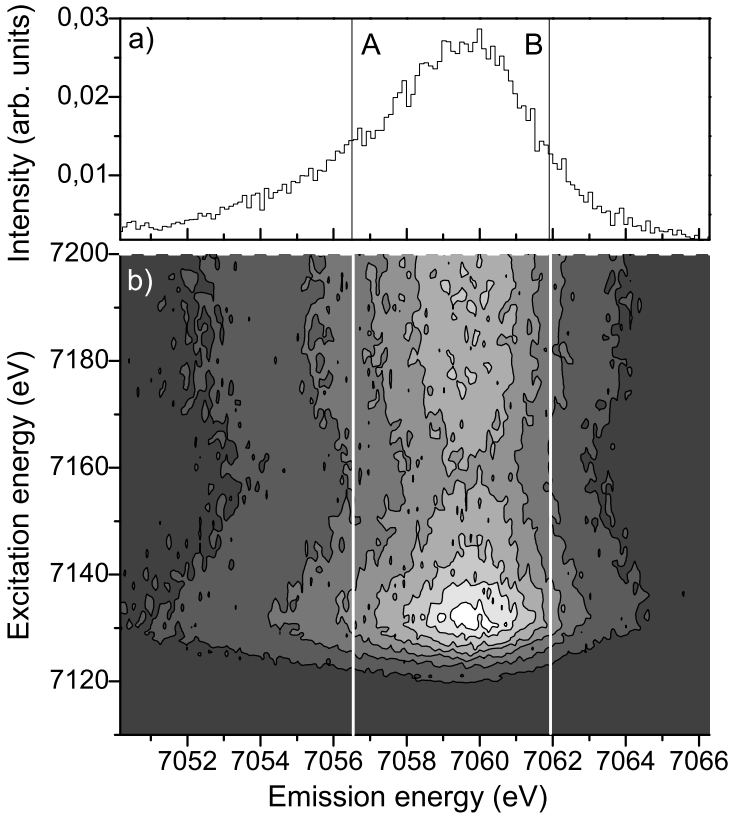

Figure 6.26: The K$\beta_{1,3}$ emission line a) and the 1s3p RIXS map b) of the LN:Fe 4wt% (C2) crystal.

HRXE spectra and RIXS map

The 1s3p non-resonant HRXE spectra of FeO and Fe_2O_3 are displayed in Figure 6.25. The Kβ line is split into a main intense emission line K$\beta_{1,3}$, which reflects 3p-1s spin down transitions and a satellite Kβ' on the low energy site, which reflects 3p-1s spin up transitions. The spin selectivity

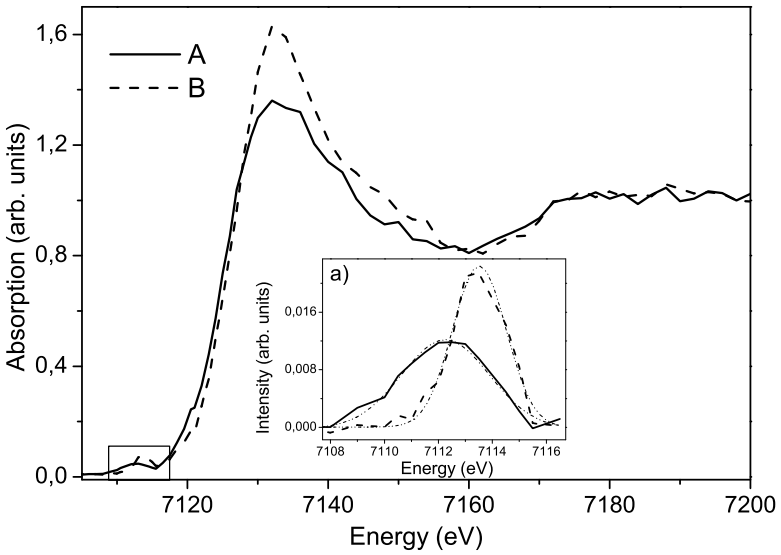

Figure 6.27: Site selective Fe K-edge XANES spectra A and B extracted from the RIXS map of the LN:Fe 4wt% crystal. The spectra A and B are obtained by integrating ± 1eV around the emission energies marked with A and B in Fig. 6.26 a), respectively. The background subtracted pre-edge resonances of the A and B spectra, their best fits and the Gauss profiles (dash dot dot) used as models are shown in the inset a).

of the Kβ emission line has been explained with the exchange interaction between the unpaired spin-up electrons in the 3d state and the hole created in the 3p state [64, 123] after transition of a 3p electron to the 1s state. Since the energy difference between the two emission lines, the width of the K$\beta_{1,3}$ line and the intensity of the Kβ' line depend on the number of spin-up electrons in the 3d state, the 1s3p HRXE spectra are sensitive to the oxidation state of iron (see Fig. 6.25). Using the chemical sensitivity of the 1s3p emission lines, Glatzel et al. measured site-selective EXAFS spectra of a mixed-valence compound Prussian blue, which contains Fe^{2+} and Fe^{3+} [66]. By following this approach, we tried to extract site-selective XANES spectra, called A and B, from the RIXS map of the C2 crystal by fixing the emission energy at the low and high energy sides at half maximum of the K$\beta_{1,3}$ emission line of the C2 crystal (see Fig. 6.26 and Fig. 6.27). Since the emission line of the Fe^{2+} reference (FeO) is wider than that of the Fe^{3+} (Fe_2O_3) reference (Fig. 6.25), mainly Fe^{2+} is expected to contribute to the A XANES spectrum. As the Fe^{2+} and Fe^{3+} emission lines overlap, it is not possible to extract "pure" site-selective spectra with the available energy resolution. The A and B XANES spectra are plotted in Figure 6.27. Despite the similarity of the two spectra, clear differences in the intensities and center of gravity of the two pre-edges are present (see the inset in Fig. 6.27). The two pre-edges are isolated by fitting a spline function and subtracting the remaining part of the spectra. The pre-edge resonances of the A and B spectra were modeled with Gauss profiles [see inset a) in Fig. 6.27]. The Gauss profiles are not assigned to any atomic transitions. The aim of the fit is determination of the center of gravity of the two structures. M. Wilke et al. has shown in his systematic study of iron oxides that the center of gravity of the pre-edge feature for Fe^{2+} and Fe^{3+} compounds differs by ≈1.4 eV [200]. This finding does obviously not depend on the site symmetry of iron. The difference in center of gravity of the pre-edges of the A and B spectra is ≈1.4 eV ± 0.1 eV. This result indicates that Fe^{2+} and Fe^{3+} dominantly contribute in the A and B spectra, respectively. The similarity of the shape of the White Lines (WL) and the

multiple scattering regions of the two spectra suggest that the short and long range geometrical structures of the two sites are similar. This finding agrees with the results obtained by the in situ XAS experiment. However, in this specific case the partially site-selective XANES spectra are more sensitive, demonstrating the difference in the electronic structure of the Fe^{2+} and Fe^{3+} sites.

6.3.5 Conclusion

Based on XANES, EXAFS, VIS absorption studies, in situ measurements of thermo-electric oxidization of a LN:Fe 2wt% crystal and HRXE spectroscopic studies, we come to the following conclusions:

1. The Fe atoms in the LN crystals doped with 2 and 4wt% iron are sixfold coordinated by oxygen atoms and occupy Li sites. Formation of iron oxide clusters (Fe-O-Fe coordination) was not found within the sensitivity of the EXAFS analyses.

2. It was possible to distinguish between the Fe^{2+} and Fe^{3+} sites and it was found that their site symmetries and positions in the LN matrix are very similar, i.e., the Fe^{2+} and Fe^{3+} atoms are in octahedral geometry surrounded by oxygen atoms and they both occupy the Li site.

6.4 Bond Valence Model (BVM)

The Cu, Mn and Fe trapping sites in LN can be predicted by the empirically derived Bond Valence Model (BVM) [28, 29]. This chapter will briefly describe this model and will compare the most probable Cu, Mn and Fe trapping sites with the ones obtained from the EXAFS analyses and published results from other methods.

In the Bond Valence Model (BVM), a crystal structure consists of anions and cations with numbers j and i, respectively [28, 29]. A bond valence s_{ij} is defined and its value is empirically derived:

$$s_{ij} = \exp\left(\frac{d_0 - d_{ij}}{B}\right). \tag{6.1}$$

B is equal to 0.36, whereas d_0 depends on the cation-anion pair [25, 28]. The distance between a cation and an anion is d_{ij}. According to the bond valence sum rule, the sum of bond valences around an atom i should be equal to its normal valence state (V_i)

$$\sum_j s_{ij} = V_i. \tag{6.2}$$

The absolute value of the difference between the normal valence and the bond valence sum is denoted as d_i in valence unites (v.u.)

$$d_i = \left| V_i - \sum_j s_{ij} \right|. \tag{6.3}$$

d_i value larger than zero indicates a strained bond. However, the structure still can exist as far as the Global Instability Index (GII) is less than 0.2 v.u. The GII is defined as

$$GII = \sqrt{\sum_{i=1}^{N} d_i^2 / N}, \tag{6.4}$$

where N is the number of cations in the structure.

A perfect periodic crystal structure might impose constrains (non-local steric effects), as it requires that all parts of a structure be commensurate. If the non-local steric effects lead to too large strains, the symmetry may be lowered or the structure may become incommensurate. The interplay between an ideal bond geometry and a stable periodic structure is regulated by the bond strength. A strained structure can not exist for strong bonds. Strains are possible for bonds with intermediate or weak strength but only for GII less than about 0.2 v.u. [25, 28]. Otherwise, the stress is reduced by changes in the structure, e.g., structure with lower symmetry, unusual oxidation states. A steric strain imposed on a crystal structure often leads to interesting physical properties like ferroelectricity and superconductivity [29].

The d_i values for the studied cations, assuming Li sites ($d_i^{Li\text{–}site}$) or Nb sites ($d_i^{Li\text{–}site}$) occupation, are given in Table 6.8. The d_0 values are derived by studying hundreds of inorganic crystal structures stable at room temperature [25, 28]. The used d_{ij} bond lengths are: short Li-O: 2.052 Å, long Li-O: 2.260 Å, short Nb-O: 1.878 Å and long Nb-O: 2.126 Å (ICSD 28294). The preferred occupation

sites are summarized in Table 6.8. The selection is done considering that a smaller d_i value leads to less strained bond and hence to more stable structure. In case of Cu^{1+}, Cu^{2+}, Fe^{2+} and Mn^{2+}, sixfold coordinated by O atoms, the BVM predicts incorporation into Li sites. However, twofold coordinated Cu^{1+} and sixfold coordinated Fe^{3+}, Mn^{3+} and Mn^{4+} have smaller $d_i^{Nb\_site}$ values, i.e., Nb sites are preferred. The BVM partially contradicts our EXAFS results, since it predicts Fe^{3+} ions in Nb sites at low concentrations. Xue et al. have explained this discrepancy by considering the non-stoichiometry of congruently-melting LN and the presence of Nb atoms in Li sites (Nb_{Li}) with a d_i value of 1.783. It is supposed that ions with d_i value smaller than 1.783, regardless of the relative value of $d_i^{Li\_site}$ to $d_i^{Nb\_site}$, can occupy Li or Nb sites.

In this study, twofold coordinated Cu^{1+} ions are detected in LN crystals for the first time. The calculated d_i value (0.33), considering the Cu-O distance from the EXAFS analysis, indicates strained bond and an unstable structure (see Table 6.8). Since Cu^{1+}-O forms a weak bond, it is likely that the stress in the structure is reduced by distorting the local symmetry, i.e., a short and a long Cu^{1+}-O distances. The present resolution does not allow to resolve a distortion. In addition, sixfold coordinated Cu^{2+} ions still exist in the reduced samples and their consideration might lead to a lower GII value. Except for Fe^{2+}, all other d_i values calculated on the basis of the obtained Me-O distances and assuming perfect local symmetry are larger than 0.2 v.u. suggesting unstable crystal structure (see Table 6.8). The actual structural relaxation could not be precisely detected with the present resolution. However, difference in the Me-Nb distances is found for the studied ions (Tables 6.3, 6.5 and 6.7), compared to the Cu_on_Li/Nb_site models. This implies long range structural changes induced by introducing ions into the LN crystal.

Some type of ions begin to occupy Nb sites after a certain threshold concentration or co-doping with other ions. For example, Xue et al. have found that the threshold for Fe^{3+} is 2.02 mol%, whereas it is 5.03 mol% for Mn^{2+} [203]. Samples with doping concentrations over these thresholds are not studied here. Please notice, that the absolute concentration of Fe in the 4 wt% iron-doped LN crystal is about 2 wt%

The Cu (≈1.8) and Fe (≈2.8) average formal oxidation states does not depend on their concentrations, within the studied concentration ranges, in indiffused copper- and as-grown iron-doped LN crystals. Congruently-melting LN crystals have intrinsic defects, whose amount and type are influenced strongly by the growing conditions. It is likely that different LN compositions cause formation of different average dopant formal oxidation states. This can be verified by comparing the average formal oxidation states of metals doped in LN crystals grown by different producers.

FOS (coord.)	d_0 (Å)	$d_i^{Li-site}$ (v.u.)	$d_i^{Nb-site}$ (v.u.)	BVM	EXAFS	experimental studies	theoretical studies	d_i (v.u.)	dis. Å
Cu^{1+} (2O)	1.593	0.55	0.30	Nb	Li			0.33	2.00
Cu^{1+} (6O)	1.593	0.36	1.09	Li	Li	Li [120]		1.00	2.00
Cu^{2+} (6O)	1.679	0.29	0.63	Li	Li	Li [34]		0.52	2.00
Fe^{2+} (6O)	1.734	0.02	1.05	Li	Li	Li [70] (XSW), [134] (XANES)	Li [50], Nb [11]	0.92	2.00
Fe^{3+} (6O)	1.759	0.88	0.27	Nb	Li	Li [70] (XSW), [134] (XANES), [179] (ENDOR)	Nb [218], Li [50]	0.13	2.00
Mn^{2+} (6O)	1.790	0.31	1.55	Li	Li/Nb	Li [39] (ENDOR), [119] (EPR), [212] (EXAFS)	Li [50], Li and Nb [11]	0.67	2.09
Mn^{3+} (6O)	1.760	0.87	0.28	Nb	Li/Nb		Li [50]	0.54	2.09
Mn^{4+} (6O)	1.753	1.91	0.79	Nb	Li/Nb			1.59	2.09

Table 6.8: The Formal Oxidation State (FOS) of the studied ions and their coordination to O atoms (in brackets) are given in the first column. The d_0 values in v.u. (from [25, 28]) are in the second column. The $d_i^{Li-site}$ and $d_i^{Nb-site}$ values in v.u. are given in the third and fourth columns. The dopants occupation site according to the BVM and EXAFS are in the fifth and sixth columns, respectively. The dopants occupation site from other experimental and theoretical studies are in the seventh and eight columns, respectively. The d_i values in v.u. calculated with the d_{ij} values from the tenth column are in the ninth column. d_{ij} Me-O distances in Å obtained from the EXAFS analysis are in the tenth column.

Chapter 7

Lithium niobate irradiated with $^3He^{2+}$ ions

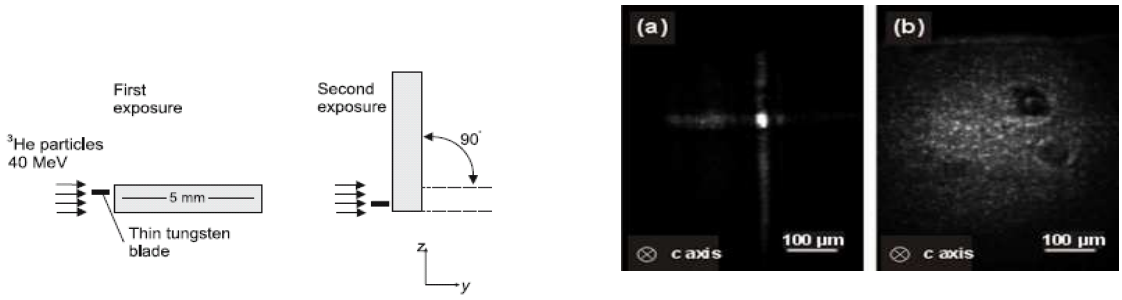

Figure 7.1: The two-steps irradiation process (left) creates a channel in the LN crystal. When laser light is coupled into the channel, the light is guided (right, (*a*)), because of the lower refractive index around the channel. The picture on the right (*b*) shows the transmitted intensity, when the laser is coupled to the crystal outside of the channel. (from [143])

7.1 Introduction

Lithium Niobate (LN, $LiNbO_3$) is an important non-linear optical material and is also widely applied as waveguides [7]. Waveguides are fabricated by indiffusing or implanting LN crystals with metal ions, e.g., Ti [97, 164], or irradiating them with low-energy ions, e.g., O, F or He [47]. The surface of the crystal is used as a wall for the waveguide. The second wall is the thin layer of damaged material, where the ions are stopped (Bragg peak). It has been observed that the refractive index slightly changes (Δn) in the region between the surface and the Bragg peak, when low-energy, low-mass ions pass through the material [36, 69, 215]. The extraordinary refractive index (n_e) of LN is enhanced, whereas its ordinary refractive index (n_o) is reduced. Hence the birefringence (n_o-n_e) of LN is diminished. Peithmann et al. strengthened this effect, by irraditing LN crystals with high-energy $^3He^{2+}$ ions (41 MeV), and demonstrated its use for fabrication of a novel type of polarization-selective embedded waveguide [143] (see Fig. 7.1). The diminished birefringence was explained from SRIM-2003 [219] simulations showing the loss of the axis of anisotropy, caused by Li, O and Nb

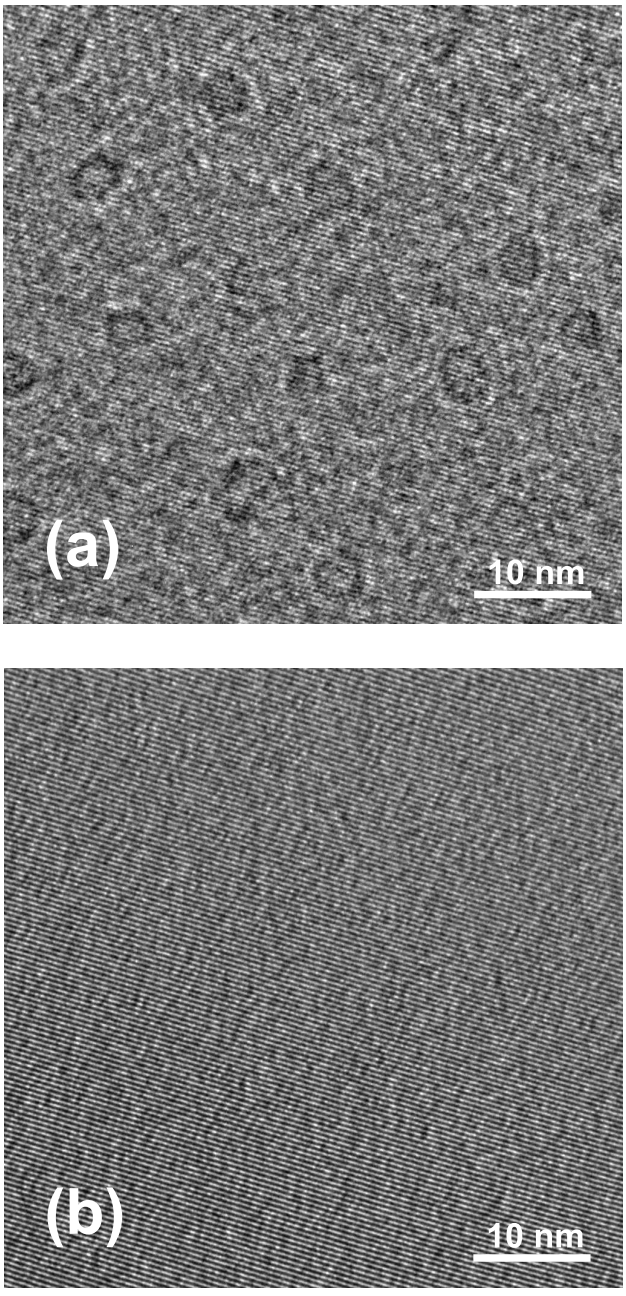

Figure 7.2: TEM images of LN crystals. The upper image (a) shows a crystal which has been exposed by $^{3}He^{2+}$ ions whereas the lower image (b) shows a non-irradiated crystal. (from [213])

lattice vacancies [142]. The effect is reversible, i.e., the Δn is reduced at about 100°C and disappears completely at about 500°C. It is known that Li atoms diffuse in a LN crystal in the temperature interval 100-200°C [130], whereas O and Nb atoms become mobile at higher temperatures [19]. It is assumed that with increasing temperature Li, Nb and O atoms diffuse to there initial positions in the crystal matrix, restoring the axis of anisotropy, i.e., the birefringence of the LN crystal [142]. These results are supported by TEM measurements [213]. Structurally disordered circular centers with about 4 nm diameter are visible on the TEM image of an irradiated LN crystal (see Fig. 7.2).

XAFS spectroscopy is a suitable tool for studying local structural and electronic changes around an element of interest in a compound. However, to reveal the structural changes causing Δn is a challenging task for XAFS spectroscopy. An exact probe of the irradiated spot with 1 mm^2 size is necessary. Moreover, significant damage should be present in order to be detected within the sensitivity of the method.

The goal of the this XAFS study is to probe the local environment of the Nb atoms in order to verify the induced structural damage, i.e., Li, Nb and O lattice vacancies [142]. For this purpose a single irradiated LN crystal with 40 μm thickness is studied. Nb K-edge XAFS spectra, measured inside and outside of the irradiated spot, are compared. The XANES spectra are interpreted by performing simulations of Nb K-edge XANES spectra with the FEFF8.2 code [10].

7.2 Preparation of the samples

A commercially available x-cut $LiNbO_3$ crystal was cut into 0.5x10x10 mm^3 pieces, polished and irradiated with $^3He^{2+}$ ions with energy 41 MeV, at the isochron cyclotron of the Helmholtz-Insitute for Radiation and Nuclear Physics, University of Bonn. The relaxation process of the activated Nb is as follows: 1) $^{93}Nb(^3He,^4He)^{92}Nb$; 2) ^{92}Nb does an electron capture and transforms into ^{92}Zr, the half-life is 10 days; 3) ^{92}Zr relaxes by emitting a gamma particle, energy 934 keV.

The thickness of one of the irradiated crystals was reduced to 40 μm after irradiation. The Bragg peak was removed from the crystal.

7.3 Experiment, methods and data evaluation

XAS experiments were performed at the INE-Beamline at ANKA. For energy monochromatization a set of Ge(422) crystals was used.

The XAFS (XANES + EXAFS) spectra were recorded in transmission mode using Argon filled ionization chambers. The Nb K edge-XANES spectra were measured in the energy interval from 18930 eV to 19140 eV with 1.7 or 0.6 eV step width and 1s integration time. For energy calibration, photon energy of 18986 eV was set to the first inflection point of the K-edge spectrum of a niobium foil, simultaneously measured with the crystal. The data reduction of the Nb K-edge XANES spectra consisted of subtraction of a linear background fit to the pre-edge region from 18936 eV to 18970 eV and normalization of the spectra to an edge jump of one at 19125 eV.

The ARTEMIS [151] program package was used for the EXAFS analysis. The χ(k) Nb K-edge signal caring a k range from 3.6 to 13 $Å^{-1}$ was Fourier-transformed to R space using a k weighting of 1,2 and 3 and a Kaiser-Bessel Window with window sills dk equal to 4. The fit was performed in R space over a range from 1 to 2 Å. For the initial model the structure of $LiNbO_3$ (ICSD 28294) was

used. The amplitude reduction factor (S_0^2) was fixed to 1 during the fit of the He:$LiNbO_3$ spectrum. This value was obtained by fixing the coordination numbers and varying S_0^2 during the fit of the $LiNbO_3$ FT-EXAFS spectrum.

In the FEFF8.2 [10] calculations the EXCHANGE, SCF, FMS and XANES cards were used. The Hedin-Lundqvist self-energy was chosen as exchange correlation potential, which is the default setting of the EXCHANGE card. The calculations were done for a cluster of 200 atoms around Nb.

7.4 Results and discussion

7.4.1 XANES analysis

Figure 7.3 displays the absorption of the irradiated crystal with ≈40 μm thickness at 19 keV as a function of the beam position. The different areas present spots from the sample with ± 0.09 difference in absorption. The variations in absorption of a single LN crystal give the opportunity to study the influence of thickness effects on Nb K-edge XANES spectra of LN. The spectra measured with 1.7 eV energy step at positions from the sample marked with spot_1, spot_2 and spot_3 in Figure 7.3 are plotted in Figure 7.4 *A*. The three spectra are the same, which suggests that thickness differences in this order do not alter the XANES spectrum. These measurements were repeated with a 0.6 eV energy step; the spectra are shown in Figure 7.4 *B*. Nb K-edge XANES spectra, measured at spot_2 with 1.7 eV or 0.6 eV energy step, are compared in Figure 7.4 *C*. Evidently, the two spectra are identical in the pre-edge regions, denoted with *a*, whereas amplitude differences are visible in the WL regions, i.e., the *b* and *c* resonances of the spot_2 (0.6 eV) spectrum have higher intensity than the respective of the spot_2 (1.7 eV) spectrum. This deviation demonstrates the importance of measurements with equal step size.

Nb K-edge XANES spectra measured at the irradiated and outside of the irradiated spot with 0.6 eV energy step are compared in Figures 7.4 *D* and 7.5. The differences in the WL region of the two spectra are too small to be considered significant (see Fig. 7.5 *b* and *c*). However, the increased intensity of the pre-edge shoulder of the He:$LiNbO_3$ spectrum is reproducible and significant and certainly reflects structural changes occurring during the irradiation process (see Fig. 7.5 *a*).

FEFF8.2 calculations based on two different models were carried out in order to explain the origin of the differences in the Nb K-edge XANES spectrum measured within the irradiated and outside the irradiated spot. The first model is motivated by literature study [168], which reports changes affected in *a* (see Fig. 7.5), i.e., an increased intensity of the pre-edge resonance, and correlates this, in the case of octahedrally-coordinated transition metal oxides, with displacement of the absorber atom from the center of the octahedron. Figures 7.6 and 7.7 show selected calculated spectra obtained with atomic clusters with a systematic variation of atomic coordinates, i.e., the Nb atoms are shifted 0.01, 0.02 or 0.03 Å along the z axis, in negative (Fig. 7.6) or positive (Fig. 7.7) direction. The same calculations were performed by shifting the Nb atoms along the positive x and y and negative x and y axis. For most simulations, the amplitude of the pre-edge shoulder raises with the absolute size of the shift. This change in oscillatory strength is accompanied by changes in features *b* and *c* in the WL region (see Fig. 7.5).

The second model investigated in these theoretical calculations includes the presence of Li and O vacancies in the structure. The vacancies are simulated by random removal of O and Li atoms/O atoms from the list of atomic coordinates. The Nb K-edge XANES spectrum converges after averaging around 15 calculated spectra. Figures 7.8 shows calculated spectra with Li and O vacancies.

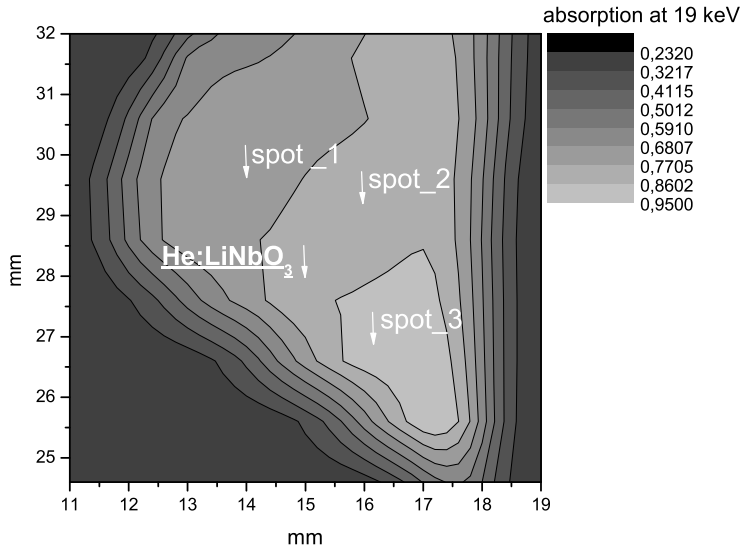

Figure 7.3: Absorption map of the irradiated single $LiNbO_3$ crystal with thickness 40 μm. The XAS measurements are done at the irradited spot, denoted with He:$LiNbO_3$, and at three spots, where the crystal is unexposed, denoted with spot_1, spot_2 and spot_3.

	$LiNbO_3$			He:$LiNbO_3$		
	R(Å)	N	σ^2 (Å^2)	R(Å)	N	σ^2 (Å^2)
O1	1.89 ± 0.01	3.6 ± 0.5	0.004 ± 0.001	1.88 ± 0.02	4 ± 1.2	0.005 ± 0.001
O2	2.13 ± 0.01	3.2 ± 0.5	0.004 ± 0.001	2.12 ± 0.01	2.6 ± 1.1	0.005 ± 0.001

Table 7.1: The results from the analyses of the $LiNbO_3$ and He:$LiNbO_3$ EXAFS spectra. The structural parameters are named as follow: N: coordination numbers, R (Å): distances and σ^2 (Å^2): Debye-Waller factors.

.

An increase in the pre-edge resonance and a distribution of intensities of the resonances b and c in the WL region are visible. The calculated spectra with O vacancies are not shown here.

The amplitude of the pre-edge shoulder decreases only in the case of the simulations shown in Figure 7.6. It is an expected effect, as the Nb atoms move towards the centrosymmetric position in the oxygen-octahedron in this calculation. The pre-edge shoulder increases in the remaining simulated XANES spectra. These findings indicate that XANES can not distinguish between these two models; hence they are both likely.

7.4.2 EXAFS analysis

Additional insights into the structural changes are provided by an EXAFS analysis. Figures 7.9 *A* and *B* show the FT-EXAFS (χ(R)) spectra measured at the irradiated spot and at spot_2 on the sample. The first coordination shell of the He:$LiNbO_3$ spectrum was fit with: 4 ± 1.2 O atoms at 1.88 ± 0.02 Å and 2.6 ± 1.1 O atoms at 2.12 ± 0.01 Å . The obtained structural parameters from the spectrum measured at spot_2 are 3.6 ± 0.5 O atoms at 1.89 ± 0.01 Å and 3.2 ± 0.5 O atoms at 2.13 ± 0.01 Å. Evidently, the best fit-values for the first coordination shell of the irradiated LN

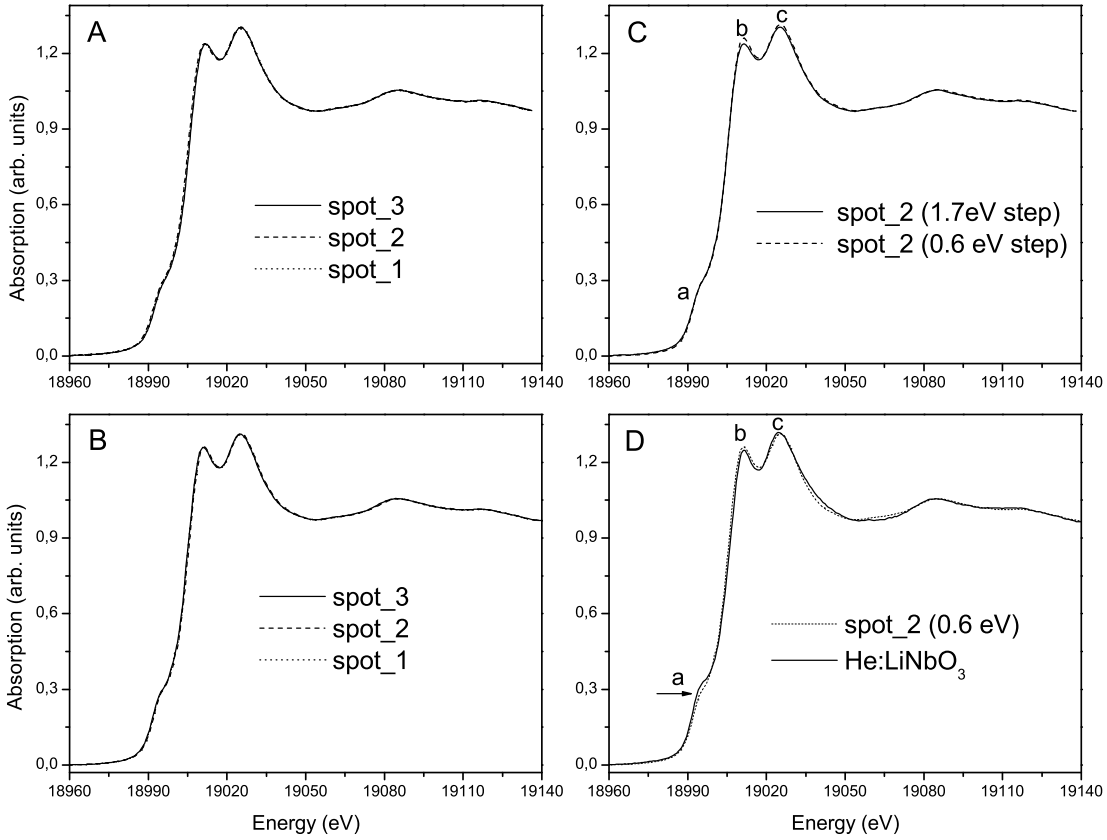

Figure 7.4: Nb K-edge XANES spectra of a single crystal $LiNbO_3$ measured at different spots from the sample with 1.7 eV (A) or 0.6 eV (B) energy steps. Nb K-edge XANES spectra measured at spot_2 from the LN crystal with 1.7 eV or 0.6 eV energy steps (C). Nb K-edge XANES spectra measured in and out of the irradiated spot (D) (see Fig. 7.3).

crystal do not support the distorted-octahedron-model (see Table 7.1). The obtained coordination numbers also exclude any major contribution of O vacancies. Nb vacancies do not dominate as well, as the amplitude of the peak corresponding to the Nb - Nb single scattering path remains the same after irradiation (see Fig. 7.9 *C*). However, changes are present at the vicinity of the second coordination shell, where the Nb-Li single scattering paths contribute (see the circled area in Figure 7.9 *C*). This finding indicates that the applied irradiation has damaged the LN matrix by creating lithium vacancies and/or redistributing of Li atoms.

7.5 Conclusion

The performed simulations of Nb K-edge XANES spectra indicate that the structural disorder caused by displacement of Nb atoms as well as Li and O vacancies can explain the modification in the XANES spectra. Within the sensitivity of the method, the FT-EXAFS spectra support the Li vacancies hypothesis.

The XAFS analyses corroborate results in [142] that the presence of disorder in the geometrical

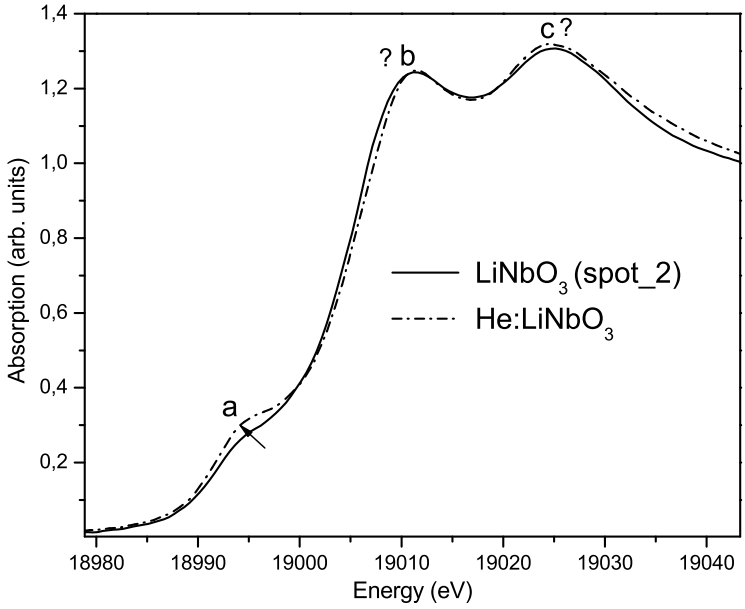

Figure 7.5: Nb K-edge XANES spectra measured in and outside of the irradiated spot (see Fig. 7.3).

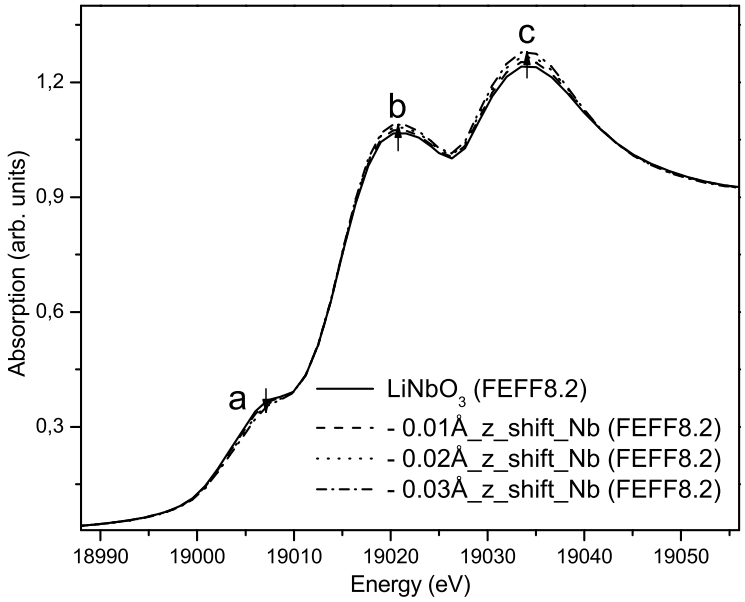

Figure 7.6: Nb K-edge XANES spectra of $LiNbO_3$ calculated with the FEFF8.2 code. A modified list of atomic coordinates with the Nb atoms shifted 0.01, 0.02 or 0.03 Å along z axis in a negative direction is used in the calculation.

structure of irradiated LN [213], leads to changes in the refractive index and causes decrease of the birefringence of LN.

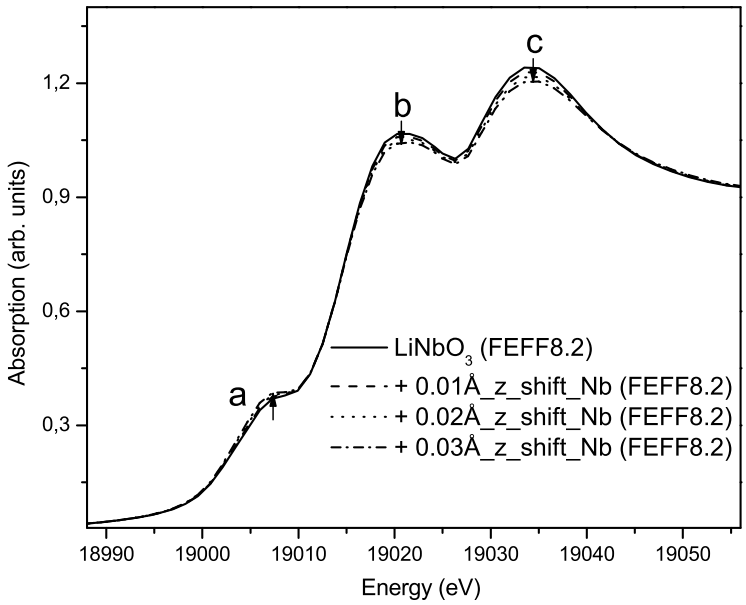

Figure 7.7: Nb K-edge XANES spectra of a $LiNbO_3$ calculated with the FEFF8.2 code. A modified list of atomic coordinates with the Nb atoms shifted 0.01, 0.02 or 0.03 Å along z axis in a positive direction is used in the calculation.

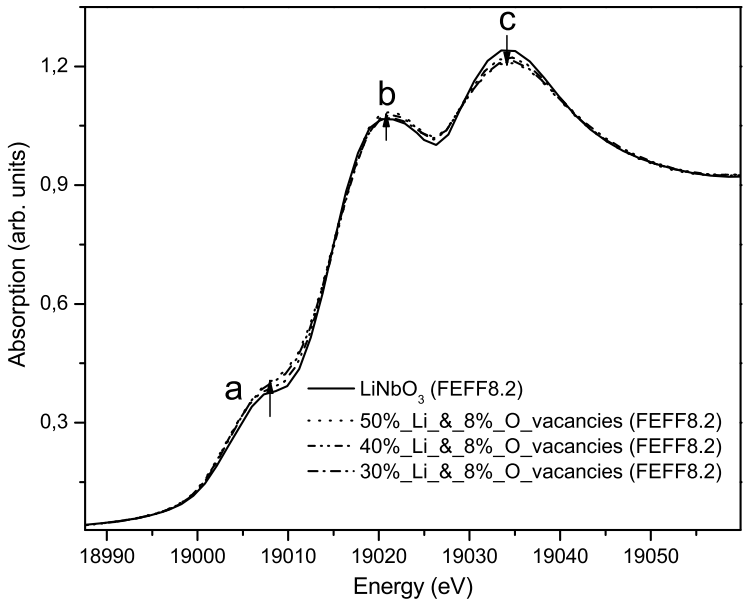

Figure 7.8: Nb K-edge XANES spectra of $LiNbO_3$ and $LiNbO_3$ with simulated Li and O vacancies calculated with the FEFF8.2 code.

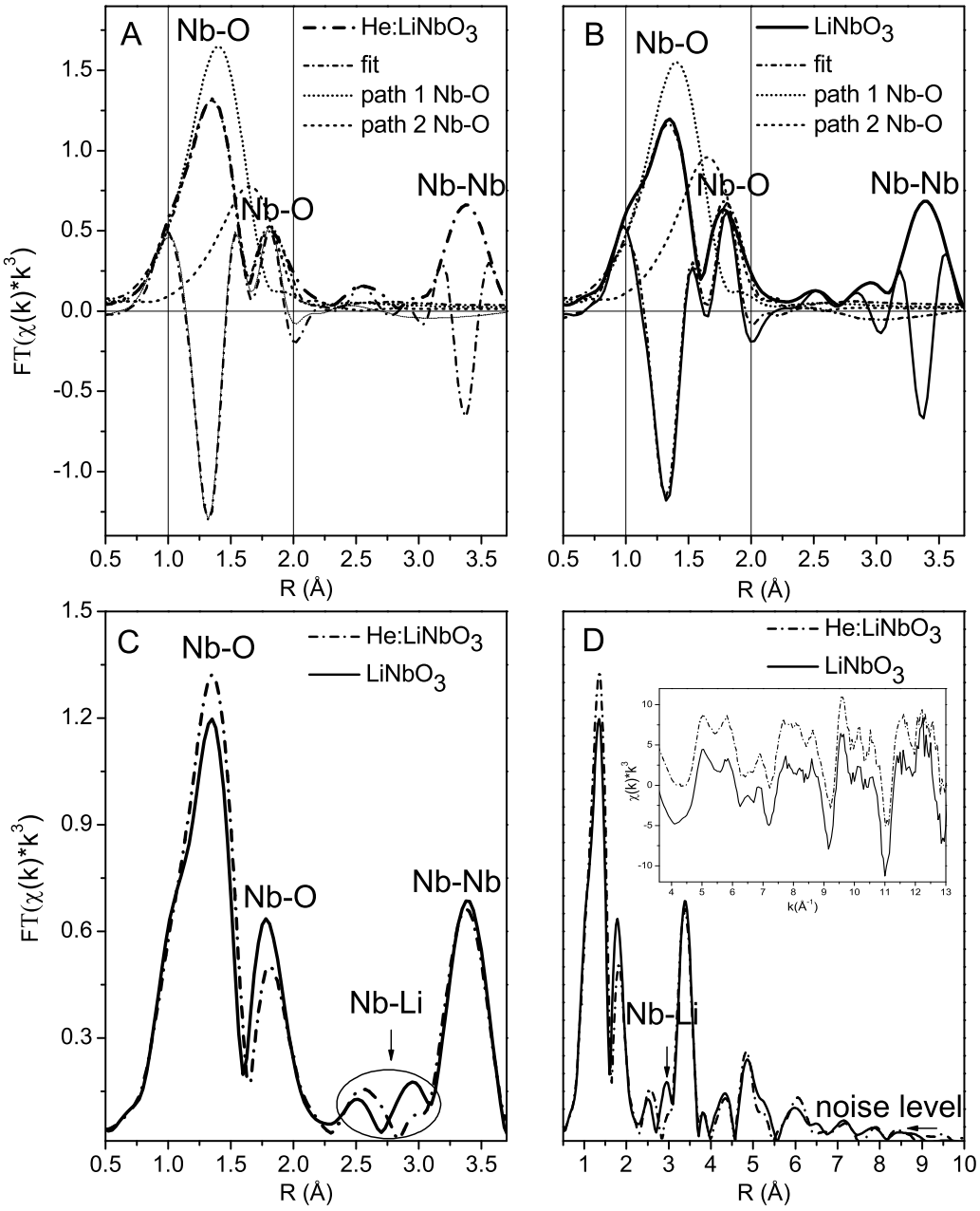

Figure 7.9: EXAFS spectra in R space of $LiNbO_3$ (A) and He:$LiNbO_3$ (B) the best fits of the first coordination shells and the Nb-O single scattering paths used in the fits. The EXAFS spectra in R space of $LiNbO_3$ and He:$LiNbO_3$ until 4 Å (C) and 10 Å (D).

Chapter 8

Summary and outlook

LN crystals doped with various concentrations of Cu (0.1-0.7 wt%), Mn (0.05-1 wt%) or Fe (2 and 4 wt%) as prepared, reduced and oxidized state and LN crystals irradiated with high-energy $^{3}He^{2+}$ ions were studied with XAS, UV/VIS/IR and HXES. These investigations were carried out with DFG research group "Light confinement and control with structured dielectrics and metals". The main results are summarized as follows:

Copper-doped LN crystals:

(1) The average formal oxidation state of Cu in all studied samples is between Cu^{1+} and Cu^{2+} (Table 6.2).

(2) It was found that the average formal valency of Cu does not notably depend on the Cu concentration (for the range 0.1-0.3 wt% of Cu) upon simultaneous diffusion and oxidation of the doped crystals. However, it does depend on the Cu concentration upon reduction of the doped crystals.

(3) Strong experimental evidence were found that the Cu atoms occupy dominantly Li sites for all samples. It was possible to distinguish between Cu^{1+} and Cu^{2+} sites: (i) the Cu^{2+} atoms are sixfold coordinated by O atoms in the LN crystals having a formal Cu valence equal to or higher than 1.7 ± 0.2 (ii) Cu^{1+} atoms are twofold coordinated and Cu^{2+} sixfold coordinated by O atoms in the LN crystals having formal Cu valency equal to or lower than 1.5 ± 0.2.

(4) Upon reduction of the doped LN crystals, one of the charge compensation mechanisms is outgassing of O atoms.

(5) No experimental evidence for metal copper or copper oxide cluster formation in the LN matrix was found, even for the highly doped LN crystals (0.3-0.7 wt% of Cu).

(6) Change in the formal oxidation state of the Nb atoms upon reduction of the crystals is necessary for charge compensation, but was not detected by the XAS measurements at the Nb LIII-edge due to the expected change being lower than the energy resolution.

Manganese-doped LN crystals:

(1) Mn atoms are incorporated both into Li and Nb sites in the C5AG, C5RE, and C5OX crystals, where these two sites are not neighboring. It is unlikely that selection of the Nb trapping site is induced by high Mn concentrations. The Bond Valence Model (BVM) predicts that Mn atoms with formal oxidation state higher than 2+ preferably occupy Nb sites. Indications for a small amount of MnO clusters were also found.

(2) The thermo-electric oxidization method led to oxidation of Mn^{2+} to Mn^{3+} (from 2.8 ± 0.2 to 2.9 ± 0.2). The reduction treatment caused full elimination of the Mn^{3+} site, leading to lower average Mn formal oxidation state (from 2.8 ± 0.2 to 2.6 ± 0.2). The higher than 2+ average formal oxidation state of the reduced crystal is possibly due to presence of two different Mn^{2+} sites (Li and Nb) with significantly different XANES spectra. Direct evidence for presence of Mn valency higher than 3+ was not found in the C5AG, C5RE, and C5OX crystals.

(3) The average formal oxidation state of Mn in the LN:Mn crystals with various doping levels of Mn (0.01-1 wt% Mn) is between 2+ and 3+. The deviation from a linear relation between average formal oxidation state and concentration, and from one average formal oxidation state might be due to existence of Mn valency higher than 3+.

Iron-doped LN crystals:

(1) The Fe atoms in the LN crystals doped with 2 and 4wt% iron are sixfold coordinated by oxygen atoms and occupy Li sites. Formation of iron oxide clusters (Fe-O-Fe coordination) was not found within the sensitivity of the EXAFS analyses.

(2) It was possible to distinguish between the Fe^{2+} and Fe^{3+} sites and it was found that their site symmetries and positions in the LN matrix are very similar, i.e., the Fe^{2+} and Fe^{3+} atoms are in octahedral geometry surrounded by oxygen atoms and they both occupy the Li site.

LN crystals irradiated with $^{3}He^{2+}$ ions:

The performed simulations of Nb K-edge XANES spectra indicate that the structural disorder caused by displacement of Nb atoms as well as Li and O vacancies can explain the modification in the XANES spectra. Within the sensitivity of the method, the FT-EXAFS spectra support the Li vacancies hypothesis.

The XAFS analyses corroborate results in [142] that the presence of disorder in the geometrical structure of irradiated LN [213], leads to changes in the refractive index and causes decrease of the birefringence of LN.

According to the EXAFS results, Cu and Fe atoms are only trapped into Li sites, whereas Mn atoms occupy Li and Nb sites. BVM predicts that Mn atoms with Formal Oxidation State (FOS) higher than 2+ are incorporated into Nb sites (see Table 6.6). The Cu, Mn and Fe atoms are sixfold coordinated by O atoms in as-grown/indiffused and oxidized state. However, the Metal-O (Me-O) distances differ from the Li_site_model. The coordination is changed from 6 to 2 O for Cu^{1+} in the reduced LN:Cu crystals, whereas no changes are found in the reduced LN:Mn 1 wt% crystal. Indication of metal oxide clusters (Me-O-Me coordination) are present only for the LN:Mn crystals. The high dopant concentration leads to decrease of the distance between the impurity centers. This causes change in LN lattice parameters, for example, the Fe-Nb distance increases from 3.05 to 3.14 Å for LN:Fe 2 and 4 wt%, respectively. The doped atoms are highly site-selective in the concentration range studied. No evidence for change in incorporation site induced by high concentration is found.

The amount and type of donors and traps, i.e., impurity centers with different oxidation states, is crucial for tuning the optical properties of doped or pure LN crystals. Impurities in two formal oxidation states are found for Cu and Fe and their ratio is rather independent of their concentration in the indiffused/as-grown state, within the concentration range studied. This is not the case for manganese-doped LN crystals, where three different Mn valencies are present; the Mn Average Formal Oxidation State (AFOS) differs in the various LN:Mn crystals and is not correlated with the

Mn concentration. BVM indicates that the stoichiometry of LN, i.e., type and amount of intrinsic defects, have direct influence on the formed dopant valency. This could be verified by studying copper and iron doped crystals from different suppliers. An alternative way to regulate the amount of traps and donors, in order to obtain specific optical properties, is to apply additional treatments i.e., reduction or oxidation. However, the reduction treatment can lead to dramatic change in site-symmetry, for example from sixfold to twofold coordinated Cu^{1+}, which also influence the LN matrix geometry, e.g., changes Cu-Nb distances. As a result, the LN anisotropy axis is lost and the LN birefringence can diminish. No evidence for concentration dependence of the AFOS is found for the covered concentration range. Reproducibility of optical properties, e.g, exact AFOS, is crucial in a serial production. Therefore, understanding and controlling the charge compensation mechanisms upon reduction or oxidation of doped LN crystals is important. The clear evidence that O atoms outgass during reduction process leads to the question: is there a reduction method, which leads to charge compensation only by reducing Nb atoms?

The obtained electronic and geometric structural properties of the modified LN crystals demonstrate the valuable structural characterization resources of the XAS technique. The HRXES confirmed to be an advanced method, which allows to distinguish between atoms in different valence states with similar local geometric structure.

A more detailed understanding of the local structure of modified LN crystals and its correlation with specific optical properties requires additional studies. The charge compensation mechanisms during reduction or oxidation of Cu, Mn and Fe:LN crystals can be better understood by for example, in situ mass spectrometric and XAFS measurements. Such studies can confirm and complement the already obtained results. The refractive index change stops to increase at different concentrations for the three dopants. Simultaneous laser illumination and XAFS measurements at the same spot of a doped LN crystal might help to understand the origin of these differences. HRXES studies with an improved experimental energy resolution (less than 1 eV) will allow to resolve electronic transitions in the XANES pre-edge region and thus to distinguish between the electronic structures of different sites. XAFS studies of LN crystals doped with higher than 1wt% copper and copper added into the LN melt, i.e., as-grown LN:Cu, will give answers to questions like do the Cu atoms change their incorporation site at high concentrations and does the preparation method influence the Cu trapping site. No XAFS studies so far has been done on doubly doped LN crystals, e.g., Fe and Mn. Such investigations are desirable, in order to compare the local structures around Mn and Fe with the respective of a single dopant.

Appendix A

The studied LN cluster and graphical comparison of the Cu, Mn and Fe EXAFS results

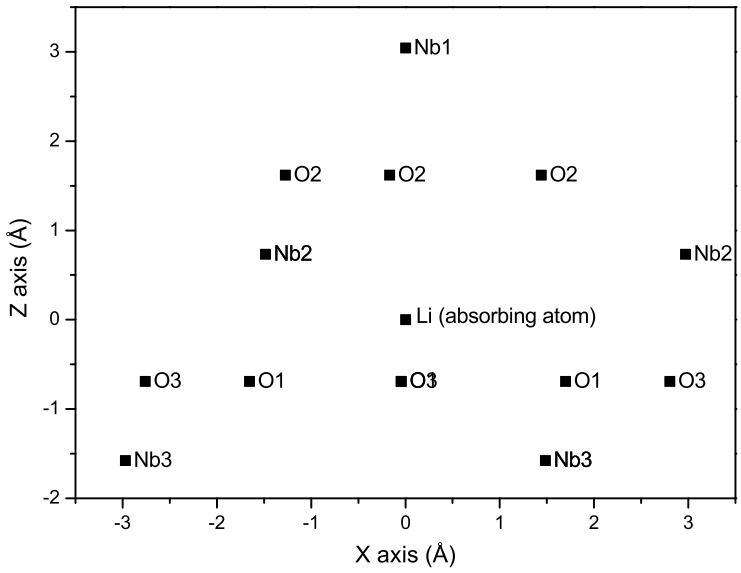

Figure A.1: The studied LN cluster with EXAFS analysis. Li is assumed as central absorbing atom.

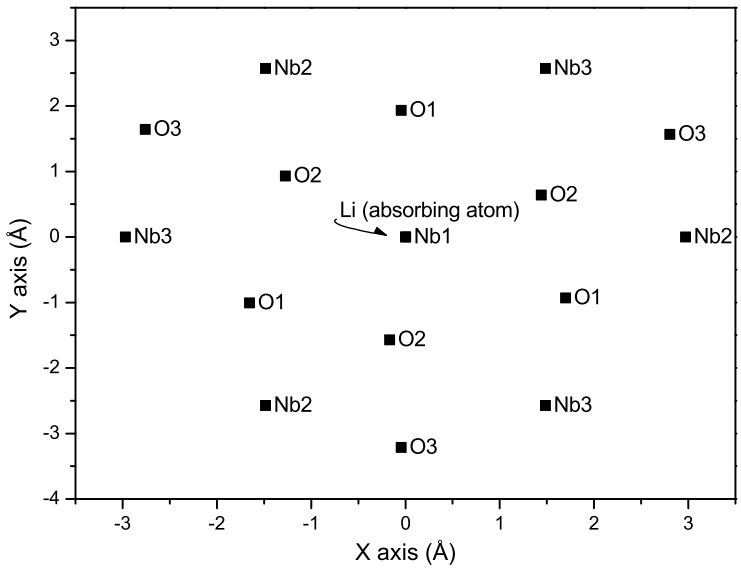

Figure A.2: The studied LN cluster with EXAFS analysis. Li is assumed as central absorbing atom and is located behind the Nb1 atom.

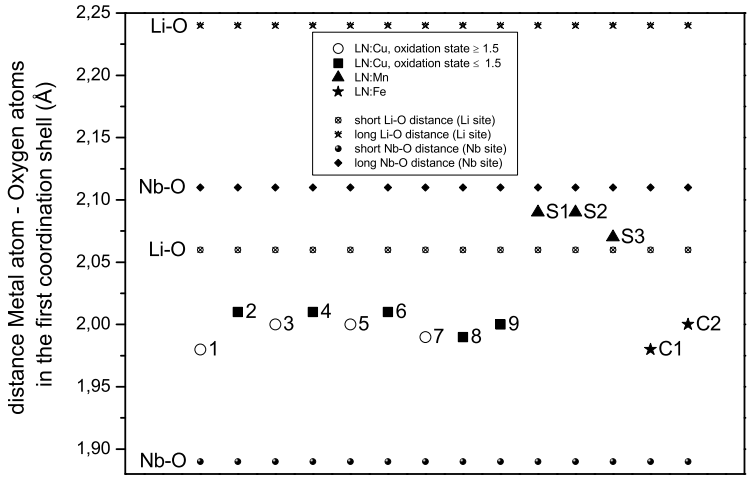

Figure A.3: Distances Metal-O in the first coordination shell.

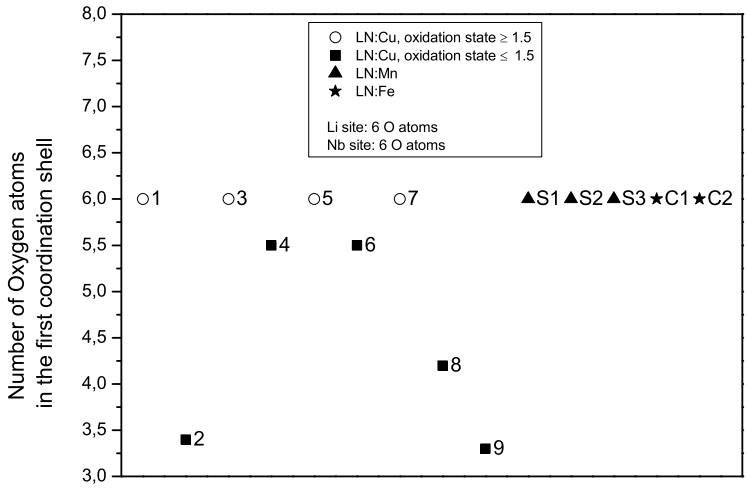

Figure A.4: Number of O atoms in the first coordination shell.

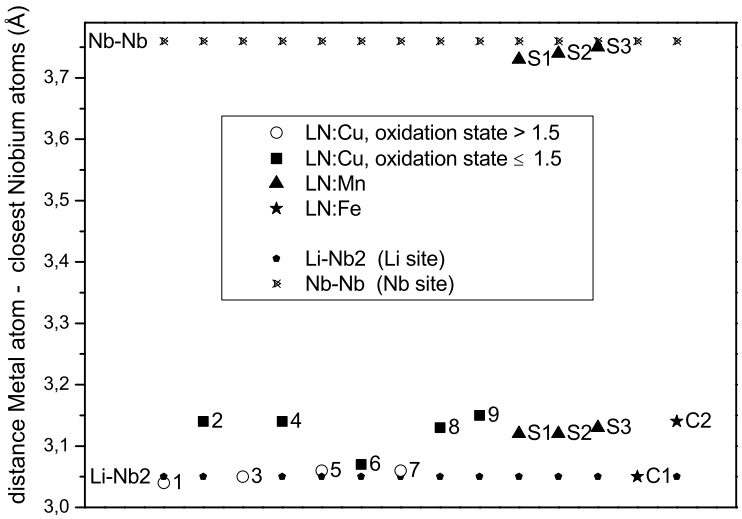

Figure A.5: Distances Metal-closest Nb atoms.

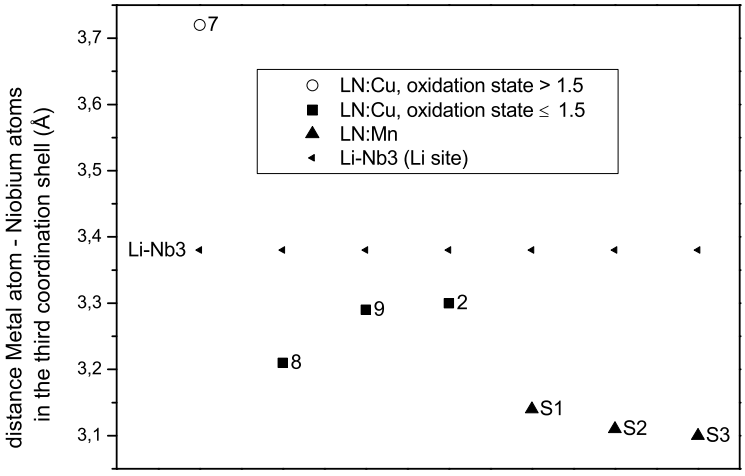

Figure A.6: Distances Metal-Nb atoms in the third coordination shell.

Appendix B

MoO_3 nanoparticles supported on Mesoporous SBA-15: Characterization of starting materials and the products using X-ray scattering, Physisorption, Transmission Electron microscopy, Raman and XAFS spectroscopy

Manuscript with the above title is in preparation. The X-ray scattering, Physisorption, Transmission Electron Microscopy (TEM) and Raman studies have been done by Zhida Huang and Dangshen Deng from the group of Prof. Bensch, University of Kiel. The author of the present thesis has contributed with XAFS spectroscopy measurements and analyses of Mo K-edge XAFS spectra. For completeness, the manuscript is presented as a whole in this chapter.

B.1 Introduction

In the past few years periodic silica based mesoporous materials such as MCM-41 and SBA-15 were used as templates for the syntheses of shape-selective new materials. The mesoporous materials are synthesized via the polymerization of silica around a periodic cationic amphiphiles (MCM-41) as well as neutral block copolymer (SBA-15). SBA-15 possesses well ordered hexagonal arrays of mesopores with pore diameters between 3 and 30 nm [216, 217], with thicker walls between 31 and 64 Å compared to MCM-41. Therefore, SBA-15 exhibits a higher thermal stability, being claimed to be stable for at least 48 h in boiling water [217]. Using SBA-15 with the narrow pore diameter distribution as a template for the synthesis of nanoparticles, yields products reflecting the diameters of the pores and maximal particle lengths in accordance of the channel lengths of the template material. Such incorporated nanoparticles may have interesting optical, magnetic and catalytic properties. In addition to the studies of the formation of metal nanoparticles and nanowires, such as Pt [59, 74, 205], Pd [110, 112, 194, 210], Au [59, 74, 102, 204, 205], Ag [74], and Ti [117], the formation of binary nanomaterials such as PbS[60], CdS [202], TiN [85], GaN [206]

within the nanoscale channels of these mesoporous materials have been explored. More recently, the highly ordered quantum wires like, $Zn_{1-x}Mn_xS$ [27] and $Cd_{1-x}Mn_xS$ [26] have been successfully synthesized within the mesopores of SBA-15.

The molybdenum oxide catalysts have been investigated intensively [22, 46, 91, 113, 124, 173], because of its importance in the technical processes, such as propene metathesis [115, 135], propene oxidation [62], methanol oxidation [116], ethanol oxidative photochemical reaction [135] and most important in hydrodesulfurization processes, which represent one of the largest groups of catalytic steps in petroleum and petrochemical reactions. Recently, SBA-15 supported MoO_3 materials were synthesized by thermal treatment of SBA-15 impregnated with ammonium heptamolybdate (AHM) [48], by thermal spreading of MoO_3 [161] or by sonochemical decomposition of $Mo(CO)_6$ in organic solvents [193]. The group of Blanchard et al. [161] mixed appropriate amounts of MoO_3 and SBA-15 in a mortar, heated the physical mixture to 773 K in He and sulfided the material in a 10% H_2S/H_2 atmosphere for 14 h at 673 K. A different approach was used by Dhar et al. [48]. The pristine SBA-15 material was impregnated with aqueous solutions of AHM followed by activation in a flow of CS_2/H_2 for 2 h at 673 K. Both groups used MoO_3 as an intermediate for the preparation of MoS_2 supported on SBA-15. But the formation of MoO_3 and especially the interaction of the oxide with the support were not investigated in detail. In the present work, MoO_3 species formed within SBA-15 are analyzed and characterized applying various analytical methods including Raman spectroscopy, N_2 physisorption, transmission electron microscopy (TEM), scanning electron microscopy (SEM), small angle and wide angle X-ray scattering experiments as well as X-ray absorption spectroscopy. From the results of these studies a complete picture about the structures of MoO_3/SBA-15 composite materials is obtained.

B.2 Experimental section

B.2.1 Synthesis of pristine Mesoporous SBA-15

8 g of poly(ethylene glycol)-block-poly(propylene glycol)-block-poly(ethylene glycol) triblock copolymer (Aldrich, pluronic, P-123) was dissolved in 240 g of water and 28.6 g of concentrated hydrochloric acid at 30 °C on a water bath. After drop wise addition of 16 g of tetraethyl orthosilicate (TEOS), the reaction mixture was stirred for 24 h at 30 °C. The resulting gel was transferred into a Teflon bottle and heated to 80 °C for 24 h to obtain SBA-15 with 6 nm pores. The resulting white powder was filtered and washed with deionized water, and the surfactant was removed by Soxleth extraction at 78 °C with a mixture of 970 mL of ethanol and 30 mL of concentrated hydrochloric acid. After washing with ethanol, the white powder was dried at RT for about one week.

B.2.2 Synthesis of MoO_3/SBA-15

Typically, 1 g of SBA-15 was stirred in aqueous solutions of ammonium heptamolybdate $(NH_4)_6Mo_7O_{24}$ $4H_2O$ (AHM) with different concentrations at pH 7-8. After stirring at room temperature for 18 h, the products were filtered without washing. The impregnated SBA-15 was calcined at 500 °C for 3 h to obtain MoO_3. This calcination temperature is much higher than the usual thermal decomposition temperature of AHM (350 °C) [129], at which MoO_3 is formed in air. At lower temperatures, AHM is found not completely to be decomposed to MoO_3 which indicates that AHM is located

in the pores and not on the outer surface of the material. The silica walls and small pore diameters can impede the removal of the decomposition products of AHM, such as NH_3 and H_2O, and consequently a higher formation temperature is required. Materials containing different Mo concentrations were prepared using appropriate concentrations of AHM, i.e. 0.03 M, 0.06 M, 0.09 M, 0.02 M and 0.05 M solutions. The synthesized products are abbreviated as Mo/SBA-15 (A), Mo/SBA-15 (B), Mo/SBA-15 (C), 3 wt% and 10 wt% with Mo loadings of 8 wt%, 13 wt%, 17 wt%, 3 wt% and 10 wt% respectively.

Small-angle and wide-angle powder X-ray diffraction (XRD) patterns were obtained on a Bruker D8 Advance diffractometer at room temperature using Cu K_α radiation generated at 40 kV and 30 mA. Fourier transform (FT) Raman spectra were recorded with a Bruker FT-106 Raman module, equipped with a Ge detector cooled by liquid nitrogen and connected to a Bruker FT-IR 66 interferometer and a continuous wave diode-pumped Nd:YAG Laser with a radiation wavelength of 1064 nm (9398.4 cm^{-1}). The laser power was set to 300 mW and the spectral resolution was 2 cm^{-1}. Nitrogen absorption measurements were carried out at 77 K on a Sorptomatic 1990 adsorption analyzer. Before the measurements, the samples were out gassed for at least 24 h at 120 °C [129]. The BET surface areas were calculated from p/p_0 = 0.03 - 0.3 in the absorption branch; the BJH pore size distributions were calculated from the desorption branch. Transmission electron microscopy (TEM) microphotographs were obtained on a JEOL JEM-200 FX electron microscope operating at 200 kV. Dried SBA-15 and MoO_3/SBA-15 powders were sonicated in dichloromethane for several seconds, dropped on the TEM grids, and dried on carbon-film-coated copper grids (Ted Pella) in air. SEM pictures were obtained on a Hitachi S-4800 scanning micro-analyzer. The Mo-content was determined with EDS analysis. Data were collected using an accelerating voltage of 20 kV and 120 s accumulating time.

The XAS experiment was performed at the INE beamline at the ANKA 2.5 GeV synchrotron radiation facility. For details about the instrumentation at this beamline, see [45]. For energy monochromatization, a Lemonnier-type [111] double crystal monochromator equipped with Ge(422) crystals was employed, leading to a minimum energy step width of 0.2 eV. For calibration, photon energy of 20 keV was assigned to the first inflection point of the K-edge spectrum of a molybdenum foil. The absorption spectra of the powder samples: Mo/SBA-15 (B) (with 13 wt% molybdenum loading) and MoO_3 reference were recorded at the Mo-K edge (20 keV) in transmission mode between 19.799 keV and 20.853 keV with energy steps of 0.5 eV and 2 seconds integration time per step. The data reduction consisted of subtracting a linear background fit to the pre-edge region (19.850 - 19.970 keV), and normalization of the spectra to an "edge jump" of one at 20.142 keV. ARTEMIS [151] was used for the EXAFS analysis. The XAFS signal $\chi(k)$ was Fourier-transformed to R space, utilizing the following parameters: k range: 4 - 15.7 $Å^{-1}$ for the Mo/SBA-15 (B) sample and 4 - 15 $Å^{-1}$ for the MoO_3 reference, k weight: 1,2 and 3, Kaiser-Bessel Window: dk = 2, R range: 1 - 4 Å. The fit was performed in R space. The number of varying parameters was kept always half the number of independent points. 5 important multiple scattering paths (4 collinear and one triangle) were applied in the fit of the Mo/SBA-15 (B) sample. 25 multiple scattering paths were utilized for the fit of MoO_3 reference. 0.003 and 0.01 r - factor of fits are obtained for the Mo/SBA-15 (B) sample and the MoO_3 reference respectively. For comparison of the FT EXAFS spectra of the Mo/SBA-15 (B) (13 wt%), Mo/SBA-15 (C) (17 wt%), 3 wt% and 10 wt% samples and MoO_3 and AHM references, the XAFS signals $\chi(k)$ were Fourier-transformed to R space, utilizing the following parameters: k range: 4 - 16 $Å^{-1}$, k weight: 2 and a Kaiser-Bessel Window: dk = 2.

B.3 Results and discussion

B.3.1 Powder X-ray Diffraction

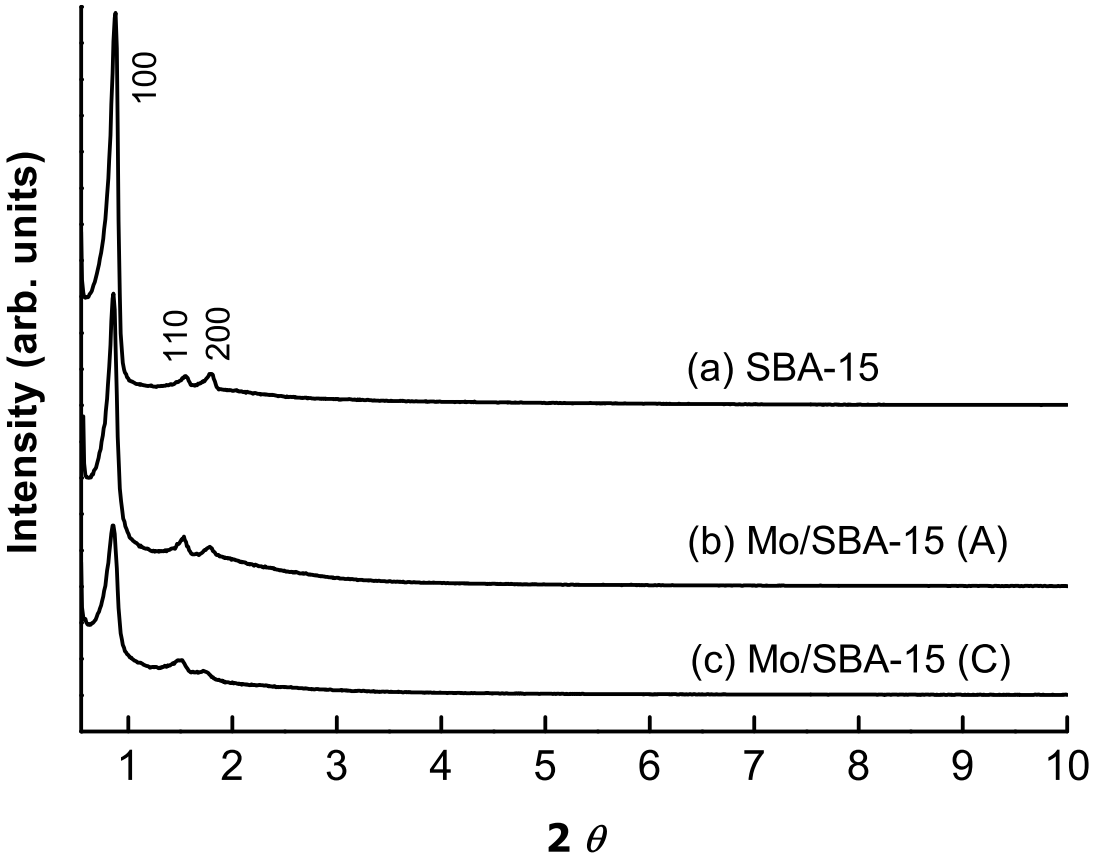

Figure B.1: Small-angle XRD patterns of (a) SBA-15, (b) Mo/SBA-15 (A), and (c) Mo/SBA-15 (C).

Figure B.1 shows the small angle patterns of MoO_3/SBA-15 in the 0.55° - 10° 2θ range. All samples display three reflections that can be indexed as the characteristic (100), (110), and (200) peaks of hexagonal mesoporous SBA-15 with space group p6m. The powder patterns indicate that the primary structure of SBA-15 consists of well ordered channels which are maintained after the formation of MoO_3 nanoparticles inside the channels. In addition, the phase cancellation between the pore walls and the guest species MoO_3 leads to a decrease of the intensity of Bragg reflections, which is more pronounced for higher MoO_3 contents. This phenomenon is well-known [27, 58] and was also observed in [48].

Figure B.2 shows wide angle XRD patterns of the MoO_3/SBA-15 samples together with a pattern of a physical mixture of MoO_3 and SBA-15. Some weak reflections of MoO_3 are visible in the 2θ region between 7 and 70° at a loading of 13 wt% Mo, and the reflection positions agree well with those of bulk MoO_3. Below 13 wt% Mo no reflections of crystalline MoO_3 occur in the patterns and only a broad feature caused by SBA-15 is observed, indicating that the crystallite size of the MoO_3 particles is below the coherence length of X-ray scattering of roughly 5 nm (see Fig. B.2,

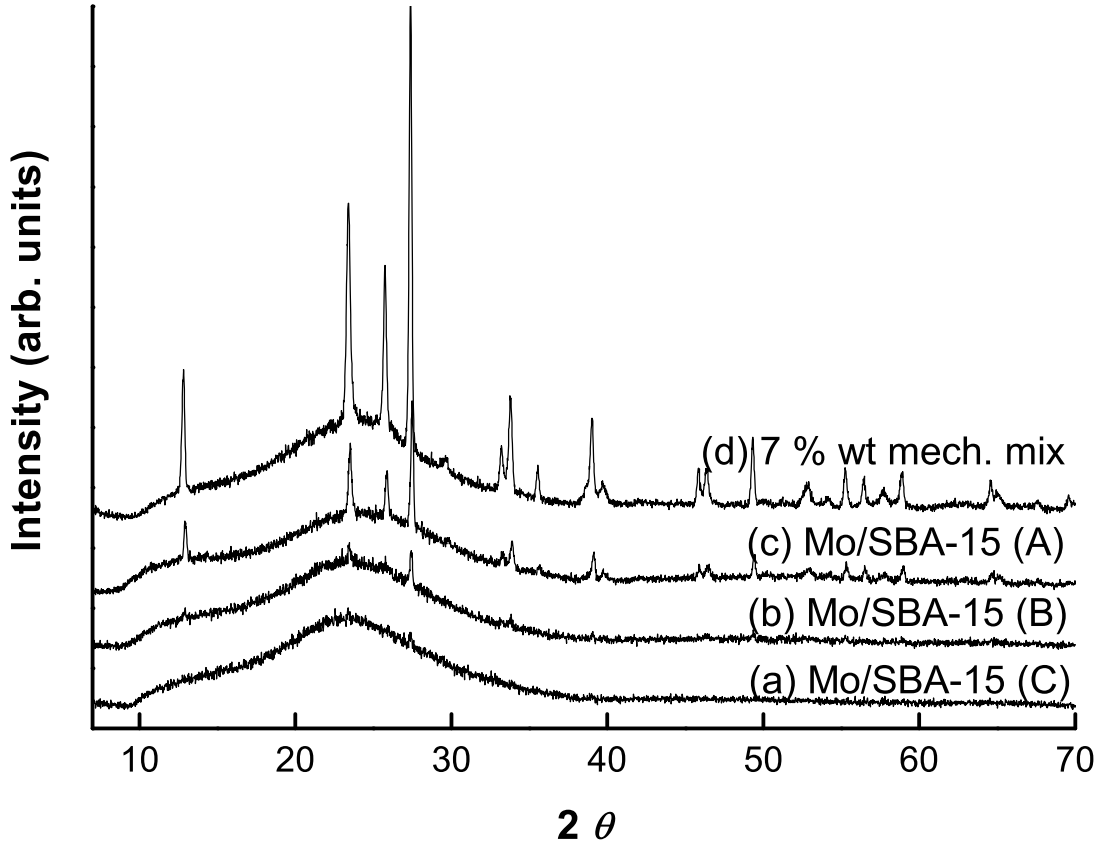

Figure B.2: XRD patterns of (a) Mo/SBA-15 (A), (b) Mo/SBA-15 (B), (c) Mo/SBA-15 (C) and (d) physical mixture with 7 wt% Mo.

trace (B) with 8 wt% Mo as an example). For higher loadings than 13 wt%, the reflections of MoO_3 become more intense with increasing MoO_3 content. But even for 17 wt% Mo in the SBA-15 pores the reflection intensity is much lower compared with the data of the mechanical mixture which has only 7 wt% Mo. The amount of actually crystalline dispersed MoO_3 can be estimated from the intensity of the XRD reflection located at $2\theta = 25.7°$. Because the intensity of Mo/SBA-15 (C) with 17 wt% Mo is nearly identical with that of a mechanical mixture of 3 wt% Mo, one may estimate that the amount of nanocrystalline highly dispersed MoO_3 for this sample is close to 14 wt%. Indeed, the maximal surface loading achieved can be evaluated to 1.7 ţmol m^{-2} (surface area of SBA-15 is about 850 m^2/g) for a fully dispersed MoO_3, which is in good agreement with the value determined by Blanchard et al. (2 ţmol m^{-2}) for SBA-15 support [161]. The results of the XRD investigations clearly indicate that the MoO_3 species are finely dispersed in the pores of SBA-15 and a similar observation was made by Dhar et al. [48]. The silica (Cabosil L 90)-supported MoO_3 was also investigated extensively by Desikan et al. [46]. The reflections of MoO_3 appeared already at a loading of 5 wt% Mo, which implies that mesoporous SBA-15 with the larger surface area facilitated the formation of MoO_3 on a nanoscale in our samples.

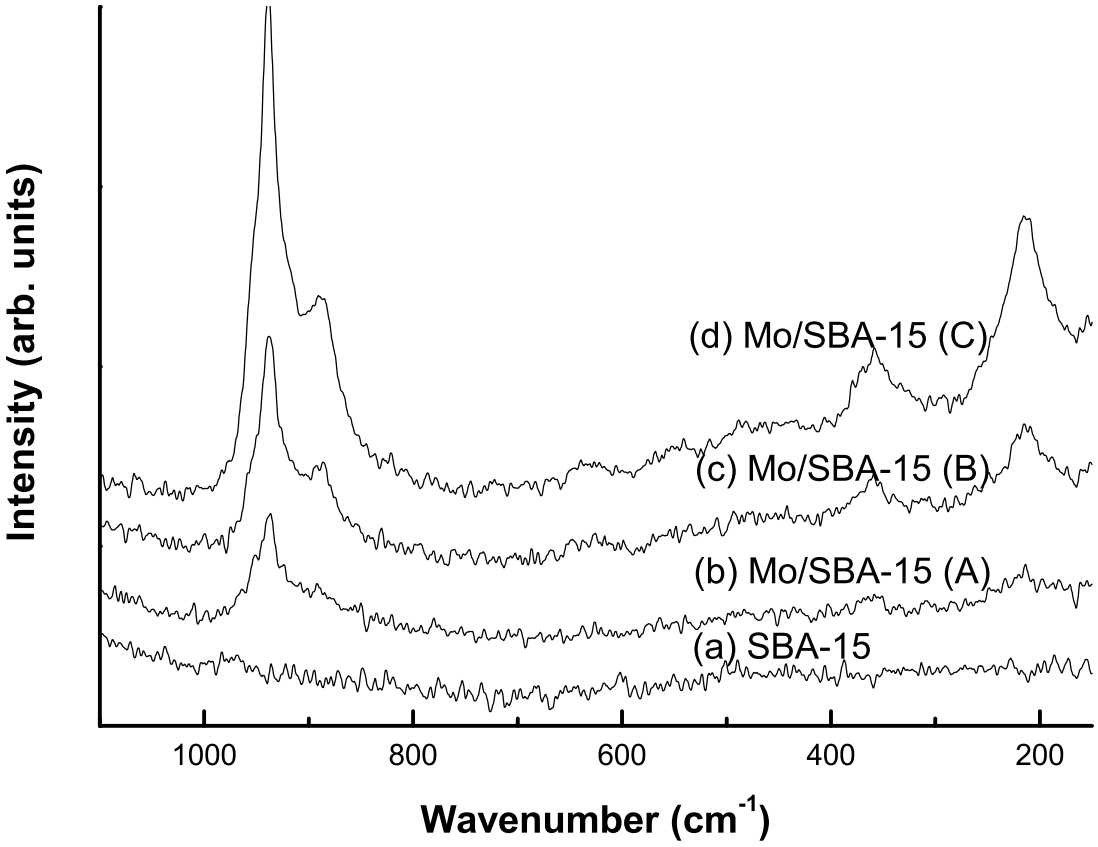

Figure B.3: Laser Raman spectra of (a) SBA-15, (b) Mo/SBA-15 (A), (c) Mo/SBA-15 (B) and (d) Mo/SBA-15 (C) before calcination at the temperature of 500 °C.

B.3.2 Raman spectroscopy

Raman spectroscopy is one of the effective methods to probe crystalline as well as amorphous nanoscale oxides [113, 173]. Raman spectra of impregnated samples before calcination are displayed in Figure B.3, and the characteristic bands of the $[Mo_7O_{24}]^{-6}$ anion are clearly visible for the sample with 8wt% Mo. As reported by Desikan et al. [46] the strong band at 943 cm^{-1} is due to the symmetric stretching of the short Mo-O terminal bonds of $[Mo_7O_{24}]^{-6}$ along with a weak and medium band at 898 cm^{-1}. The bending vibration at 362 cm^{-1} and deformation band at 320 cm^{-1} of the terminal Mo=O groups are also observed. The intensity of these bands increases with the amount of incorporated AHM.

The Raman spectra of calcined Mo/SBA-15 together with a spectrum of the mechanical mixture (Figure B.4) show the characteristic features of bulk MoO_3. MoO_3 is a layered material in which single layers are built up by MoO_3 tetrahedra sharing two oxygen corners with two neighboring tetrahedra are joined to form chains running along the c axis [95]. The Raman spectrum of MoO_3 between 82 and 995 cm^{-1} was investigated by Py et al. [149], who carried out a study on a single crystals and performed valence force-field calculations. The band at 994 cm^{-1} was assigned to the symmetric stretching of the terminal Mo=O groups and the signals at 819 and 665 cm^{-1} to the vibrations of the Mo-O-Mo bridge. The doublet at 290-280 cm^{-1} corresponds to the two wagging

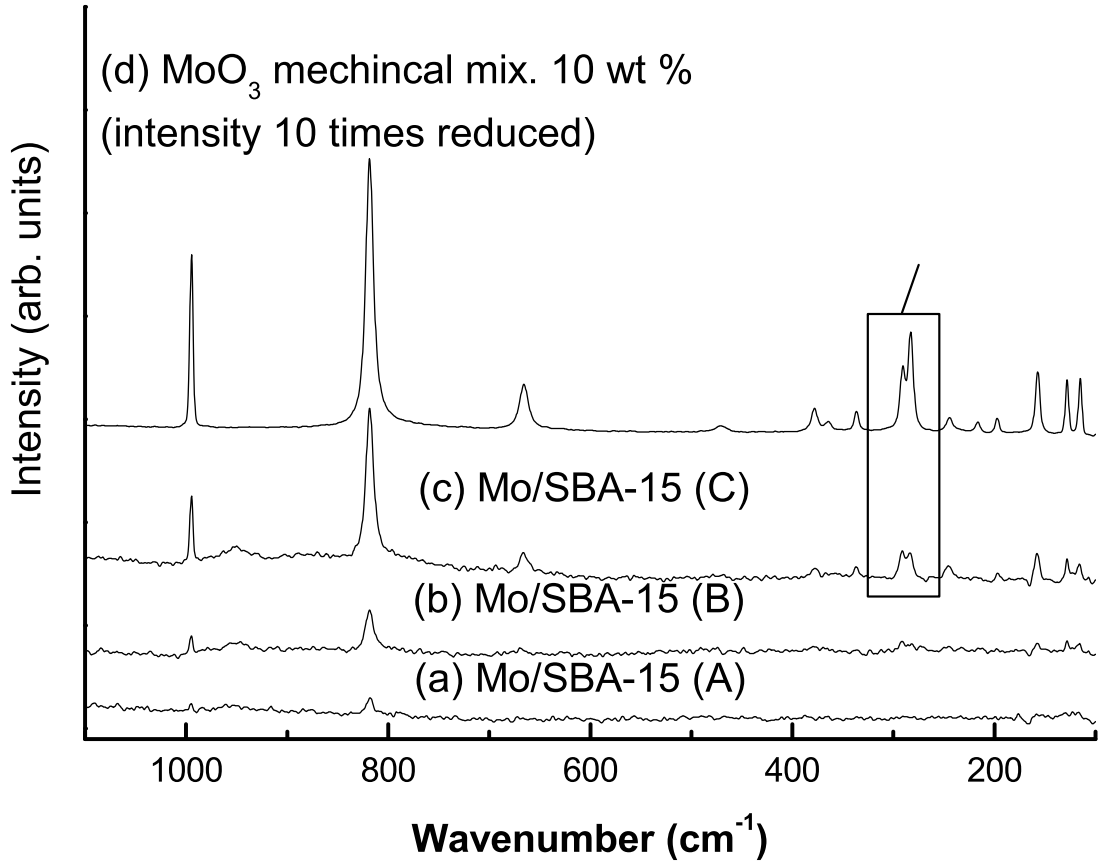

Figure B.4: Laser Raman spectra of (a) Mo/SBA-15 (A), (b) Mo/SBA-15 (B), (c) Mo/SBA-15 (C), and (d) mechanical mixture with 10 wt% Mo.

modes of the terminal Mo=O groups.

Apparently, these bands are observed in the spectrum of Mo/SBA-15(A) with 8 wt% Mo. For lower loadings the predominant silica-supported molybdenum species were observed to be isolated molybdate tetrahedra [91]. However, no bands at 988 and 620 cm^{-1} characteristic of MoO_4^{2-} were detected in our sample. But the formation of such isolated species may be below the detection limit. At high loadings, the observed wave numbers for MoO_3/SBA-15 materials are similar to that found for the physical mixture. However, four different features in the Raman spectra should be highlighted. The Raman spectra of MoO_3/SBA-15 materials exhibit a drastic intensity loss compared to the physical mixture with the same Mo content. The intensity reduction may be explained by a reduced effective scattering volume of dispersed MoO_3 particles. Such a size dependent intensity change was also reported by Mestl et al. [124]. Furthermore, the spectra show a change of the relative intensity of the MoO_3 characteristic modes at 819 and 994 cm^{-1}, which may be associated with the weak interaction between the highly distorted small MoO_3 particles and the SBA-15 support. The typical intensity ratio I_{994}/I_{819} for Mo/SBA-15 (B) and Mo/SBA-15 (C) is 0.44 which is smaller than that of the mechanical mixture of 0.64. An identical feature was observed by Braun et al. [22], who prepared the silica (aerosil-200) supported MoO_3 by thermal spreading of bulk MoO_3. In addition, an interesting phenomenon in the Raman spectra is the change in relative intensity

of the two wagging modes at 290 (B_{2g}) and 280 cm^{-1} (B_{3g}). In the single crystal and the physical mixture spectra, the B_{3g} wagging mode has only 2/3 of the intensity of the B_{2g} mode. For all the MoO_3/SBA-15 samples, the B_{3g} wagging mode is as intense as the B_{2g} signal and the two modes are hardly resolved. This observation is consistent with a phenomenon which has been discussed by Braun et al. [22] in the spectra of Mo/Al_2O_3 and Mo/SiO_2 samples. The two wagging modes of the terminal Mo=O groups are parallel polarized to the direction of the chain of the tetrahedral MoO_4 units, i. e. directed along the c-axis. Therefore, the change of the intensity ratio for this doublet may be attributed to the distortions along the MoO_4 chains. Finally, a weak shoulder appears at about 953 cm^{-1} corresponding to the Mo=O vibration of a polymeric molybdate species interacting with the support [173]. This observation suggests that spreading of MoO_3 particles on the SBA-15 support at high temperatures occurs to form $(MoO_3)_n$ oligomers.

B.3.3 Nitrogen physisorption

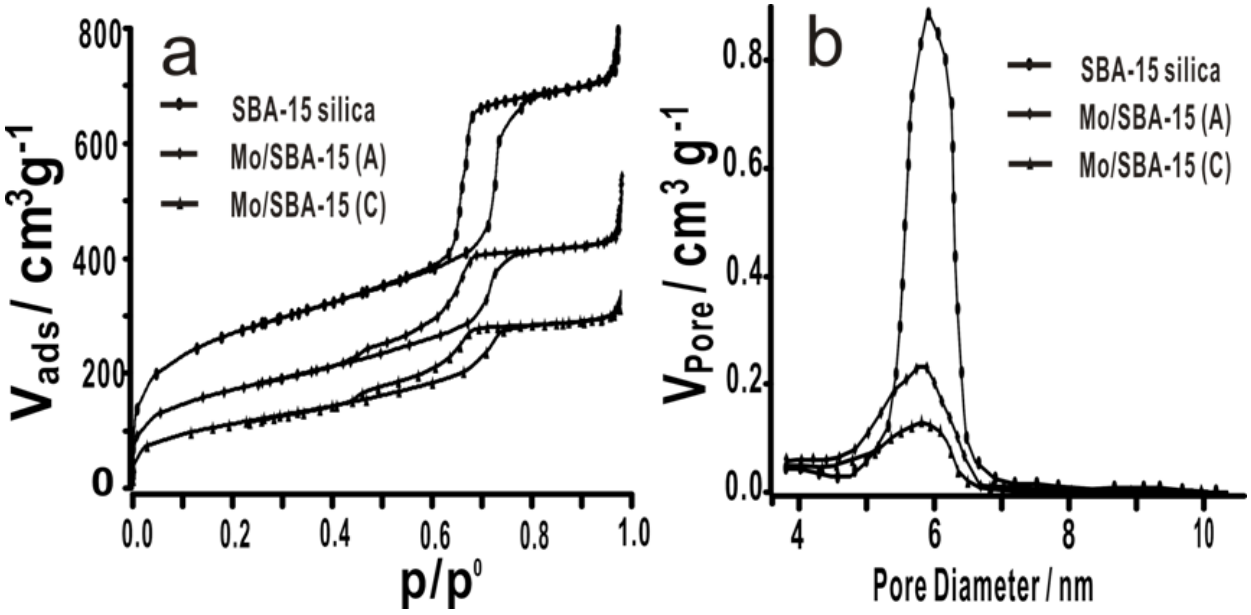

Figure B.5: Nitrogen absorption/desorption isotherms of MoO3/SBA-15 (a) and BJH pore-size distributions (b).

Figure B.5 displays the N_2 adsorption-desorption isotherms (at 77 K) and the pore-size distribution of SBA-15 and the MoO_3 impregnated SBA-15 materials with different Mo concentrations and the numerical data are listed in Table B.1. For all materials a type IV isotherm is observed, which is the typical hysteresis loop of mesoporous materials [4], indicating that the incorporation of Mo species does not destroy the structure of mesoporous SBA-15. The pore sizes were calculated from the desorption branch of the isotherm using the Barrett-Joyner-Halenda (BJH) model, which is an appropriate method for determining changes in the pore-size distribution [26, 27, 109], and the Barrett-Emmett-Teller (BET) equation was applied for calculation of specific surface areas. For SBA-15 the capillary condensation step was typically at the relative pressure p/p_0 = 0.6 - 0.7. After introduction of MoO_3 particles into the pores, the capillary condensation step shifts to lower relative pressure p/p_0 = 0.4 - 0.6, which is caused by the decrease of the pore sizes. Moreover, the

Sample	MoO3 loading wt%	Pore volume ($cm^3\ g^{-1}$)	BET surface area ($m^2\ g^{-1}$)	Mean pore diameter D (nm)	Wall thickness t (nm)
SBA-15	0	1.08	920	5.96	4.31
Mo/ SBA-15 (A)	8	0.65	597	5.34	4.93
Mo/ SBA-15 (B)	13	0.55	505	5.11	5.16
Mo/ SBA-15 (C)	17	0.45	397	5.02	5.25

Table B.1: BET surface area, mean pore diameter D, and wall thickness t (calculated from t = a - D^{18}, a = cell parameter), for the pristine SBA-15 silica and the MoO_3/SBA-15 host-guest compounds.

amount of adsorbed nitrogen decreased significantly, which is associated with the smaller specific surface area (Table B.1). The pore volumes decrease with increasing amount of impregnated Mo in SBA-15. In addition, the mean pore diameter (Figure B.5b) decreases as evidenced by the slight shift of the main peak in pore-size distribution curves to smaller values. The pore volumes of 1.08 $cm^3\ g^{-1}$ and 0.45 $cm^3\ g^{-1}$ are calculated at $p/p_0 = 0.9$ for pristine SBA-15 silica and Mo/SBA-15(C). The degree of filling can then be estimated to be more than 55% for the sample with 17 wt% Mo. All effects can be attributed to the coating of the silica walls of SBA-15 by MoO_3 particles, and the mesoporosity of the support is still preserved after the successful incorporation of MoO_3 particles throughout the SBA-15 channels. Similar effects in the N_2 physisorption curves were observed for intrapore formation of nanoparticles inside different host structures [26, 27].

B.3.4 Transmission Electron Microscopy and Scanning Electron Microscopy

The results of the XRD investigations, Raman spectroscopy and nitrogen physisorption experiments are proved by Transmission Electron Microscopy (TEM) (Figure B.6) and Scanning Electron Microscopy (SEM) (FigureB.7). The hexagonal ordered pore structure and the columnar frameworks can be clearly observed in all images, indicating that the hexagonal structure was maintained after inclusion of MoO_3 and calcination at high temperatures. It can be seen from the SEM picture (Figure B.7) that there are no crystals of MoO_3 being formed outside the pore systems. The view perpendicular to the pores shows that the wall thickness is larger after MoO_3 incorporation (Figure B.6d) in comparison with SBA-15 (Figure B.6b). In addition, the image also evidences a homogenous dispersion of MoO_3 along the silica pore channels. Hence, the nanoscale MoO_3 in the pores may better described as a nanowire-like material rather than individual nanosized particles.

B.3.5 XAFS

XANES analysis

The Mo K-edge XANES spectrum of the Mo/SBA-15(B) sample displayed in Figure B.8 differs from the crystalline MoO_3 reference spectrum. A magnification of the spectra is shown in Figure B.9. Co-existence of other Mo oxide valencies, different from Mo 6+, is excluded, as the spectrum of the Mo/SBA-15(B) sample does not exhibit energy shift (Fig. B.8). Right at the absorption edge, a notable degree of similarity to the spectrum of $(NH_4)6Mo_7O_{24}\ 4H_2O$ (AHM) is observed, although the "D" shape resonance is shifted by about 5 eV indicating that one is not dealing with AHM. However, AHM contains molybdenum oxide (Mo 6+) clusters leading to the question whether the

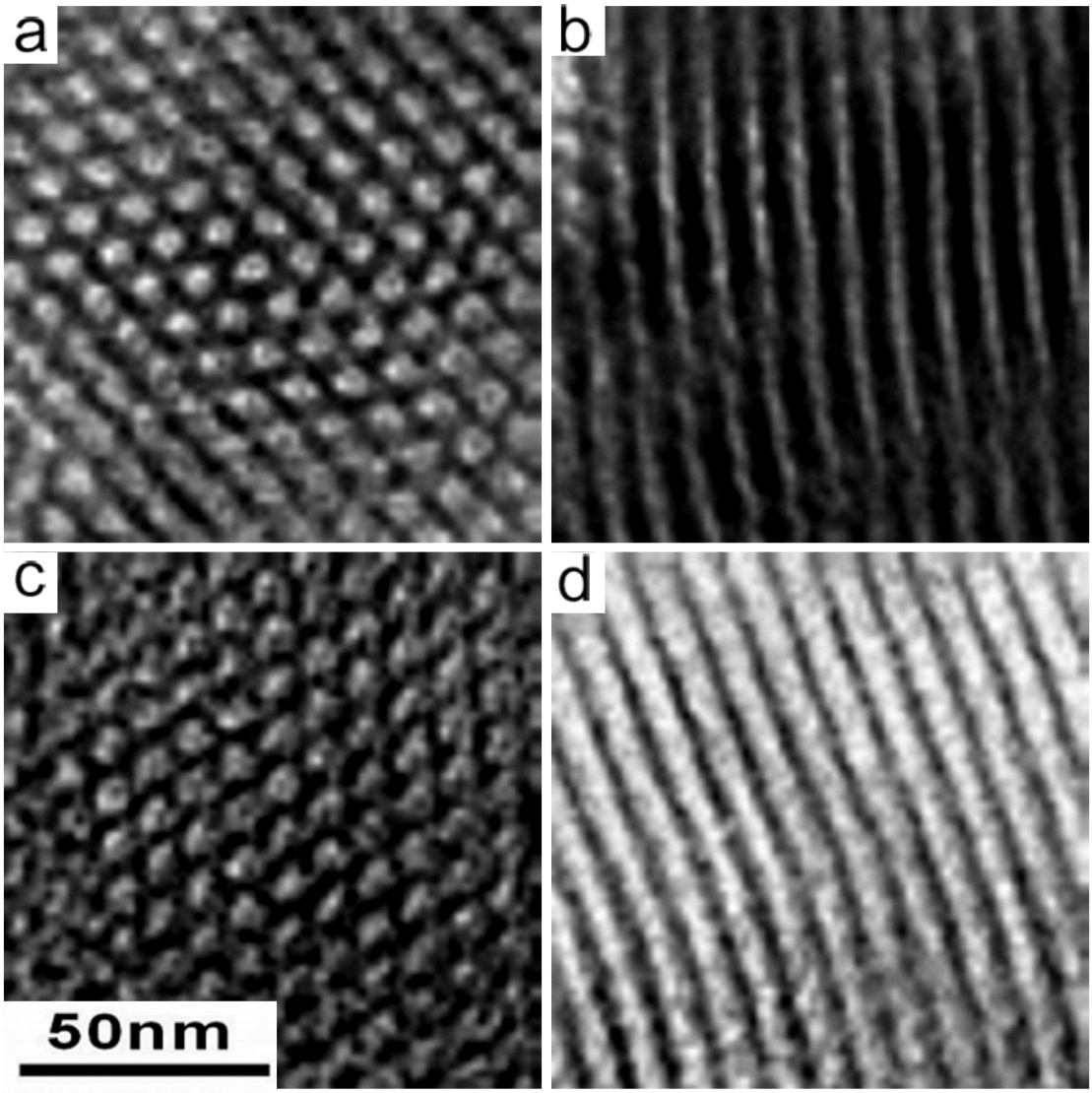

Figure B.6: TEM images of SBA-15 silica ((a) (b)), TEM images of MoO3/SBA-15 ((c) (d)), (a) and (c) taken with the beam direction parallel to the pores. (b) and (d) taken with the beam direction perpendicular to the pores.

observed spectral changes can be induced by the geometrical constraints, i.e. on the one hand reduced particle size and on the other hand a crystal structure with preferable orientation of growing, which may be enforced by the structure of the substrate. In order to verify this assumption, theoretical calculations with the FEFF8 code based on the real-space full multiple scattering approach [10] have been performed on a systematic series of model compounds. This approach is justified by the fact that calculated spectra using this code are usually in satisfactory agreement with the measured spectra [126, 136]. In addition, it was successfully applied for a qualitatively reproduction

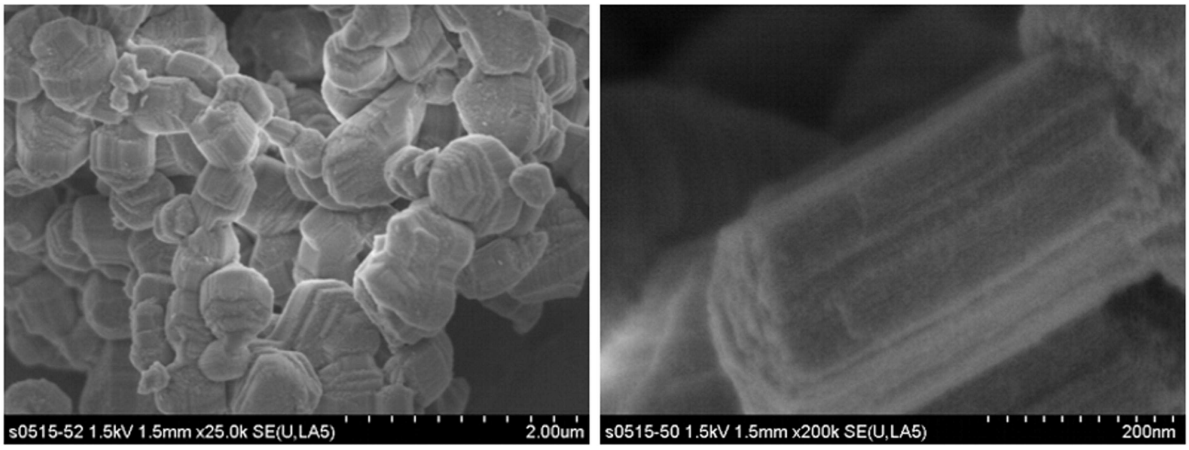

Figure B.7: SEM images of the MoO3/SBA-15.

of changes in the spectra of nano-scaled materials [9, 155].

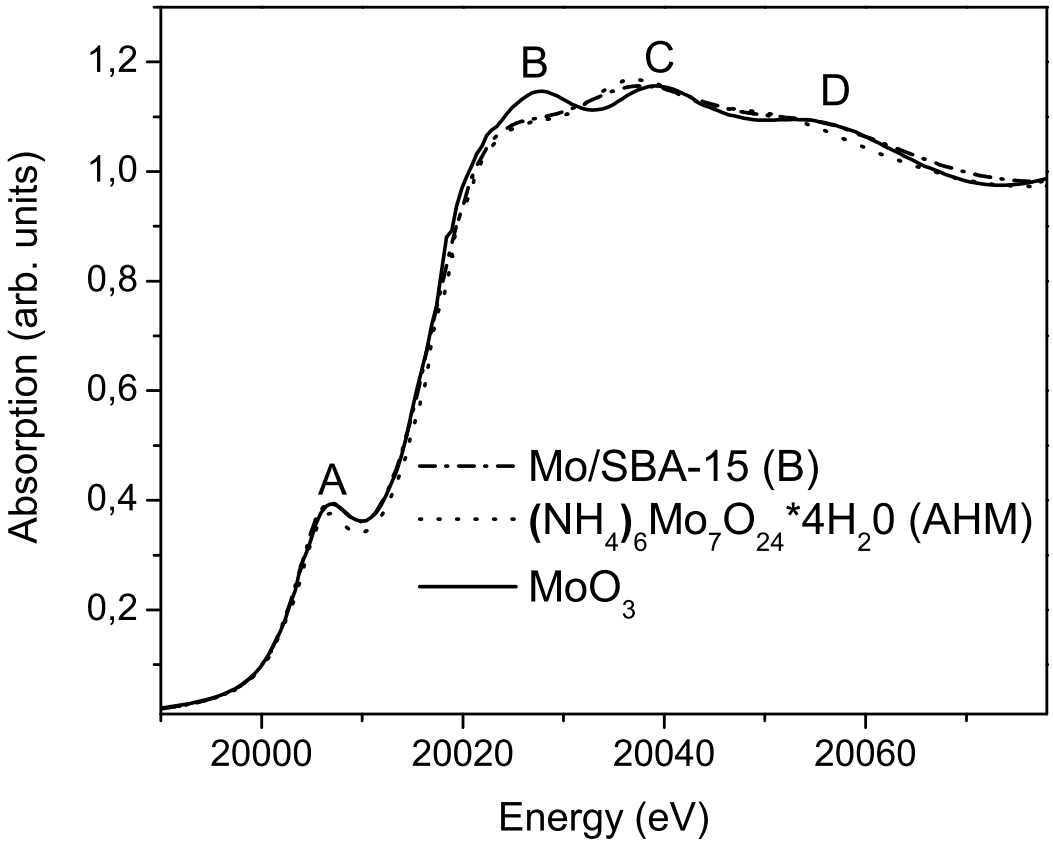

Figure B.8: Experimental XANES spectra of Mo/SBA-15 (B) sample (dash dot) and MoO_3 reference (solid) and (NH4)6Mo7O24*4H2O (AHM) (dot).

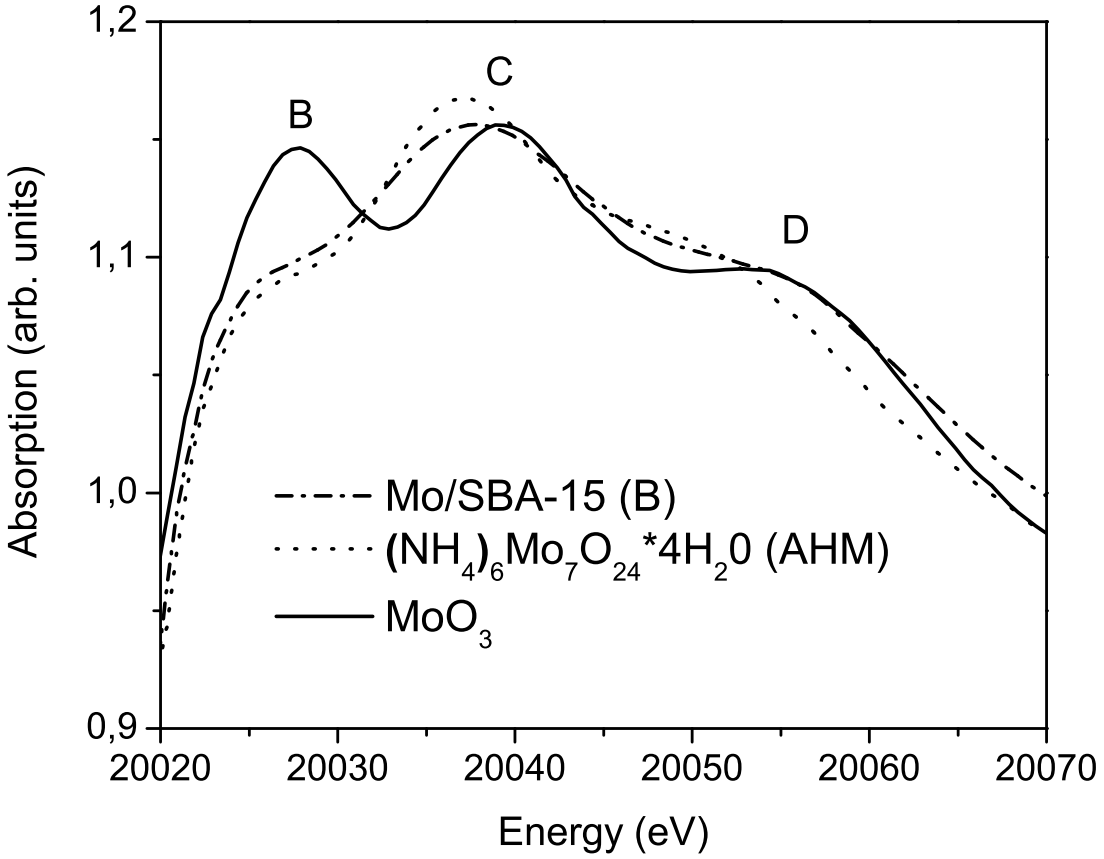

Figure B.9: A magnified region (from 20 020 eV to 20 070 eV) of the XANES spectra of Mo/SBA-15 (B) sample (dash dot), MoO_3 reference (solid) and $(NH_4)6Mo_7O_{24}$*$4H_2O$ (AHM) (dot).

The following models were studied in detail:
The first model, provoked by the differences in the XANES region of "B" and bulk MoO_3 spectra, includes varying cluster sizes of MoO_3 considering the first coordination shell, 20, 87, and 200 atoms which are named: "MoO_3 first shell", "MoO_3 20 atoms cluster", "MoO_3 87 atoms cluster" and "MoO_3 200 atoms cluster" in Figure B.10 (the calculated MoO_3 spectrum converges at 200 atoms). Increasing the number of cluster atoms beyond 20 atoms yields spectra which become very similar to that of bulk MoO_3 (200 atoms), therefore these spectra are not displayed in Figure B.10.

The second model is incited by the rod-like framework of the grown material, which is induced by the hexagonally shaped substrate material possibly leading to a structure with extended dimensions. This model is based on preferred growth directions of a 20-atoms cluster. The according spectra in Figure B.10 are denoted as "MoO_3 xy 20 atoms cluster", "MoO_3 xz 20 atoms cluster", "MoO_3 yz 20 atoms cluster", "MoO_3 x 20 atoms cluster", "MoO_3 y 20 atoms cluster", and "MoO_3 z 20 atoms cluster" , where x, y, z define the direction of extension of the clusters. The missing direction/s in the name, for example z in "MoO_3 xy 20 atoms cluster" and x and z in "MoO_3 y 20 atoms cluster" means that the z or x and z coordinates of the atoms, do not exceed 2 Å. In Figure B.10 the series of calculated spectra are plotted together with the experimental "MoO_3" and "Mo/SBA-

15(B)" spectra (underlined). For the qualitative comparison, the position and general shape of the three most characteristic features, named "B", "C" and "D" in Figure B.8, and the form of the shape resonance region of the spectra, i.e. the region after 20070 eV in Figure B.10 (arrow b), are taken into account. Comparing the modeled spectra of the first approach considering different cluster sizes with the experimental "Mo/SBA-15(B)" and "MoO_3" spectra, one can conclude that the "MoO_3 20-atoms cluster" spectrum clearly resembles the spectrum of "Mo/SBA-15(B)", while "MoO_3 87 atoms cluster" and "MoO_3 200 atoms cluster" spectra are representative for bulk MoO_3. It should be kept in mind that the FEFF8 code tends to underestimate the first resonance at the main absorption edge which is marked Figure B.10 (arrows next to letter a). More examples for this effect can be found in [136, 211]. The decreased amplitude of resonance a) (Fig. B.10) is a reasonable explanation for the slight misfit between the energy positions of the second and third resonances from the so called White Line (WL) region of the calculated MoO_3 (Fig. B.10, "MoO_3 200 atoms cluster", a1 and a2) compared to the experimental MoO_3 spectrum, the effect is visible on some of the spectra in reference [211].

Examining the "MoO_3 x 20 atoms cluster", "MoO_3 y 20 atoms cluster" and "MoO_3 z 20 atoms cluster" spectra (second model) (Fig. B.10), one intuitively connects each of the three peaks marked as "B", "C", and "D" in Figure B.9 with a respective crystallographic direction of growing, for example the "B" peak becomes well pronounced in the case of atoms with y coordinates above 2 Å ("MoO_3 y 20 atoms cluster", Figure B.10, arrow next to letter c). Taking into account this observation and the reduced dimensionality of the calcined MoO_3, a further exploration of the calculated spectra leads to an improved agreement between experimental and calculated data (Fig. B.10). The experimental "Mo/SBA-15(B)" spectrum is best described by the calculated "MoO_3 xy 20 atoms cluster" spectrum (Fig. B.10). In reality, the SBA-15 supported MoO_3 might not only be qualified as a nano-sized material, but also as a low dimensional material with a preferred orientation of growth. The results of this novel approach consisting of size and shape dependent calculations indicate that the low-dimensional MoO_3 (Mo/SBA-15 (B)) might predominantly grow in the x and y crystallographic directions. This preferred growth may be dictated by the structure of the porous substrate.

EXAFS analysis

In any case, the EXAFS analysis confirms the reduced dimensionality of the material inside the SBA-15 pores. The decreased overall amplitude of the "Mo/SBA-15(B)" XAFS spectrum in k space (χ(k)) (Fig. B.11 a) compared to the one of "MoO_3" (χ(k)) (Fig. B.11 b) evidence to reduced coordination numbers in all shells [57]. The decreased amplitudes of peaks A and B in Figure B.11 c of the Radial Distribution Function (RDF) of the SBA-15 supported MoO_3, compared to the RDF of the MoO_3 reference also exhibit this tendency. A quantitative verification, achieved by fitting the first and higher coordination shells (until 4 Å) of the RDF of "Mo/SBA-15(B)" and "MoO_3" spectra is shown in Table B.2. Significant decrease of coordination numbers: 56.6 % O and 57% Mo compared to bulk MoO_3 is obtained, clearly attesting to formation of low dimensional material. The gradual decrease of distances going from first shell (between 1 and 2.4 Å) towards outer shells (between 2.4 and 4 Å), compared to α - MoO_3, (the obtained distances for α - MoO_3 are consistent with the values in references [156, 157, 199]) can be explained by the transition from bulk like to surface like structure [57]. This trend is fully followed by the coordination numbers [57]: 25% decrease O atoms in the first coordination shell (between 1 and 2.4 Å), whereas 72 % less O atoms and 57% less Mo atoms in higher coordination shells (between 2.4 and 4 Å). The hypothesis for preferable x and y orientation of growing of the material is supported by the EXAFS fit, as only

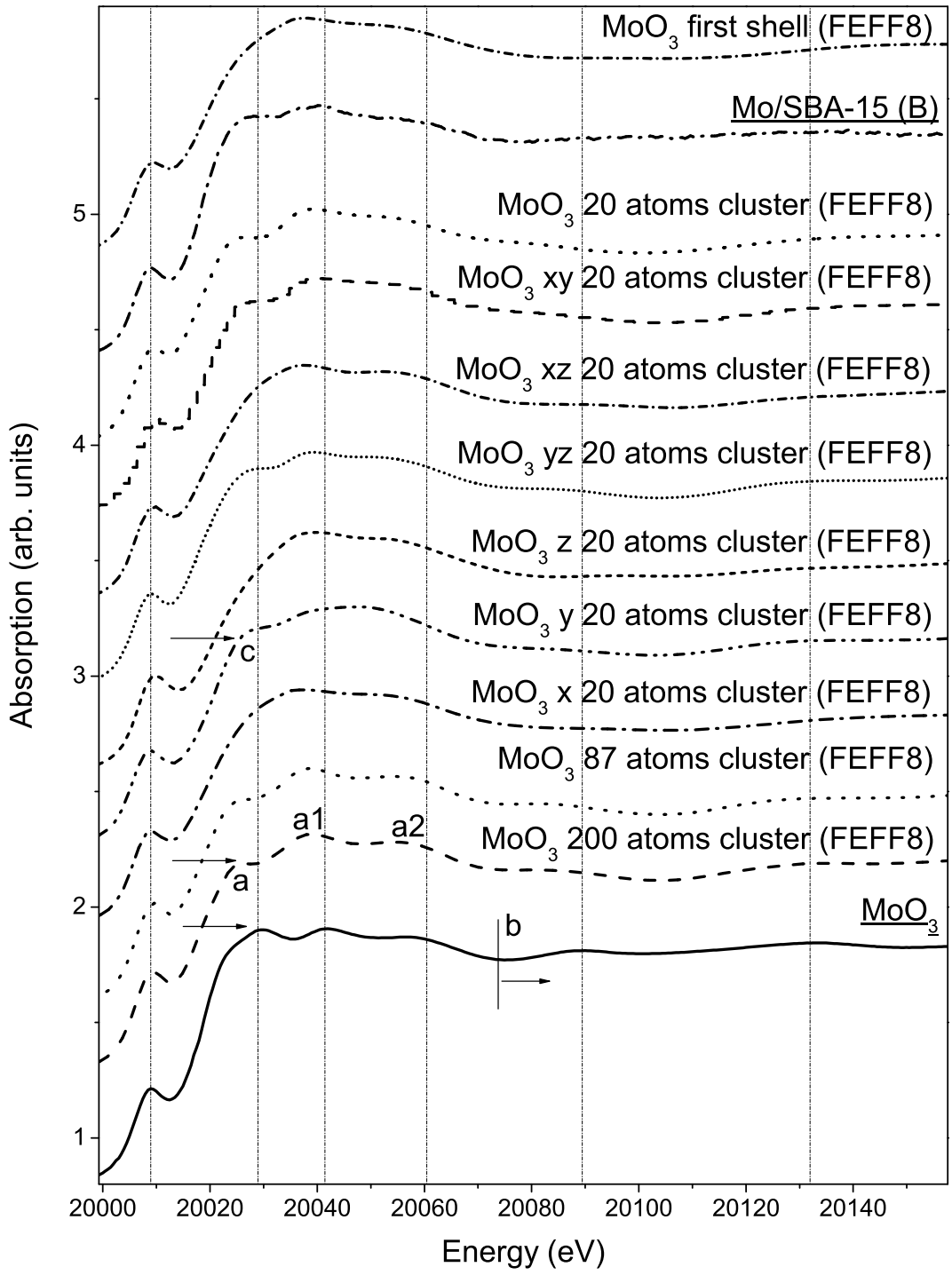

Figure B.10: A series of calculated spectra (FEFF8 code) (labeled in black) in comparison with the experimental spectra of Mo/SBA-15 (B) sample (dash dot, labeled in black and underlined) and MoO_3 reference (solid, labeled in black and underlined).

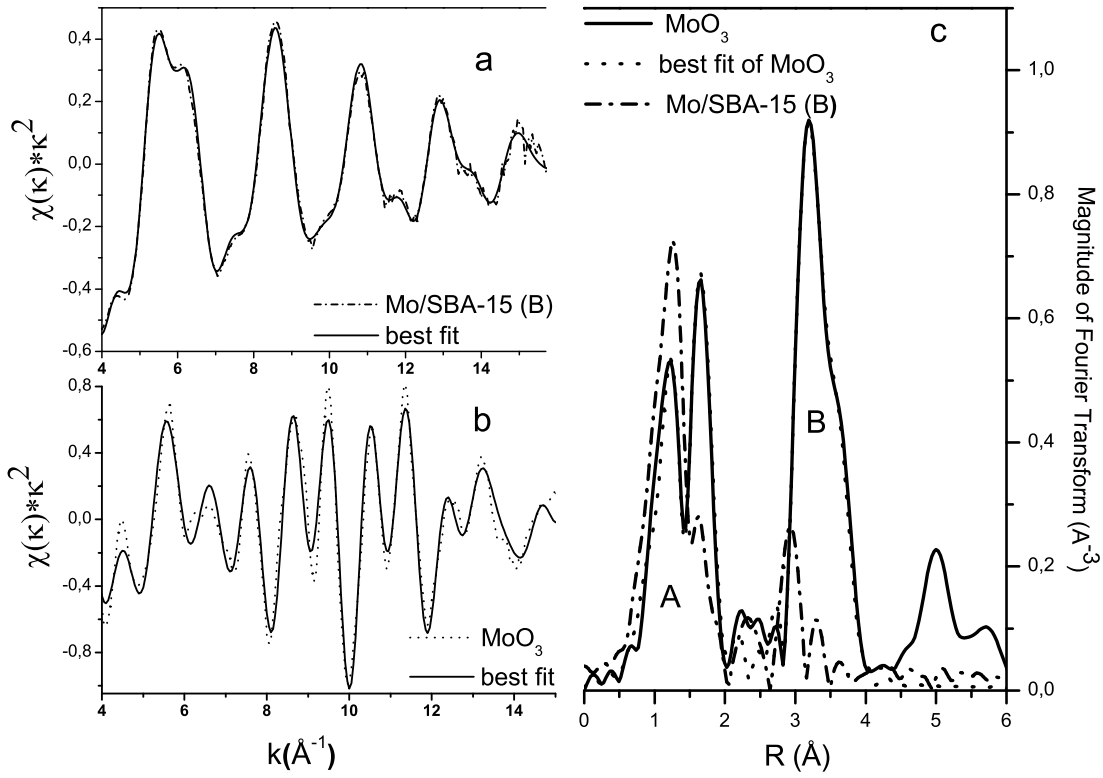

Figure B.11: The XAFS spectrum of Mo/SBA-15 (B) sample in k space (χ(k)) (dash dot) together with the best fit (solid); b: The XAFS spectrum of a - MoO_3 reference (dot) in k space (χ(k)) together with the best fit (solid): c: The RDF of MoO_3 reference (solid), its best fit (dot) and the RDF of Mo/SBA-15 (B) sample (dash dot).

atoms with z coordinates smaller than 2 Åare applied (e.g. best fit is achieved using Mo1 (z = 1.85 Å) and Mo3 (z = 0 Å) and omitting Mo2 (z = 3.7 Å)). In Figure B.12 the three main steps leading to closest agreement between data and simulation are displayed. In Figure B.12, the RDF of "Mo/SBA-15 (B)" its best fit and the single scattering paths applied in the fit are plotted. Despite the good r factor of fit (r = 0.012), the circled region from the real part of the Fourier transformed "Mo/SBA-15(B)" spectrum and its fit plotted in Figure B.11 b, clearly demonstrate a discrepancy between data and simulation. An improved fit (r = 0.006) is obtained by adding a Mo-O single scattering path at around 2.4 Å, Figure B.12 c and d. However, in order to achieve best accordance with the data (r = 0.003), a Mo-Si single scattering path is required at around 2.9 Å, Figure B.12 e and f. The connection nanowire - substrate, Mo-O-Si, might be built through the O5 atom, as it is at a slightly higher (+0.04 Å) distance than the respective atom in the MoO_3 structure.

The "Mo/SBA-15 (B)" (13 wt% MoO_3) spectrum is compared with the spectra of MoO_3, AHM and the spectra of SBA-15 loaded with 3, 10 and 17 wt% MoO_3 in Figure B.13. The spectra of all samples differ from the MoO_3 and AHM spectra. The features in the 17 wt% spectrum marked with arrows are more pronounced than the respective in the other samples. Since these features are characteristic for the MoO_3 spectrum, their gain in intensity indicate a higher contribution of

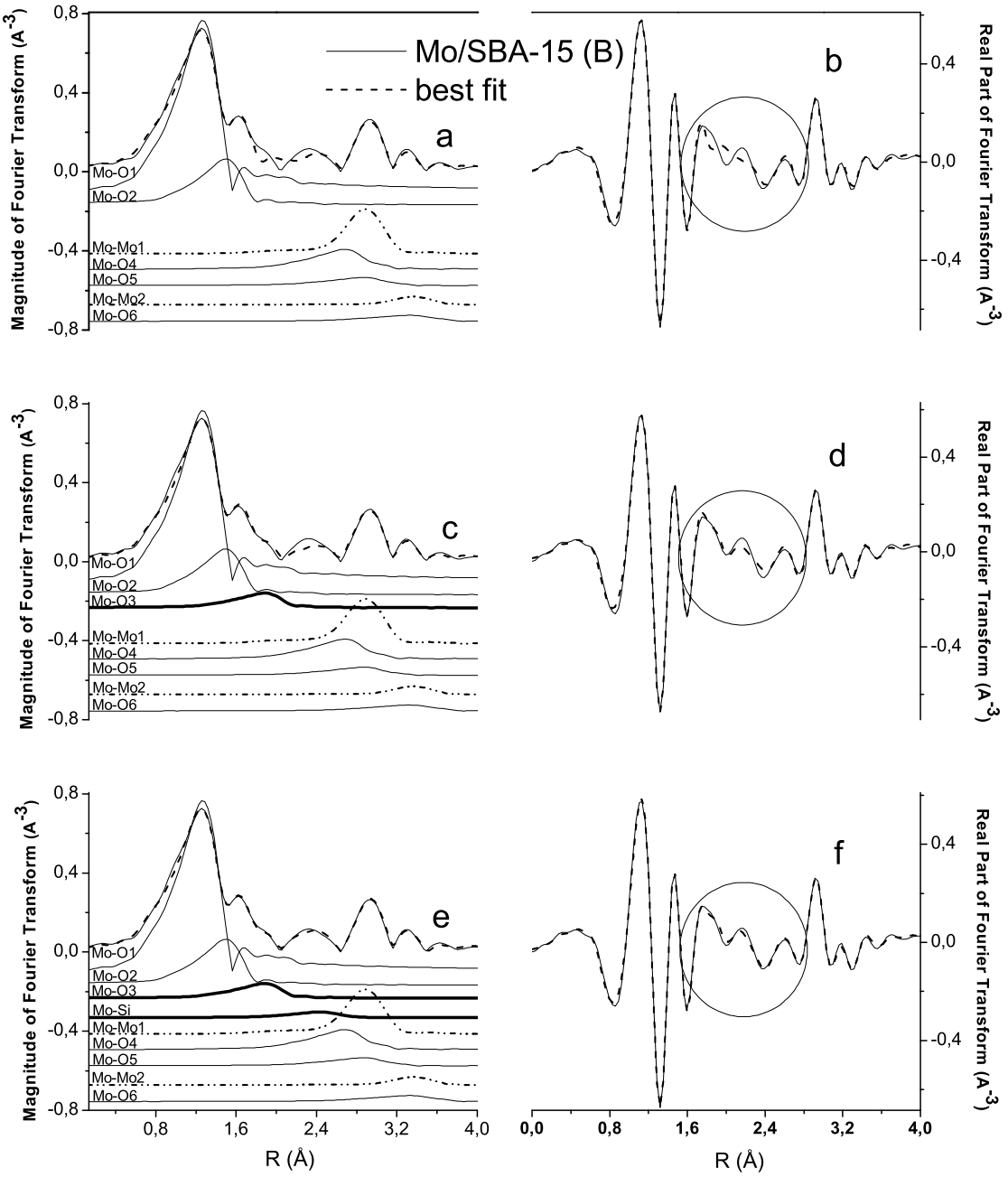

Figure B.12: The RDF of Mo/SBA-15 (B) sample (solid), its best fit (dash) and the single scattering paths applied in the fit (Mo-O: solid, Mo-Mo: dash dot dot); b: the contents of B.12a and an additional Mo-O single scattering path (solid bold); c: the contents of B.12b and an additional Mo-Si single scattering path (bold solid).

bulk-like MoO_3 in the 17wt% sample. The FT EXAFS spectra are plotted in Figure B.14. The spectrum of the 17wt% sample slightly differs from the spectra of the other samples in the region of the Mo-Mo single scattering paths (3-3.5 Å). All other samples appear to have very similar short

range structure (4 Å).

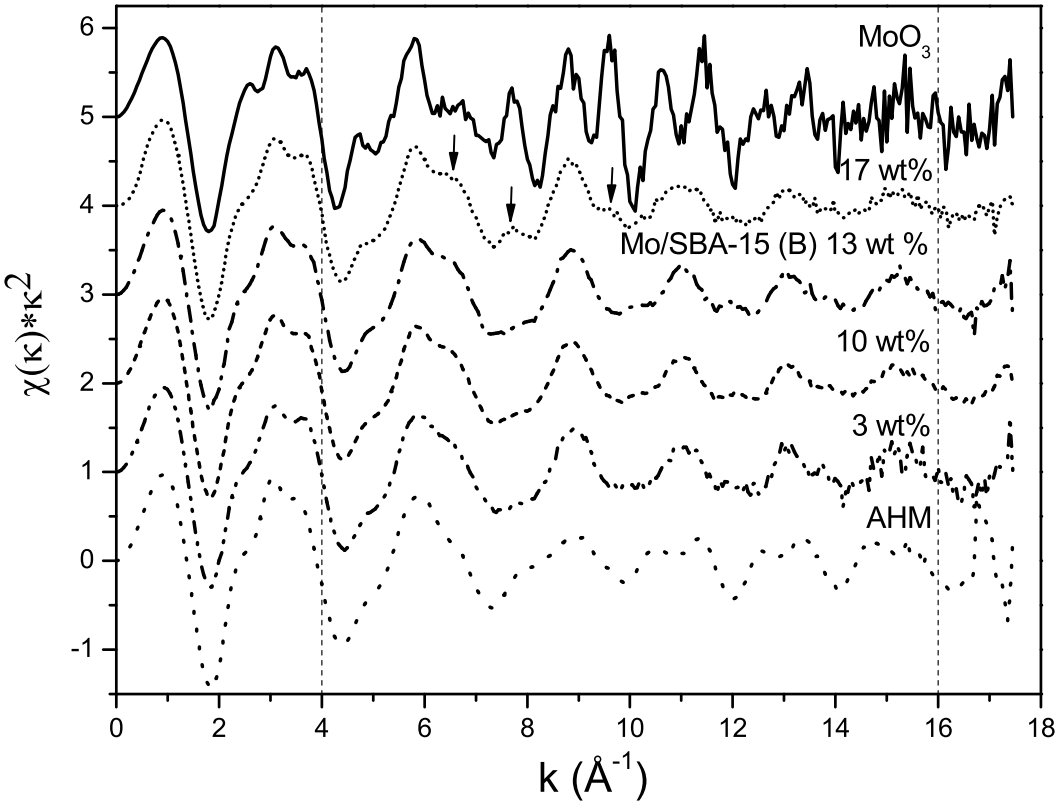

Figure B.13: χ(k) spectra.

B.4 Conclusion

In summary, the formation of MoO_3 nanowires within the nanoscale channels of SBA-15 with different Mo-concentrations has been demonstrated. Ammonium heptamolybdate dissolved in water was used as the Mo precursor and introduced into the SBA-15 powder; and the formation of $[Mo_7O_{24}]^{-6}$ anion can be observed in Raman spectra. Raman spectroscopic measurements show the strong effects of the reduced dimensions on the vibraitonal properties of MoO_3. The appearance of a weak shoulder at about 953 cm^{-1} indicating the spreading of MoO_3 particles on the SBA-15 to form $(MoO_3)_n$ oligomers. In addition, the formation process and the existence of these nanowires have been examined by XRD patterns, Nitrogen adsorption-desorption isotherm measurements, TEM and SEM images. The decreasing intensity of (100) reflections with increasing of the impregnation Mo-content displaying in the small angle XRD-patterns, as well as the reduction of the pore volume and the surface area obtained from the nitrogen physisortion experiments revealed that MoO_3 particles were filled into the SBA-15 channels. The intensively reduction of reflection intensity of MoO_3 showed in the wide angle XRD patterns as well as SEM images confirm coincidently the formation of MoO_3 particles in nanoscale. A careful TEM analysis shows that the MoO_3 nanoparticles are

Type of Neighbor	Coordination number: N		Distance: R (Å)		R (Å) model	Debye - Waller factor: s^2(Å^2)	
	Mo/SBA-15 (B)	α-MoO_3	Mo/SBA-15 (B)	α-MoO_3	α-MoO_3 model	Mo/SBA-15 (B)	α-MoO_3 ± 0.0005
O1	2.8 ± 0.4	1	1.70 ± 0.001	1.66 ± 0.003	1.67	0.003 ± 0.0003	0.001
O2				1.72 ± 0.003	1.73		0.001
O3	1.1 ± 0.4	1	1.95 ± 0.002	1.94 ± 0.003	1.95	0.003 ± 0.0003	0.001
O4		2		2.24 ± 0.003	2.25		0.001
O5	0.6 ± 0.1	1	2.36 ± 0.010	2.32 ± 0.003	2.33	0.003 ± 0.0003	0.001
Si	0.2 ± 0.1		2.92 ± 0.020			0.003 ± 0.0003	
O6	2.0 ± 0.5	4	3.21 ± 0.003	3.40 ± 0.003	3.55	0.003 ± 0.0003	0.001
Mo1	2.0 ± 0.2	2	3.28 ± 0.002	3.43 ± 0.002	3.44	0.007 ± 0.0007	0.003
Mo2		2		3.68 ± 0.002	3.70		0.003
O7	1.0 ± 0.5	2	3.40 ± 0.003	3.60 ± 0.010	3.76	0.003 ± 0.0003	0.001
Mo3	0.6 ± 0.5	2	3.79 ± 0.002	3.95 ± 0.002	3.96	0.007 ± 0.0007	0.003
O8		2		3.83 ± 0.010	4.00		0.001
O9		2		3.90 ± 0.010	4.06		0.001
O10		2		3.93 ± 0.010	4.08		0.001
O11		2		3.94 ± 0.010	4.09		0.001
O12	1.2 ± 1	1	3.88 ± 0.01	4.00 ± 0.010	4.12	0.003 ± 0.0003	0.001

Table B.2: The results from the EXAFS analysis, Mo/SBA-15 (B) sample and α-MoO_3 reference, the values for α-MoO_3 are consistent with the ones reported in the references[107, 156, 157, 199]. The structure of ICSD 35076 is used as a model. (r factor of fit: Mo/SBA-15 (B): 0.003, α-MoO_3: 0.01)

.

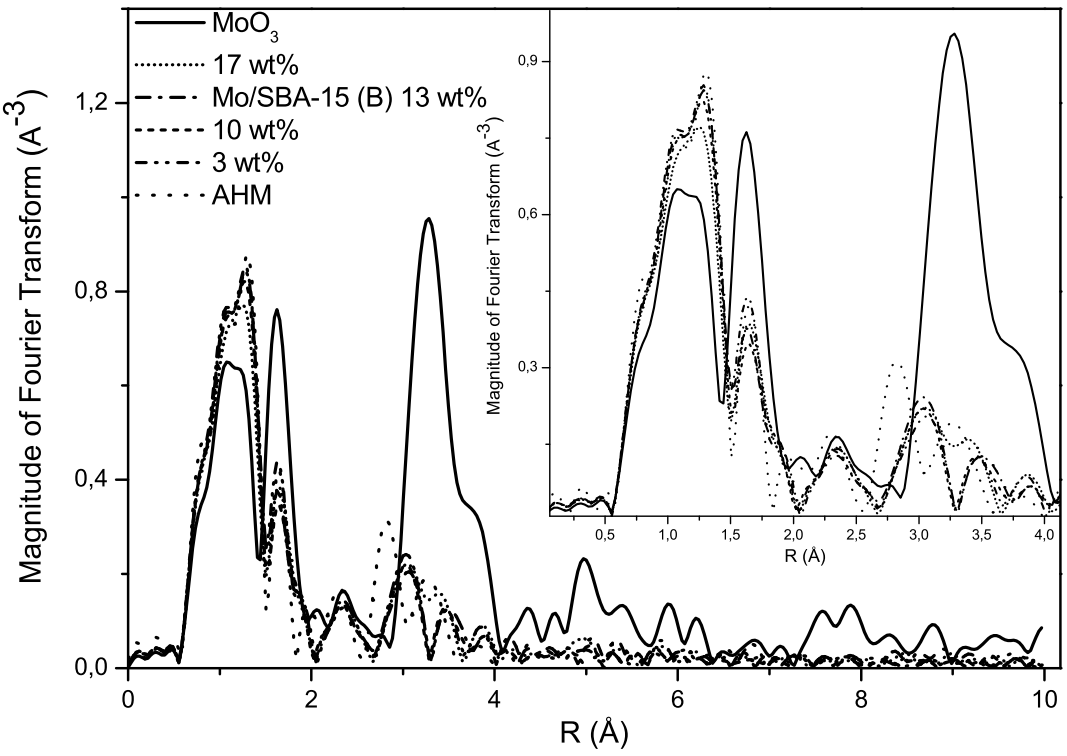

Figure B.14: FT EXAFS spectra.

limited by the ordered pore system and the nanoparticles tend to agglomerate to form wire-like structure along the mesoporous channels of SBA-15 silica. The wire-liked structure of MoO_3 supported on SBA-15 was also proved by the results of XAFS by applying a novel approach consisting of size and shape dependent calculations.

List of Figures

List of Tables

Bibliography

[1] http://ankaweb.fzk.de/.

[2] Camd web page: http://www.camd.lsu.edu/index.htm.

[3] http://hasylab.desy.de/facilities/.

[4] Iupac manual of symbols and terminology, appendix 2, part 1. *Pure Appl. Chem.*, (31):578, 1972.

[5] S. C. Abrahams and P. Marsh. *Acta Cryst. B*, 42:61, 1986.

[6] B. K. Agarwal. *X-Ray Spectroscopy: An Introduction.* Springer Series in Optical Sciences, Springer Verlag-Berlin, 1991.

[7] R. C. Alferness, R. V. Schmidt, and E. H. Turner. *Appl. Opt.*, 18:4012, 1979.

[8] J. J. Amodei and D. L. Staebler. *Appl. Phys. Lett.*, 18:540, 1971.

[9] K. Angermund, M. Bühl, U. Endruschat, F. T. Mauschick, R. Mörtel, R. Mynott, B. Tesche, N. Waldöfner, H. Bönnemann, G. Köhl, H. Modrow, J. Hormes, E. Dinjus, F. Gassner, H.-G. Haubold, T. Vad, and M. Kaupp. *J. Phys. Chem. B*, 107:7507, 2003.

[10] A. Ankudinov, B. Ravel, J. J. Rehr, and S. Conradson. *Phys. Rev. B*, 58:7665, 1998.

[11] R. M. Araujo, K. Lengyel, R. A. Jackson, L. Kovacs, and M. E. G. Valerio. *J. Phys.: Condens. Matter*, 19:046211, 2007.

[12] A. Ashkin, G. D. Boyd, J. M. Dziedzic, R. G. Smith, A. A. Ballman, J. J. Livinstein, and K. Nassau. *Appl. Phys. Lett.*, 9:72, 1966.

[13] ATOMS. The web page of atoms: http://cars9.uchicago.edu/ ravel/software/aboutatoms.html.

[14] AUTOBK. The web page of autobk: http://cars9.uchicago.edu/ newville/autobk/.

[15] S. Beauchemin, D. Hesterberg, and M. Beauchemin. *Soil Sci. Soc. Am. J.*, 66:83, 2002.

[16] M. Benfatto and S. Della Longa. *J. Synchr. Rad.*, 8:1087, 2001.

[17] U. Bergmann, C. R. Horne, T. J. Collins, J. M. Workman, and S. P. Cramer. *Chem. Phys. Lett.*, 302:119, 1999.

[18] U. Bergmann, P. Glatzel, J. H. Roblee, J. Messinger, C. Fernandez, R. Cinco, H. Visser, K. McFarlane, E. Bellacchio, S. Pizarro, K. Sauer, V. K. Yachandra, M. P. Klein, B. L. Cox, K. H. Nealson, and S. P. Cramer. *J. Synchrotron Rad.*, 8:199, 2001.

[19] D. P. Birnie. *Journal of Materials Science*, 28:302, 1993.

[20] H. Bönnemann and R.M. Richards. *European J. Inorg. Chem.*, 10:2455, 2001.

[21] S. Bocharov, Th. Kirchner, G. Dräger, O. Sipr, and A. Simunek. *Phys. Rev. B*, 63:045104, 2001.

[22] S. Braun, L. G. Appel, V. L. Camorim, and M. Schmal. *J. Phys. Chem. B*, 104:6584, 2000.

[23] B. Brendebach. *Röntgenabsorptionsspektroskopie an Phosphorsalzperlen: Bestimmung der geometrischen und elektronischen Struktur von metalloxid-dotierten Natriumphosphatgläsern.* Dissertation, Physikalisches Istitut, ISSN-0172-8741, 2004.

[24] B. Brendebach, F. Reinauer, N. Zotov, M. Funke, R. Glaum, J. Hormes, and H. Modrow. *Jour. of Non. Cryst. Sol.*, 351:1072, 2005.

[25] N. E. Brese and M. O'Keeffe. *Acta Cryst.*, B47:192, 1991.

[26] F. J. Brieler, M. Froeba, L. Chen, P. J. Klar, W. Heimbrodt, von H.-A. K. Nidda, T. Kurz, and A. Loidl. *Chem. Eur. J.*, 8:185, 2002.

[27] F. J. Brieler, P. Grundmann, M. Froeba, L. Chen, P. J. Klar, W. Heimbrodt, H.-A. K. von Nidda, T. Kurz, and A. Loidl. *J. Am. Chem. Soc.*, 126:797, 2004.

[28] I. D. Brown. *Acta Crystallogr., Sect. B: Struct. Sci.*, B41:254, 1985.

[29] I. D. Brown. *Acta Crystallogr., Sect. B: Struct. Sci.*, B48:553, 1992.

[30] S. Bucher. *Experimentelle Untersuchung der kantennahen Feinstruktur in den Röntgenabsorptionsspektren der 3d-Metalle und ihrer Oxide.* Staatsexamensarbeit, Physikalisches Institut der Universität Bonn, BONN-IB-98-16, 1998.

[31] K. Buse. *Appl. Phys. B: Lasers Opt.*, 64:391, 1997.

[32] K. Buse, S. Beer, K. Peithmann, S. Kapphan, M. Gao, and E. Krätzig. *Phys. Rev. B*, 56(3): 1225, 1996.

[33] K. Buse, A. Adibi, and D. Psaltis. *Nature*, 393:665, 1998.

[34] F. Caccavale, C. Sada, F. Segato, L. D. Bogomolova, N. A. Krasil'nikova, Yu. N. Korkishko, V. A. Fedorov, and T. V. Morozova. *J. Mater. Res.*, 15(5):1120, 2000.

[35] W. A. Caliebe, C.-C. Kao, and J. B. Hastings. *Phys. Rev. B*, 58(20):13452, 1998.

[36] P. J. Chandler and P. D. Townsend. *Nucl. Instrum. Methods Phys. Res. B*, 19/20:921, 1987.

[37] F. S. Chen, J. T. LaMacchia, and D. B. Fraser. *Appl. Phys. Lett*, 13:223, 1968.

[38] W. Y. Ching, Z.-Q. Gu, and Y.-N. Xu. *Phys. Rev. B*, 50:1992, 1994.

[39] G. Corradi, H. Söthe, J.-M. Spaeth, and K. Polgar. *J. Phys.: Condens. Matter*, 2:6603, 1990.

[40] F. M. F. de Groot. *Topics in Catal.*, 10:179, 2000.

[41] F. M. F. de Groot. American Institute of Physics, 2007.

[42] F. M. F. de Groot, P. Glatzel, U. Bergmann, P. A. van Aken, R. A. Barrea, S. Klemme, M. Ha1vecker, A. Knop-Gericke, W. M. Heijboer, and B. M. WeckhuysenĘ. *J. Phys. Chem. B*, 109:20751, 2005.

[43] Frank de Groot. *Chem. Rev.*, 101:1779, 2001.

[44] M. A. Denecke. *Coordination Chemistry Reviews*, 250:730, 2005.

[45] M. A. Denecke, J. Rothe, K. Dardenne, H. Blank, and J. Hormes. *Pysica Scr.*, T115:1001, 2005.

[46] A. N. Desikan, L. Huang, and S. T. Oyama. *J. Phys. Chem.*, 95:10050, 1991.

[47] G. L. Destefanis, P. D. Townsend, and J. P. Galliard. *Appl. Phys. Lett*, 32:293, 1978.

[48] G. M. Dhar, G. M. Kumaran, M. Kumar, K. S. Rawat, L. D. Sharma, B. D. Raju, and K. Rama Rao. *Catal. Today*, 99:309, 2005.

[49] R. Diamant, S. Huotari, K. Hämäläinen, R. Sharon, C.C. Kao, and M. Deutsch. *Rad. Phys. and Chem.*, 75:1434, 2006.

[50] H. Donnerberg, S. M. Tomlinson, C. R. A. Catlow, and O. F. Schirmer. *Phys. Rev. B*, 44 (10):4877, 1991.

[51] G. Döring, C. Sternemann, A. Kaprolat, A. Mattila, K. Hämäläinen, and W. Schülke. *Phys. Rev. B*, 70:085115, 2004.

[52] M. Falk and K. Buse. *Appl. Phys. B*, 81:853, 2005.

[53] M. Falk, J. Japs, T. Woike, and K. Buse. *Appl. Phys. B*, 87:119, 2007.

[54] F. Farges. *Phys. Rev. B*, 71:155109, 2005.

[55] FEFF. The web page of feff: http://leonardo.phys.washington.edu/feff/.

[56] FEFFIT. The web page of feffit: http://cars9.uchicago.edu/ newville/feffit/.

[57] I. A. Frenkel, W. Ch. Hills, and G. R. Nuzzo. *J. Phys. Chem B*, 105:51, 2001.

[58] M. Froeba, R. Koehn, and G. Bouffaud. *Chem. Mater.*, (11):2858, 1999.

[59] A. Fukuoka, H. Araki, Y. Sakamoto, N. Sugimoto, H. Tsukada, Y. Kumai, Y. Akimoto, and M. Ichikawa. *Nano Lett.*, 2:793, 2002.

[60] F. Gao, Q. Lu, X. Liu, Y. Yan, and D. Zhao. *Nanolett.*, 1:743, 2001.

[61] F. GelŠmukhanov and H. Ågren. *Phys. Rep. Rev. Sec. Phys. Lett.*, 312:91, 1999.

[62] N. Giordano, M. Meazzo, A. Castellan, J. C. Bart, and V. Ragaini. *J. Catal.*, 50:342, 1997.

[63] A. M. Glass, D. Von der Linde, and T. J. Negran. *Appl. Phys. Lett.*, 25:233, 1974.

[64] P. Glatzel and U. Bergmann. *Coord. Chem. Rev.*, 249:65, 2005.

[65] P. Glatzel, U. Bergmann, F. M. F. de Groot, and S. P. Cramer. *Phys. Rev. B*, 64:045109, 2001.

[66] P. Glatzel, L. Jacquamet, U. Bergmann, F. M. F. de Groot, and S. P. Cramer. *Inorg. Chem.*, 41:3121, 2002.

[67] P. Glatzel, U. Bergmann, F. M. F. de Groot, B. M. Weckhuysen, and S. P. Cramer. *Physica Scripta*, T115:1032, 2005.

[68] P. Glatzel, J. Yano, U. Bergmann, H. Visser, J. H. Robblee, W. Gu, F. M. F. de Groot, S. P. Cramer, and V. K. Yachandra. *J. of Phys. and Chem. of Solids*, 66:2163, 2005.

[69] E. Glavas, L. Zhang, P. J. Chandler, and P. D. Townsend. *Nucl. Instrum. Methods Phys. Res. B*, 32:45, 1988.

[70] Th. Gog, P. Schotters, J. Falta, G. Materlik, and M. Grodzicki. *Phys:Condens. Matter*, 7: 6971, 1995.

[71] M. Grush, G. Christou, K. Hämäläinen, and S. P. Cramer. *J. Am. Chem. Soc.*, 117:5895, 1995.

[72] L. Hafid and F. M. Michel-Calendini. *J. Phys. C:Solid State Phys.*, 19:2907, 1986.

[73] M. Hall. *Nature*, 422:556, 2003.

[74] Y.-J. Han and J. M. Kim G. D. Stucky. *Chem. Mater.*, 12:2068, 2000.

[75] U. Hartwig, K. Peithmann, B. Sturman, and K. Buse. *Applied Physics B*, 80:227, 2005.

[76] U. Hartwig, K. Peithmann, Th. Woike, and K. Buse. *J. Phys.: Condens. Matter*, 18:L447, 2006.

[77] H. Hayashi and Y. Udagawa. *Phys. Rev. B*, 66:033105, 2002.

[78] H. Hayashi, R. Takeda, Y. Udagawa, T. Nakamura, H. Miyagawa, H. Shoji, S. Nanao, and N. Kawamura. *Phys. Rev. B*, 68:045122, 2003.

[79] H. Hayashi, M. Kawata, R. Takeda, Y. Udagawa, Y. Watanabe, T. Takano, S. Nanao, and N. Kawamura. *J. of Elect. Spect. and Rel. Phen.*, 136:191, 2004.

[80] H. Hayashi, R. Takeda, M. Kawata, Y. Udagawa, N. Kawamura, Y. Watanabe, and S. Nanao. *Phys. Rev. B*, 70:155133, 2004.

[81] H. Hayashi, M. Kawata, R. Takeda, A. Sato, Y. Udagawa, N. Kawamura, and S. Nanao. *J. of Phys. and Chem. of Solids*, 66:2168, 2005.

[82] W. M. Heijboer, P. Glatzel, K. R. Sawant, R. F. Lobo, U. Bergmann, R. A. Barrea, D. C. Koningsberger, B. M. Weckhuysen, and F. M. F. de Groot. *J. Phys. Chem B*, 2004.

[83] K. Hermann, C. Daul L. G. M. Pettersson, M. E. Casida, A. Koester A. Goursot, A. St-Amant E. Proynov, and D. R. Salahub. The web page of stobe: http://w3.rz-berlin.mpg.de/ hermann/stobe/. 2006.

[84] N. Hilbrandt and M. Martin. *J. Phys. Chem. B*, 103:4797, 1999.

[85] H.-S. Hsueh, C.-T. Yang, J. I. Zink, and M. H. Huang. *J. Phys. Chem. B*, 109:4404, 2005.

[86] J. Hukriede, B. Gather, D. Kip, and E. Krätzig. *Phys. Status Solidi A*, 172:R3, 1999.

[87] ICSD. The web page of icsd: http://icsdweb.fiz-karlsruhe.de/.

[88] Y. Izumi and H. Nagamori. *Bull. Chem. Soc. Jpn.*, 73:1581, 2000.

[89] Y. Izumi, F. Kiyotaki, and Y. Seida. *J. Phys. Chem B*, 106:1518, 2002.

[90] Y. Izumi, F. Kiyotaki, N. Yagi, A.-M. Vlaicu, A. Nisawa, S. Fukushima, H. Yashitake, and Y. Iwasawa. *J. Phys. Chem B*, 109:14884, 2005.

[91] N. Kakuta, K. Tohji, and Y. Udagawa. *J. Phys. Chem.*, 92:2583, 1988.

[92] L. S. Kau, D. J. Spira-Solomon, J. E. Penner-Hahn, K. O. Hodgson, and E. I. Solomon. *J. Am. Chem. Soc.*, 109:6433, 1987.

[93] Shelly Kelly. Shelly kelly's web page: http://www.mesg.anl.gov/skelly.html.

[94] T.-J. Kühn, T. Vitova, S. Zinoveva, and J. Hormes. *Advances in Synchrotron Radiation*, Submitted manuscript, 2007.

[95] L. Kihlborg. *Ark Kemi.*, (21):357, 1963.

[96] Y. J. Kim, J. P. Hill, C. A. Burns, S. Wakimoto, R. J. Birgeneau, D. Casa, T. Gog, and C. T. Venkataraman. *Phys. Rev. Lett.*, 89(17):177003, 2002.

[97] D. Kip. *Appl. Phys. B*, 67:131, 1998.

[98] D. Kip, B. Gather, H. Bending, and E. Krätzig. *Phys. Status Solidi A*, 172:R3, 1999.

[99] I. V. Kityka, M. Makowska-Janusik, M. D. Fontana, M. Aillerie, and F. Abdi. *J. Appl. Phys.*, 90:5542, 2001.

[100] H. C. Külich. *Opt. Commun.*, 64:407, 1987.

[101] E. Kokanyan and E. Diguez. *J. Optoelectron. Adv. M.*, 2:205, 2000.

[102] Z. Ko'nya, V. F. Puntes, I. Kiricsi, J. Zhu, J. W. III Ager, M. K. Ko, H. Frei, P. Alivisatos, and G. A. Somorjai. *Chem. Mater.*, 15:1242, 2003.

[103] A. Kotani and S. Shin. *Rev. Mod. Phys.*, 203:73, 2001.

[104] S. Krinsky. *Fundamentals of Hard X-Ray Synchrotron Radiation Sources, in Third-Generation Hard X-ray Synchrotron Radiation Sources.* John Wiley and Sons, Inc., New York, 2002.

[105] E. Krätzig and R. Orlowski. *Ferroelectrics*, 27:241, 1980.

[106] H. Kurz, E. Krätzig, W. Keune, H. Engelmann, U. Gonser, B. Discher, and A. Raäber. *Appl. Phys.*, 12:355, 1977.

[107] A. Kuzmin and J. J. Purans. *Phys. Condens. Matter*, 12:1995, 2000.

[108] K. O. Kvashnina, S. M. Butorin, D. K. Shuh, J.-H. Guo, L. Werme, and J. Nordgren. *Phys. Rev. B*, 75:115107, 2007.

[109] C. Lastokie, K. E. Gubbins, and N. Quirke. *J. Phys. Chem.*, (97):4786, 1993.

[110] K.-B. Lee, S.-M. Lee, and J. Cheon. *Adv. Mater.*, 13:517, 2001.

[111] M. Lemonnier, O. Coller, C. Depautex, J. M. Esteva, and D. Raoux. *Nucl. Instr. Meth.*, 152: 109, 1978.

[112] L. Li, J.-L. Shi, L.-X. Zhang, L.-M. Xiong, and J.-N. Yan. *Adv. Mater.*, 16:1079, 2004.

[113] W. Li, G. D. Meitzner, R. W. Borry III, and E. Iglesia. *J. Catal.*, 191:373, 2000.

[114] H. Liu, J. Guo, Y. Yin, A. Augustsson, C. Dong, J. Nordgren, C. Chang, P. Alivisatos, G. Thornton, D. F. Ogletree, F. G. Requejo, F. de Groot, and M. Salmeron. *Nano Lett.*, 0 (0):A–D, 2007.

[115] T.-C. Liu, M. Forissier, G. Coudurier, and J. C. Vet'drine. *J. Chem. Soc. Faraday Trans. 1*, 85:1607, 1989.

[116] C. Louis, J. M. Tatibouet, and M. Che. *J. Catal.*, 109:354, 1988.

[117] Z. Luan, E. M. Maes, P. A. W. van der Heide, D. Zhao, R. S. Czernuszewicz, and L. Kevan. *Chem. Mater.*, 11:3680, 1999.

[118] F. W. Lytle, R. B. Greegor, and A. J. Panson. *Phys. Rev. B*, 37:1550, 1988.

[119] G. I. Malovichko and V. G. Grachev. *Sov. Phys. Solid State*, 27:1678, 1985.

[120] P. Marcus, A. V. Chadwick, and A. *J. Mater. Chem.*, 5(7):1043, 1995.

[121] G. Materlik and V. O. Kostroun. *Review of Scientific Instruments*, 51:86, 1980.

[122] K. Meerholz, B. L. Volodin, Sandalphon, Kippelen, and N. B. Peyghambarian. *Nature*, 371: 497, 1994.

[123] A. Meisel, G. Leonhardt, and R. Szargan. *In X-Ray Spectra and Chemical Binding*, volume 37. Springer-Verlag: Berlin, 1989.

[124] G. Mestl, T. K. K. Srinivasan, and H. Knoezinger. *Langmuir*, 11:3795, 1995.

[125] F. Micheron and G. Bismuth. *Appl. Phys. Lett.*, 20:79, 1972.

[126] H. Modrow, S. Bucher, J. J. Rehr, and A. L. Ankudinov. *Phys. Rev. B*, 67:035123, 2003.

[127] H. Modrow, M. O. Rahman, R. Richerd, J. Hormes, and H. Bönnemann. *J. Phys. Chem.*, 107:12221, 2003.

[128] C. Monesi, C. Meneghini, F. Bardelli, M. Benfatto, S. Mobilio, U. Anju, and D. D. Sarma. *Nucl. Instr. and Meth. B*, 246:158, 2006.

[129] R. Murugan and H. Chang. *J. Chem. Soc. dalton Trans.*, page 3125, 2001.

[130] I. Nee, K. Buse, F. Havermeyer, R. A. Rupp, M. Fally, and R. P. May. *Phys. Rev. B*, 60: R9896, 1999.

[131] I. Nee, M. Müller, K. Buse, and E. Krätzig. *J. Appl. Phys.*, 88:4282, 2000.

[132] Y. Nisikawa, M. Usuda, J. Igarashi, H. Shoh, and T. Iwazumi. *J. of the Phys. Soc. Jap.*, 73 (4):970, 2004.

[133] M. Newville Fundamentals of XAFS. 2004.

[134] Kh. Olimov, M. Falk, K. Buse, Th. Woike, J. Hormes, and H. Modrow. *J. Phys. Cond. Mat.*, 8:5131, 2006.

[135] T. Ono, M. Anpo, and Y. Kubokawa. *J. Phys. Chem.*, 90:4780, 1986.

[136] A. Pantelouris, H. Modrow, M. Pantelouris, J. Hormes, and D. Reinen. *Chemical Physics*, 300:13, 2004.

[137] M. Pape, H.-J. Reyher, and O. F. Schirmer. *J. Phys.: Condens. Matter*, 17:6835, 2005.

[138] L. G. Parratt. *Rev. of Mod. Phys.*, 31:616, 1959.

[139] K. Peithmann, A. Wiebrock, and K. Buse. *Appl. Phys. B: Lasers Opt.*, 68:777, 1999.

[140] K. Peithmann, J. Hukriede, K. Buse, and E. Krätzig. *Phys. Rev. B*, 61:4615, 2000.

[141] K. Peithmann, K. Buse, and E. Krätzig. *Appl. Phys. B*, 74:549, 2002.

[142] K. Peithmann, M.-R. Zamani-Meymian, M. Haaks, K. Maier, B. Andreas, and I. Breunig. *Opt. Soc. Am. B*, 23(10):2107, 2006.

[143] K. Peithmann, M.-R. Zamani-Meymian, M. Haaks, K. Maier, B. Andreas, K. Buse, and H. Modrow. *Appl. Phys. B*, 82:419, 2006.

[144] G. Peng, F. M. F. deGroot, K. Hämäläinen, J. A. Moore, X. Wang, M. M. Grush, J. B. Hastings, D. P. Siddons, W. H. Armstrong, O. C. Mullins, and S. P. Cramer. *J. Am. Chem. Soc.*, 116:2914, 1994.

[145] G. D. Pirngruber, J.-D. Grunwaldt, J. A. van Bokhoven, A. Kalytta, A. Reller, O. V. Safonova, and P. Glatzel. *J. Phys. Chem. B Lett.*, 110:18104, 2006.

[146] G. D. Pirngruber, J.-D. Grunwaldt, J. A. van Bokhoven, A. Kalytta, A. Reller, O. V. Safonova, and P. Glatzel. *Catal. Today*, 2006.

[147] S. A. Pizarro, P. Glatzel, H. Visser, J. H. Robblee, G. Christou, U. Bergmann, and V. K. Yachandra. *Phys. Chem. Chem. Phys.*, 6:4864, 2004.

[148] Y. Pushkar, J. Yano, P. Glatzel, J. Messinger, A. Lewis, K. Sauer, U. Bergmann, and V. Yachandra. *J. of Biol. Chem.*, 282(10):7198, 2007.

[149] M. A. Py and K. A. Maschke. *Physica B*, (105):376, 1981.

[150] B. Ravel. *Journal of Alloys and Compounds*, 401:118, 2005.

[151] B. Ravel and M. Newville. *J. Synchrotron Rad.*, 12:537, 2005.

[152] B. Ravel, Y-I. Kim, P. M. Woodward, and C. M. Fang. *Phys. Rev. B*, 73:184121, 2006.

[153] J. J. Rehr and R. C. Albers. *Rev. of Mod. Physics*, 73(3):621, 2000.

[154] J. J. Rehr, J. Mustre de Leon, S. I. Zabinsky, and R. C. Alberts. *J. Amer. Chem. Soc.*, 113: 5135, 1991.

[155] A. Reich, M. Panthöfer, H. Modrow, U. Wedig, and M. Jansen. *JACS*, 126:14428, 2004.

[156] T. Ressler, J. Wienold, R. E. Jentoft, and T. Neisius. *Phys. Rev. B*, 210:67, 2002.

[157] T. Ressler, J. Wienold, R. E. Jentoft, and F. Girgsdies. *Eur. J. Inorg. Chem.*, page 301, 2003.

[158] D. G. Rexford and Y. M. Kim. *J. Chem. Phys.*, 57:3094, 1972.

[159] J. Rothe, J. Hormes, H. Bönnemann, W. Brijoux, and K. Siepen. *JACS*, 120:6019, 1998.

[160] J. P. Rueff, A. Shukla, A. Kaprolat, M. Kirsh, M. Lorenzen, F. Sette, and R. Verbeni. *Phys. Rev. B*, 63:132409, 2001.

[161] A. Sampieri, S. Pronier, J. Blanchard, M. Breysse, S. Brunet, K. Fajerwerg, C. Louis, and G. Pérot. *Catal. Today*, 107-108:537, 2005.

[162] D. E. Sayers, E. A. Stern, and F. W. Lytle. *Phys. Rev. Lett.*, 27:1204, 1971.

[163] O. F. Schirmer, O. Thiemann, and M. Wöhlecke. *J. Phys. Chem. Solids*, 52:185, 1991.

[164] R. V. Schmidt and I. P. Kaminow. *Appl. Phys. Lett.*, 25:458, 1974.

[165] T. K. Sham, R. A. Gordon, and S. M. Heald. *Phys. Rev. B*, 72:035113, 2005.

[166] R. D. Shannon and C. T. Prewitt. *Acta. Cryst.*, B25:925, 1969.

[167] K. Shimizu, H. Maeshima, H. Yoshida, A. Satsuma, and T. Hattori. *Phys. Chem. Chem. Phys.*, 3:862, 2001.

[168] V. A. Shuvaeva, K. Yanagi, K. Yagi, K. Sakaue, and H. Terauchi. *J. Synchrotron Rad.*, 6: 367, 1999.

[169] R. Sommerfeldt, R. S. Rupp, H. Vormann, and E. Krätzig. *Phys. Status Solidi A*, 99:K15, 1987.

[170] R. Sommerfeldt, L. Holtmann, E. Krätzig, and B.C. Grabmaier. *Phys. Status Soliddi A*, 89: 106, 1988.

[171] SPEC. The web page of spec: http://www.certif.com/.

[172] SPRKKR. The web page of sprkkr: http://olymp.cup.uni-muenchen.de/ak/ebert/sprkkr/.

[173] S. R. Stampfl, Y. Chen, J. A. Dumesic, C. Niu, and Jr. C. G. Hill. *J. Catal.*, 105:445, 1987.

[174] E. A. Stern. *Phys. Rev. B*, 10:3027, 1974.

[175] E. A. Stern. *Theory of EXAFS. X-Ray Absorption: Principles, Applications, Techniques of EXAFS, SEXAFS and XANES.* Wiley; New York; ISBN 0-471-87547-3, 1988.

[176] E. A. Stern and S. M. Heald. *Basic Principles and Applications of EXAFS in Handbook of Synchrotron Radiation.* New York, North-Holland, 1983.

[177] E. A. Stern and K. Kim. *Phys. Rev. B*, 23:3781, 1981.

[178] E. A. Stern, W. T. Elam, B. A. Bunker, and K. Lu. *Nuc. Inst. Meth.*, 195:345, 1982.

[179] H. Söthe and J-M Spaeth. *J. Phys.: Condens. Matter*, 4:9901, 1992.

[180] J. Stöhr. *NEXAFS Spectroscopy*. Springer Series in Surface Sciences, Vol. 25, Springer Verlag, Berlin, ISBN 3-540-54422-4, 1992.

[181] V. Stojanoff, K. Hämäläinen, D. P. Siddons, J. B. Hastings, L. E. Berman, S. Cramer, and G. Smith. *Rev. Sci. Instrum.*, 63:1125, 1992.

[182] Uwe Bergmann's talk given in 2004 in Upton NY. The talk is located at: www.bnl.gov/nsls2/oldworkshops/nsls-ii/presentations/bergmannixs.pdf.

[183] B. K. Teo. *EXAFS: Basic Principles and Data Analysis*. Inorganic Chemistry Concepts, Vol. 9, Springer Verlag,Berlin„ 1986, 1986.

[184] O. Thiemann and O. F. Schirmer. *Proc. SPIE*, 1018:18, 1988.

[185] Y. Udagawa, H. Hayashi, K. Tohji, and T. Mizushima. *J. Phys. Soc. Jap.*, 63(5):1713, 1994.

[186] P. van Heerden. *J. Appl. Optics*, 2:387, 1963.

[187] G. Vanko and F. M. F. de Groot. *Phys. Rev. B*, 75:177101, 2007.

[188] G. Vanko, T. Neisius, G. Molnar, F. Renz, S. Kaprati, A. Shukla, and F. M. F. de Groot. *J. Phys. Chem. B*, 110:11647, 2006.

[189] G. Vanko, J.-P. Rueff, A. Mattila, Z. Nemeth, and A. Shukla. *Phys. Rev. B*, 73:024424, 2006.

[190] T. Vitova, S. Zinoveva, and J. Hormes. *HASYLAB User Reports*, 2006.

[191] T. Vitova, J. Hormes, K. Peithmann, and Th. Woike. *Phys. Rev. B*, 77:144103, 2008.

[192] D. von der Linde, A. M. Glass, and K. F. Rodgers. *Appl. Phys. Lett.*, 25:155, 1974.

[193] L. Vradman, M. V. Landau, M. Herkowitz, V. Ezersky, M. Talianker, S. Nikitenko, Y. Koltypin, and A. Gedanken. *Stud. Surf. Sci. Catal.*, 146:721, 2003.

[194] D. Wang, W. L. Zhou, B. F. McCaughy, J. E. Hampsey, X. Ji, Y.-B. Jiang, H. Xu, J. Tang, R. H. Schmehl, C. O'Connor, C. J. Brinker, and Y. Lu. *Adv. Mater.*, 15:130, 2003.

[195] R. S. Weis and T. K. Gaylord. *Appl. Phys. A*, 37:191, 1985.

[196] E. Welter, P. Machek, G. Dräger, U. Brüggmann, and M. Fröba. *J. Synchrotron Rad.*, 12: 448, 2005.

[197] C. Wende, Kh. Olimov, H. Modrow, F. E. Wagner, and H. Langbein. *Mat. Res. Bull.*, 41: 1530, 2006.

[198] M. Wöhlecke, G. Corradi, and K. Betzler. *Appl. Phys. B*, 63:323, 1996.

[199] J. Wienold, R. E. Jentoft, and T. Ressler. *Eur. J. Inorg. Chem.*, page 1058, 2003.

[200] M. Wilke, F. Farges, P.-E. Petit, G. E. Brown JR., and F. Martin. *American Mineralogist*, 86:714, 2001.

[201] J. Wong, F. W. Lytle, R. P. Messmer, and D. H. Maylotte. *Phys. Rev. B*, 30:5596, 1984.

[202] W. Xu, Y. Liao, and D. L. Akins. *J. Phys. Chem. B*, 106:11127, 2002.

[203] D. Xue and X. He. *Phys. Rev. B*, 73:064113, 2006.

[204] W. Yan, B. Chen, S. M. Mahurin, E. W. Hagaman, S. Dai, and S. H. Overbury. *J. Phys. Chem. B*, 108:2793, 2004.

[205] C.-M. Yang, P.-H. Liu, Y.-F. Ho, C.-Y. Chiu, and K.-J. Chao. *Chem. Mater.*, 15:275, 2003.

[206] C.-T. Yang and M. H. Huang. *J.Phys. Chem. B*, 109:17842, 2005.

[207] Y. Yang, I. Nee, K. Buse, and D. Psaltis. *Appl. Phys. Lett.*, 78:4076, 2001.

[208] Y. Yang, D. Psaltis, M. Luennemann, D. Berben, U. Hartwig, and K. Buse. *J. Opt. Soc. Am. B*, 20(7):1491, 2003.

[209] J. Yano, Y. Pushkar, P. Glatzel, A. Lewis, K. Sauer, J. Messinger, and U. Bergmann V. Yachandra. *J. Am. Chem. Soc.*, 127:14974, 2005.

[210] I. Yuranov, L. Kiwi-Minsker, P. Buffat, and A. Renken. *Chem. Mater.*, 16:760, 2004.

[211] S. I. Zabinsky, J. J. Rehr, and A. Ankudinov. *Phys. Rev. B*, 52:2995, 1994.

[212] C. Zaldo, F. Agullo-Lopez, J. Garcie, A. Marcelli, and S. Mobilio. *Solid State Commun.*, 71: 243, 1989.

[213] M. R. Zamani-Meymian, K. Peithmann, K. Maier, and H. Schmid. *J. Phys. C: Solid State Physics*, submitted, 2007.

[214] K. Zhang, E. A. Stern, J. J. Rehr, and F. Ellis. *Phys. Rev. B*, 44(5):2030, 1991.

[215] L. Zhang, P. J. Chandler, and P. D. Townsend. *Nucl. Instrum. Methods Phys. Res. B*, 59/60: 1147, 1991.

[216] D. Zhao, J. Feng, Q. Huo, N. Melosh, G. H. Fredrickson, B. F. Chmelka, and G.D. Stucky. *Science*, 279:548, 1998.

[217] D. Zhao, Q. Huo, J. Feng, B. F. Chmelka, and G. D. J. Stucky. *J. Am. Chem. Soc.*, 120:6024, 1998.

[218] M. G. Zhao and M. Chiu. *Phys. Rev. B*, 49:12556, 1994.

[219] J. F. Ziegler, J. P. Biersack, and U. Littmark. *The Stopping and Range of Ions in Solids*. Pergamon, 1985.

Publications

[1] T.Vitova, M. - R. Zamani - Meymian, K. Maier, K. Peithmann, J. Hormes, "X-ray Absorption Spectroscopy Investigation of Lithium Niobate Irradiated with helium Ions. (3He:LiNbO3)", Proceedings of the 4th Workshop on Speciation, Techniques and Facilities for Radioactive Materials at Synchrotron Light Source, special issue of the "Nuclear Energy Agency (OECD-NEA) News".

[2] B. Brendebach, K. Dardenne, M. A. Denecke, J. Rothe, T. Vitova, "New developments at the INE-Beamline for actinide research at ANKA", Nucl. Instr. and Method. in Phys. Res. A, 582:80, 2007.

[3] T. Vitova, K. Peithmann, T. Woike, J. Hormes, "X-ray Absorption Spectroscopy study of valency and site occupation of copper in Cu-doped lithium niobate crystals", Phys. Rev. B, 77:144103, 2008.

[4] T. Vitova, M. Falk, K. Buse, J. Hormes, "Site-selective investigation of site symmetry and site occupation of iron in Fe-doped lithium niobate crystals", Journal of Applied Physics (accepted).

[5] T. Vitova, M. Falk, T. Woike, K. Buse, J. Hormes "Valency and site occupation of manganese in Mn-doped lithium niobate crystals: a combined X-ray and visible-light absorption and high-resolution X-ray emission study", Phys. Rev. B (submitted).

[6] T. Vitova, M.-R. Zamani - Meymian, K. Peithmann, K. Maier, J. Hormes, "X-ray Absorption Spectroscopy investigation of a single lithium niobate crystal irradiated with high-energy particles", J. Phys. C: Solid State Phys. (submitted).

[7] T.-J. Kühn, T. Vitova, S. Zinoveva, J. Hormes, "Characterizing metallic nanoparticles by X-ray Absorption Spectroscopy: two new approaches", Advances in Synchrotron Radiation (submitted).

Acknowledgment

I would like to thank:

Prof. Dr. J. Hormes for giving me the opportunity to work in the Synchrotron Radiation Group, for the freedom and reliance during my research activities and for the intensive discussions during the last year.

Prof. Dr. K. Maier for agreeing to be my Korreferent.

Priv.-Doz. Dr. H. Modrow for supervising my work during my first two years in Syli group and for inspiring me for a "different" way of thinking.

Dr. Peithmann for preparing the copper-doped LN crystals, for discussing many times, many topics with me and for answering my many questions. It was just great to work with you!

Dr. Reza Zamani for the good collaboration and the readiness to irradiate as many crystals as he was asked to.

Dr. Falk for agreeing to bring his experiment to Karlsruhe, for answering my questions, for the very helpful discussions and the fruitful collaboration.

Prof. Dr. K. Buse for the very useful discussions and the fast reactions on any issue.

Priv.-Doz. Dr. T. Woike for the fruitful collaboration and discussions.

Hubert Blank for the technical support and for speaking German with me.

Dr. Natalie Palina for showing me how to prepare samples and for supporting me in good and bad moments.

Dr. Zinoveva for the many nice lunches and conversations, and for the great time spent together in Baton Rouge.

All former and present Syli members for the friendly atmosphere.

Dr. Boris Brendebach for helping me at the INE bemline, reading and correcting my thesis and listening with understanding to all my problems during these four years.

Dr. Melissa Denecke, Dr. Jörg Rothe and Dr. Kathy Dardenne for the help at the INE beamline and for making me feel like at home during all my stays at ANKA, as well as for reading my manuscripts and giving valuable suggestions.

Dr. Melissa Denecke for the many nice Pizza, for the care about me and for reading and correcting my manuscripts and this thesis.

Dr. Jörg Göttlicher and Dr. Stefan Mangold for the friendliness and the nice time spent at ANKA discussing various topics.

My dear Rupal and Martin for being my German family, supporting me in sorrow and happiness.

Nata, Svetka and Tomka for all nice, funny moments in our apartment in S.A.

Irina Lilyanova for correcting my English in the thesis.

My dear Nely, Ira and Any for the friendship, no matter how many kilometers divide us.

My family for the love and constant support.

My mother for being my best friend and my best critic.

And a very special Thank you to my dear Vlady! This would not be possible, without your patience and love.